

Self-Assembly Techniques for Massively Parallel  
Packaging of MEMS Devices

Jiandong Fang

A dissertation  
submitted in partial fulfillment of the  
requirements for the degree of

Doctor of Philosophy

University of Washington

2006

Program Authorized to Offer Degree:  
Electrical Engineering



University of Washington  
Graduate School

This is to certify that I have examined this copy of a doctoral dissertation by

Jiandong Fang

and have found that it is complete and satisfactory in all respects,  
and that any and all revisions required by the final  
examining committee have been made.

Chair of Supervisory Committee:

  
\_\_\_\_\_

Karl F. Böhringer


Reading Committee:

  
\_\_\_\_\_

Karl F. Böhringer

  
\_\_\_\_\_

Alexander Mamishev

  
\_\_\_\_\_

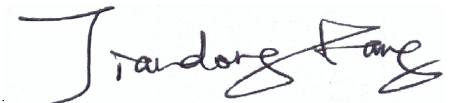
Steve Shen

Date:

July 31, 2006



In presenting this dissertation in partial fulfillment of the requirements for the doctoral degree at the University of Washington, I agree that the Library shall make its copies freely available for inspection. I further agree that extensive copying of this dissertation is allowable only for scholarly purposes, consistent with "fair use" as prescribed in the U.S. Copyright Law. Requests for copying or reproduction of this dissertation may be referred to Proquest Information and Learning, 300 North Zeeb Road, Ann Arbor, MI 48106-1346, or to the author.

Signature  \_\_\_\_\_

Date \_\_\_\_\_



University of Washington

Abstract

Self-Assembly Techniques for Massively Parallel  
Packaging of MEMS Devices

Jiandong Fang

Chair of Supervisory Committee:  
Professor Karl F. Böhringer  
Electrical Engineering

This dissertation investigates applications of self-assembly for massively parallel packaging of flat micro-components, the most common appearance of microelectromechanical systems (MEMS) or CMOS chips. Self-assembly assembles micro-components in parallel without any serial, one-by-one manipulation of components. To satisfy various packaging requirements, we have developed and demonstrated four different self-assembly processes: capillary-driven self-organizing parallel assembly (C-SPASS), semi dry uniquely orienting self-organizing parallel assembly (semi DUO-SPASS), DUO-SPASS and vertical/horizontal self-organizing parallel assembly (VH-SPASS).

The C-SPASS process assembles micro-components onto liquid covered receptor sites by minimizing interfacial energies until components align with receptor sites. We have demonstrated this assembly process by bonding PZT actuators for micro fluidic pumps (liquid adhesive polymerized for permanent bonding), and these pumps showed high performance uniformity: a low deviation  $\sim 1.5\%$  for pumping rates at resonant frequencies.

The semi DUO-SPASS process is based on single-stage shape recognition between a part's peg and a receptor site's hole. Orbital shaking moves parts to be trapped.





Unique in-plane alignment is achieved by minimizing potential energy based on pendulum's principle (the peg is located offset from the center of mass of the component). Our demonstrated experiments resulted in  $\sim 99\%$  yields after 3 minutes' agitation for 2mm square parts.

The DUO-SPASS process relies on two-stage shape recognition between two pegs on a part and two recessed features in a receptor site. The 1<sup>st</sup> recognition by a tall circular peg anchors the part, and the 2<sup>nd</sup> recognition by a shallow cross peg fixes the part to a specific in-plane orientation. Our demonstrated experiments resulted in  $\sim 98\%$  yields for 1mm square parts.

The VH-SPASS process relies on single-stage shape matching and capillary forces. Driven by vibration, parts are trapped to apertures with an opening only for a vertically standing part. Horizontal and vertical assemblies are respectively achieved with and without additional capillary torques introduced by steam condensate. Assembly results showed  $\sim 1\%$  defect rates for 1000 receptor sites on a 4" substrate.



# TABLE OF CONTENTS

<b>List of Figures</b>	<b>iv</b>
<b>List of Tables</b>	<b>vii</b>
<b>Glossary</b>	<b>viii</b>
<b>Chapter 1: Introduction</b>	<b>1</b>
1.1 Introduction and Motivation of Micro-Assembly . . . . .	1
1.2 State of the Art in Micro-Assembly . . . . .	3
1.3 Self-Assembly Techniques . . . . .	4
<b>Chapter 2: Concepts and Materials</b>	<b>17</b>
2.1 MEMS Packaging . . . . .	17
2.2 Self-Assembly Processes . . . . .	18
2.3 Self-Assembled Monolayers . . . . .	20
2.4 Hydrophobic and Hydrophilic Surfaces . . . . .	21
2.5 Bonding Methods . . . . .	22
<b>Chapter 3: Capillary-Driven Self-Assembly</b>	<b>26</b>
3.1 Introduction . . . . .	26
3.2 Capillary-Driven Self-Assembly Mechanism . . . . .	27
3.3 Diffuser Valve Micro Pumps . . . . .	30
3.4 PZT Self-Assembly . . . . .	35
3.5 Pumping Tests . . . . .	42

3.6	Conclusions and Discussions . . . . .	44
<b>Chapter 4:</b>	<b>Uniquely Orienting Self-Assembly (DUO-SPASS Processes)</b>	<b>47</b>
4.1	Introduction . . . . .	47
4.2	Wafer Level Packaging Strategy . . . . .	48
4.3	The Semi Dry Assembly Process (SEMI-DUO-SPASS) . . . . .	50
4.4	The Dry Assembly Process (DUO-SPASS) . . . . .	61
4.5	Wafer-Level Flip-chip Bonding . . . . .	71
4.6	Application to Non-silicon Parts . . . . .	71
4.7	Conclusions and Discussions . . . . .	72
<b>Chapter 5:</b>	<b>Vertical and Horizontal Parallel Assembly</b>	<b>76</b>
5.1	Introduction . . . . .	76
5.2	Parallel Assembly Strategy . . . . .	77
5.3	Fabrication and Surface Treatment . . . . .	79
5.4	Physical Modeling . . . . .	81
5.5	Experimental Implementation . . . . .	89
5.6	Discussions . . . . .	99
5.7	Conclusions . . . . .	101
<b>Chapter 6:</b>	<b>Conclusion</b>	<b>103</b>
6.1	Results Summary . . . . .	103
6.2	Research Outlook . . . . .	106
<b>Bibliography</b>		<b>108</b>
<b>Appendix A:</b>	<b>Photolithography Recipes</b>	<b>122</b>
A.1	Positive Photoresist: AZ1512 . . . . .	122
A.2	Positive Photoresist: AZ4620 . . . . .	123

A.3 Negative Photoresist: single layer SU8-2025 . . . . .	124
A.4 Negative Photoresist: double layer SU8-2025 . . . . .	125
<b>Appendix B: Deep Reactive Ion Etching</b>	<b>127</b>

## LIST OF FIGURES

Figure Number	Page
1.1 Schematic diagrams showing a typical self-assembly process . . . . .	5
1.2 Schematic overviews of capillary-driven self-assembly processes . . . . .	13
2.1 Schematic overviews of typical MEMS packaging processes . . . . .	19
2.2 Schematic side view of a liquid droplet sitting on a solid surface . . . . .	22
2.3 Schematic view of a typical anodic bonding setup. . . . .	24
3.1 A schematic top view of a part on a binding site . . . . .	28
3.2 Visualization of overlap area between a moving part and a binding site . . . . .	31
3.3 Schematic views of a diffuser valve micro pump . . . . .	32
3.4 Microscope images of DRIEed silicon substrate and the diffuser valve layout. . . . .	33
3.5 Optical images of the bonded stack and Au patterns on pyrex . . . . .	34
3.6 Wetting property of PZT parts and the pump substrate . . . . .	36
3.7 Schematic diagrams for orbital shaking assisted self-assembly . . . . .	38
3.8 Schematic overview of a pressing plate method . . . . .	40
3.9 An optical image of assembled micro pumps . . . . .	40
3.10 Optical images showing the electrical connections to a PZT actuator . . . . .	40
3.11 Schematic experimental setup for de-bonding tests . . . . .	41
3.12 Distribution of resonant frequencies for all the 28 pumps on a 4" substrate. . . . .	43
3.13 A reusable testing stage . . . . .	45

4.1	Wafer level packaging strategy . . . . .	49
4.2	One-to-one registration design rule . . . . .	51
4.3	Microscope images of parts and receptor sites for a semi DUO-SPASS process . . . . .	52
4.4	Schematic view of orbitally shaken water surface . . . . .	54
4.5	Water surface bending near carrier wafer surfaces . . . . .	56
4.6	The palletizing process for a semi DUO-SPASS process . . . . .	57
4.7	Mechanism of parts adhering to a hydrophobic surface . . . . .	58
4.8	Trapping results of a semi DUO-SPASS process . . . . .	59
4.9	Unique aligning of parts by potential energy minimization . . . . .	60
4.10	The assembly result of a semi DUO-SPASS process . . . . .	61
4.11	Schematic overview of a DUO-SPASS process . . . . .	64
4.12	A schematic top view of the exact alignment between a part and a receptor site . . . . .	65
4.13	Fabrication steps for aligning features on silicon parts by DRIE . . . . .	66
4.14	Optical photographs of templates and assembly results . . . . .	69
4.15	Fabrication steps of double-layer SU8 aligning features on parts . . . . .	72
4.16	An optical microscope image of an array of SU8 pegs . . . . .	73
5.1	Schematic overview of the assembly process with controlled poses and high surface coverage . . . . .	78
5.2	Optical images of flat-edge and step-edge parts . . . . .	80
5.3	Microscope images of water droplets on different surfaces: . . . . .	80
5.4	Microscopic side views of parts attached to receptor sites . . . . .	82
5.5	Schematic views of a vertically standing square part on a receptor site . . . . .	83
5.6	Schematic views of mounting of a step-edge part . . . . .	86

5.7	A schematic graph for a pressing plate to lay down a tilted step-edge part . . . . .	89
5.8	Experimental setup for parts falling into apertures . . . . .	90
5.9	Schematic design rule for parts, apertures and receptor sites . . . . .	91
5.10	Optical images of $790\mu\text{m}$ square parts falling into apertures vertically	92
5.11	Optical images of $790\mu\text{m}$ square parts transferred to a palletizing pyrex plate via water droplets . . . . .	93
5.12	Optical images of vertically mounted $790\mu\text{m}$ square parts . . . . .	94
5.13	Permanent bonding of $790\mu\text{m}$ square parts . . . . .	96
5.14	Optical images of parts bonded with melting solder . . . . .	97
5.15	Optical images of horizontal mounting of $790\mu\text{m}$ square step-edge parts	98
5.16	Fine alignment for vertically standing parts by gravity . . . . .	100



## LIST OF TABLES

Table Number	Page
3.1 Contact angles of water and the adhesive liquid on different surfaces .	37
3.2 Ethanol pumping results of the eight pumps . . . . .	42

## GLOSSARY

ACF: Anisotropic conducting film.

ANODIC BONDING: A typical process to bond pyrex and silicon using high electric fields.

AT: Alignment template.

BOE: Buffered oxide etchant.

CCT: Chip carrier template.

CP: Circular peg.

CT: Circular trench.

CW: Carrier wafer.

CVD: Chemical vapor deposition.

DI WATER: De-ionized water.

DRIE: Deep reactive ion etching.

DSP: Double side polished.

DUO: Dry uniquely orienting.

LED: Light emitting diode.

LIGA: A lithography method to fabricate 3d microstructures.

LPCVD: Low pressure chemical vapor deposition.

LTO: Low temperature oxide, i.e., oxide thin film deposited by chemical vapor deposition, a typical process temperature is 350°C.

MEMS: Microelectromechanical systems.

MUMPS: Multiple user MEMS processes.

PHOTOLITHOGRAPHY: A process to transfer patterns using short wavelength light such as UV light and X-ray.

ORBITAL SHAKER: An agitating apparatus with a platform supported by three identical rotating arms (synchronized rotation).

PZT: A type of piezoelectric material.

RECEPTOR SITE: A site to anchor or bond a micro-component.

RFID: Radio frequency identification.

RIE: Reactive ion etching.

SAM: Self-assembled monolayer.

SPASS: Self-organizing parallel assembly.

SSP: Single side polished.

THIOLATED: soaked in an alkenthiol solution and then coated with a self-assembled monolayer.

XP: Cross peg.

XT: Cross trench.

## ACKNOWLEDGMENTS

During the several years of my doctoral research, I was very lucky to get to know many knowledgeable people, and I was deeply impressed about their generosity to share their knowledge and experiences with me and provide me help with research and experiments.

First of all, I like to thank my academic advisor Karl Böhringer. He initiated my inspiration in this doctoral research with his wide-range knowledge about MEMS and helpful guidance. He always gave me encouragements to do experiments and test new ideas. He was very patient to discuss every detail of the research with me and supply me with many instructive suggestions.

My colleagues in the MEMS research group of the University of Washington encouraged and helped me a lot in both research and everyday life. Especially, I like to thank Xiaorong Xiong, Kerwing Wang, Yanbing Wang, Sheng-Hsiung Liang, Ashutosh Shastry, Sangjun Park, Anupama Govindarajan and Neil A. Bernotski for their long time support.

I also like to thank Tai-Chang Chen, Greg Golden and Eric Miller for their kind sharing of micro-fabrication experiences with me. Their hands-on experiences prevented me from wasting much time in the new processes and benefited my new designs of experiments a lot.

During the summer of 2003, I was lucky to work on a very interesting intern project at Microsoft Research. There my mentor Mike Sinclair shared with me a lot of interesting ideas and encouraged me a lot on the projects. I also like to thank Rajashree Baskaran from Intel for very helpful discussions about self-assembly research

goals.

During my initial doctoral research project about micro fluidic pumps, I gained much knowledge about pump design and testing from Yael Hanein, Fred Forster, Brian Williams and Chris Morris. I really appreciate their kind help.

## DEDICATION

My wife Yan and my family.





## Chapter 1

# INTRODUCTION

### ***1.1 Introduction and Motivation of Micro-Assembly***

#### *1.1.1 The Growing Need for Assembly*

Micro-assembly is a technique to create complex microstructures and systems by integrating micro-components made in separate manufacturing processes. Two-dimensional micro-assembly mounts components on a flat substrate, and three-dimensional micro-assembly produces structures with more intricate spatial geometry.

Both two- and three-dimensional micro-assembly are in great need for mass production of micro-devices. For example, a radio frequency identification (RFID) tag consists of a silicon micro-chip and an antenna. The antenna powers the tag and exchanges data between the chip and a neighboring RFID reader. The key to efficient fabrication of RFID tags lies in the rapid assembly of the small, more expensive silicon micro-chips with the larger, cheaper antenna substrate. Another example for micro-assembly is “smart dust”, i.e., collections of tiny distributed nodes that integrate sensing capabilities with signal processing and can organize into a communications network. These systems are already appearing as commercial products, and micro-assembly techniques play a very important role in mass production of such micro-scale devices.

### *1.1.2 Monolithic Fabrication vs. Heterogeneous Integration*

Monolithic fabrication constructs a whole device step by step from a single substrate. Heterogeneous integration constructs a device by combining various components from different techniques or processes. For devices with simple structures, monolithic fabrication has advantages such as compact layout and easy encapsulation. But many fabrication processes and materials are not compatible with one another, and thus micro-devices having complex functionalities or structures must be constructed by heterogeneous integration of multiple units from several different fabrication processes.

Additionally, heterogeneous integration has another significant advantage for product developers. A complex microsystem can be broken down into multiple distinct units. Each unit is then assigned to a separate process engineer or group. Each unit can be separately optimized in design and fully characterized before integration. Units of the same type can be fabricated at the highest spatial density on a single substrate to save fabrication costs.

### *1.1.3 Packaging: Die-Level vs. Wafer-Level*

Typically, packaging of micro-devices includes three process steps: (1) placement of micro-devices with correct face and in-plane orientations on receptor sites; (2) permanent bonding of micro-devices with electrical interconnections to the substrate; (3) encapsulation of the bonded device components for protection from the environment. Die-level packaging assembles individual micro-components after they are singulated from a wafer. Wafer-level packaging simultaneously assembles all the devices on the same substrate before they are singulated into individual devices, i.e., the wafer-level packaging process is parallel assembly whereas die-level packaging is serial assembly.

## **1.2 State of the Art in Micro-Assembly**

### *1.2.1 Surface Mount*

Surface mount technology (SMT) was fully established in the 1980s, when circuits became more and more complex so that through-hole component-mounting techniques were no longer economically or technologically feasible. The limitations of conventional PC-board technology motivated circuit design engineers to develop SMT. SMT keeps components and their interconnecting leads on one PC-board surface, rather than feeding the component leads through the circuit board. SMT employs solder to provide electrical and mechanical connections between components and PC-boards.

Compared with conventional through-hole mounting techniques, SMT possesses many prominent benefits such as reduced component size, increased circuit density, reduced PC-board size, reduced weight, increased interconnecting leads density, and improved high-frequency performance. No single electronic assembly technology is perfect to satisfy all circuit-design constraints. Current SMT also has some significant limitations such as poor heat dissipation, thermal mismatch, and decreased mechanical bonding strength of solder.

### *1.2.2 Robotic Assembly*

Robotic assembly is widely used in industry to assemble a variety of components. This assembly approach has three major steps: (1) part feeding, (2) pick and place, (3) affix in specified position and orientation. During a typical part feeding step, randomly agitated components move through a series of mechanical filters so that finally, they will show appropriate face and in-plane orientations. Then robotic grippers pick up these components and transfer them to targeted sites to complete the assembly. This is a serial assembly process.

Different part feeding mechanisms are required by various types (geometry or material fragility) of components. Flat silicon micro-components are a big challenge for

part feeding since they are symmetrical except for negligible differences in geometric features on some surfaces, such as interconnecting pads.

### *1.2.3 Self-Assembly*

Self-assembly techniques for component-to-substrate assembly are mainly based on energy minimization (Figure 1.1). A substrate is patterned with an array of energy traps. The types of energy traps include gravitational, interfacial, electrostatic and magnetic energies. On an assembly substrate, agitated components are attracted to these energy traps and then permanently attached. Thus, components self-assemble to receptor trap sites on the substrate.

Compared with SMT and robotic pick-and-place assembly methods, self-assembly techniques have several major advantages such as easy handling of components with size in micro-domains, fast parallel assembly, and self-alignment with high accuracy.

## **1.3 Self-Assembly Techniques**

### *1.3.1 Deterministic vs. Stochastic*

Parallel micro-assembly approaches, aiming to achieve highly efficient assembly of a very large number of micro-components, can be classified into two major categories: deterministic and stochastic. In a deterministic assembly process, each part is assigned to a certain receptor sites, e.g. wafer-to-wafer transfer of microstructures. In a stochastic assembly process, each part can be attached to any of the specifically designed identical receptor sites. People usually use the term “self-assembly” to describe such stochastic assembly approaches, owing to the property that the assembly takes place in a spontaneous manner with components of a specific design.

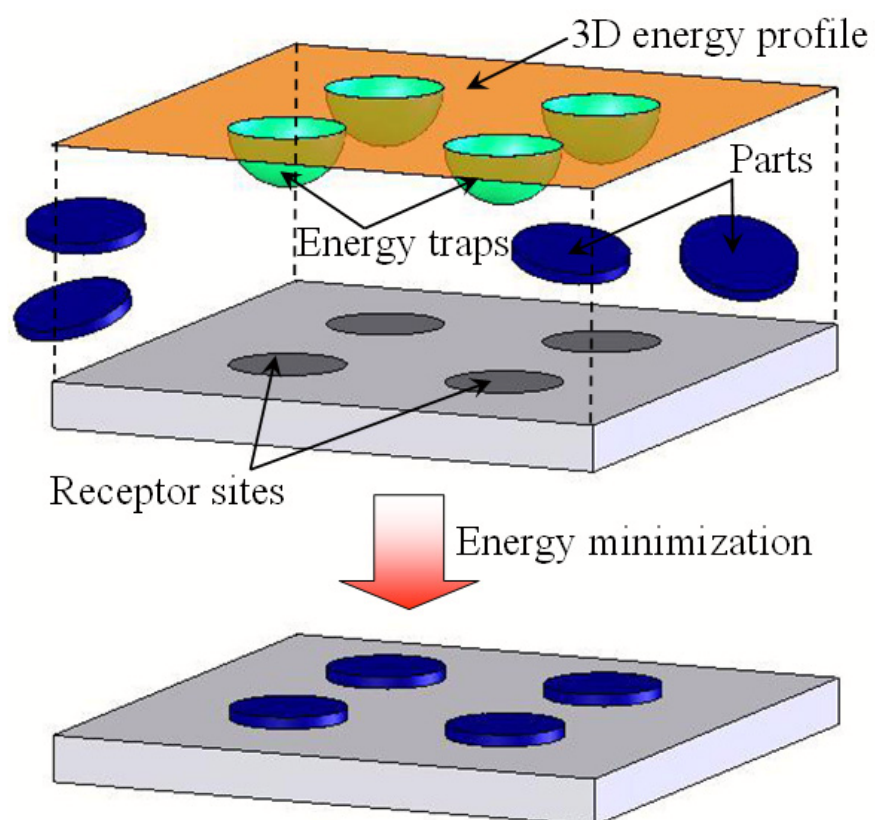


Figure 1.1: Schematic diagrams showing a typical self-assembly process based on energy minimization.

### *1.3.2 Serial vs. Parallel*

The number of parts assembled at a time on a single platform defines the property of an assembly process: serial or parallel. In a serial assembly process, only one part is assembled at each time, as in, e.g., robotic pick-and-place assembly methods. In a parallel assembly process, multiple parts are assembled simultaneously, which can achieve a higher throughput. Both wafer-to-wafer transfer of micro-components and self-assembly are parallel processes.

### *1.3.3 2D-Conformal-3D*

A two-dimensional conformal self-assembly process positions micro-components onto a rigid or flexible substrate, and the flat components attach directly to the substrate, i.e., assembled components are conformal with the substrate surface. This is the most common type of self-assembly, since patterning of energy traps on a substrate is straightforward with current micro-fabrication and surface treatment techniques.

Three-dimensional self-assembly of micro-components poses more challenges to currently available micro-fabrication techniques than two-dimensional self-assembly. Some simple three-dimensional microstructures have been constructed by self-assembly processes based on shape matching and interfacial energy minimization [ZBJ04,GTB<sup>+</sup>00], but this bottom-up fabrication method for complicated three-dimensional microstructures still requires more break-through innovations in micro-fabrication techniques and assembly mechanisms.

### *1.3.4 Hard-Coded vs. Programmed*

Based on whether the probability for parts to attach to receptor sites can be adjusted by varying conditions, self-assembly processes can be categorized into hard-coded or programmed types. In a hard-coded assembly process, each receptor site has a constant probability to attach a part at any time. In a programmable assembly

process, a receptor site has different affinities for a part under different conditions such as assembly environment and surface hydrophobicity, i.e., a receptor site can be turned on (an energy trap) or off (at the same energy level as its background or even higher). A typical usage of programmed self-assembly is to integrate different types of micro-components on an array of receptor sites patterned by a single fabrication process.

### 1.3.5 *Electrostatic and Electromagnetic Self-Assembly*

#### *Electrostatic 2D Assembly*

Electrostatic 2-D assembly is based on electrostatic attraction of micro-components, and the electrostatic attraction comes from polarization of the micro-components in electrical fields. According to Coulomb's Law, electrostatic force is inversely proportional to the square of the distance between charges, and thus it is a short-range interaction. Patterned surface areas with charges or localized electrical fields can be binding sites for micro-components, and the binding strength increases with surface charge density or electrical field intensity.

Tien et al. exploited electrostatic interactions to direct patterning of  $\text{\O}10\mu\text{m}$  gold disks on functionalized substrate surfaces [TTW97]. They fabricated the small charged gold disks by electroplating gold into photoresist molds and derivatizing these disks with charged self-assembled monolayers, and patterned the planar or curved substrate with surface charges by microcontact printing or photolithography. By agitation, the charged gold disks aggregated on the regions presenting the opposite charges. Finally they obtained selective and dense assembly in solutions such as methanol, ethanol, IPA and dioxane.

Cohn et al. demonstrated a self-assembly process with aligning capabilities over electrostatic traps [CHP95]. The experiment proceeded in an aqueous environment. The electrostatic traps were fabricated on a silicon substrate: a layer of  $2\mu\text{m}$  LTO

(Low Temperature Oxide) was first deposited using LPCVD as a dielectric layer, and then a layer of Au was deposited and patterned with an array of apertures (the size ranged from  $2\mu\text{m}$  to  $100\mu\text{m}$ ). The silicon substrate and the Au layer act as two driving electrodes, which resulted in fringing electric fields from the patterned apertures in the Au layer. If the micro-components stick to the substrate or each other, there will be no way to distribute or assemble them to the specified binding sites or electrostatic traps on the substrate. They proposed and demonstrated a method to avoid such sticking phenomena by levitating the micro-components a short distance ( $0\sim 100\mu\text{m}$ ) above the target electrostatic traps before letting them settle, and thus accurate placement and orientation of the micro-components with respect to the binding traps became feasible with a relatively low applied field of  $\sim 10\text{V}/\mu\text{m}$ . Each micro-component (a  $\text{SiO}_2\text{-pSi-SiO}_2$  sandwich) has an average dielectric constant of 10, and the assembly liquid environment was hexane with a relatively low permittivity, therefore, micro-components are easily attracted to the charged electrodes. The levitation of micro-components was achieved by adding a small amount of a more polar solvent (acetone, with a relatively high dielectric constant of  $\sim 20$ ), i.e., acetone shielded the electric field from the micro-components and prevented contact between micro-components and the binding sites. When all trap sites were occupied with “floating” micro-components, the polar solvent was titrated out to lower the micro-components to contact trap sites. Finally, permanent bonding can be accomplished with sintering metals.

Fringing electric fields out of patterned apertures on a substrate can be exploited to assemble micro-parts in an air environment [BGC<sup>+</sup>98]. A glass substrate was coated with a layer of Cr/Au and the Cr/Au was patterned with an array of square holes to expose glass underneath. The glass substrate was mounted on an aluminum vibratory platform driven by a piezoelectric actuator. Bulk parts were placed on the glass substrate. For effective agitation of these parts (initially parts tended to stick to the substrate and to each other because of the combination of electrostatic interaction,



capillary and van-der-Waals forces), the vibrating frequency was chosen in the 20kHz range. A DC voltage was applied on the aluminum platform and the Au electrode, and the resulting fringing electric field from the apertures in the upper electrode induced polarization in electrically neutral parts and caused them to be attracted to the apertures. When a part covered an upper electrode aperture, the fringing electric field was significantly reduced, which prevented attraction of more parts to this occupied site. Assembly experiments were performed in both air and low vacuum, and the results indicated that the required vibrating energy to overcome adhesive forces decreased with air pressure, probably due to squeeze film effects [Fea95a], and due to the vacuum created between the flat part bottom surface and the substrate when operated at ultrasonic frequencies.

#### *Towards 3D by Triboelectricity*

Kaajakari and Lal demonstrated a method based on triboelectricity for batch assembly of polysilicon hinged structures [KL01]. Triboelectricity on hinged plates and the substrate was achieved by use of ultrasonic vibrations generated with an attached piezoelectric actuator to vibrate polysilicon plates on silicon nitride or polysilicon substrate surfaces. Such contact electrification charge resulted in hinged flaps to be stabilized vertically on the substrate. Furthermore, they also observed a “memory effect” in which assembly occurred even without further ultrasonic vibration after the initial ultrasonic assembly.

#### *Magnetic Assembly*

Magnetic force is a type of short-range interaction and can be utilized to attach micro-components to certain magnetized sites on a substrate. Perkins et al. developed a new assembly approach called Magnetically-Assisted Statistical Assembly (MASA) [PRF02]: the compound semiconductor device heterostructures, “nanopills” covered with a soft magnetic material, were trapped to the shallow recesses patterned

into the surface of an integrated circuit wafer, and the short range magnetic attractive forces kept the parts in the recesses. The nanopills were agitated with liquid flow. The magnetic force per unit area drops exponentially with the increasing separation between a part's permalloy surface and the magnetized Co-Pt stripes at the bottom of a recess.

Magnetic fields can also be exploited to construct three-dimensional microstructures. Iwase et al. demonstrated a sequential batch assembly method based on magnetic field assisted self-assembly [IS05]: an external magnetic field perpendicular to the substrate was used to lift hinged ferromagnetic microstructures, and the magnetic field was increased gradually so that a plate with softer hinges was lifted first. The softness of a plate's hinge can be controlled by adjusting the length and number of the hinge beams.

### *1.3.6 Fluidic Shape-Directed Self-Assembly*

Fluidic self-assembly, developed by Yeh and Smith in 1994, relied on shape matching between micro-components and recessed receptor sites [YS94]. Bulk micro-components were agitated by liquid flow until they fell into receptor holes. GaAs vertical-cavity surface-emitting laser components were demonstrated to be integrated on a silicon substrate. The silicon host substrate was patterned with etched holes of a trapezoidal shape (the trapezoidal features resulted from anisotropic wet chemical etching of  $\langle 1 - 0 - 0 \rangle$  silicon substrates), and the GaAs light emitting diode (LED) components were also of the same trapezoidal shape. Carrier fluid containing the GaAs micro-components was dispensed over the host silicon substrate. Because of the trapezoidal shape design, the GaAs blocks fit preferentially into the holes in the desired face orientation. Random mechanic vibration was performed to enable large numbers of micro-parts to be positioned into precise registration with the recessed receptor sites. Greater than 90% of the etched holes on the substrate were correctly filled with the GaAs blocks before the carrier fluid evaporated.

Alien Technology Corporation has commercialized this fluidic self-assembly technique. Fluidic self-assembly can work on either rigid (glass or plastic) or flexible (polyester, polyimide, polycarbonate and etc.) substrates. They have been using fully automated in-line reel to reel (web) processing on a continuous flexible substrate. Fluidic self-assembly and web processing offer many advantages over conventional processing on rigid substrates, e.g., (1) reduced manufacturing facility investment; (2) reduced material and manufacturing costs; (3) increased manufacturing through-put.

Stauth et al. also used a fluidic self-assembly technique to integrate silicon micro-components on a plastic substrate [SP05]. Receptor wells on the plastic substrate were formed with lithographically patterned thick SU8. At the bottom of these receptor wells, electrical terminals were coated with low temperature melting solder. Correspondingly, interconnect pads on silicon micro-components are patterned Au areas with high solder-wetting capability. In a hot and acidic aqueous environment, micro-components slid on the tilted substrate and fell into receptor wells, and then micro-components were anchored when their interconnect Au pads contacted melting solder droplets in the wells.

### *1.3.7 Centrifugal Force Driven Self-Assembly and Towards 3D*

Inertial forces, e.g. gravity, are usually neglected for micro-scale components when compared with surface forces such as surface tension and electrostatic forces. As an inertial force, a centrifugal force can be increased to overcome surface forces because it is proportional to the square of the rotating speed. Lai et al. demonstrated non-contact batch assembly of 3D microstructures by centrifugal force: hinged microstructures fabricated in a MUMPs process were assembled with the help of latching features [LHL02].

### 1.3.8 Capillary-Driven Self-Assembly

#### *Towards 3D Assembly with Solder/Photoresist Reflow*

In micro-domains, surface tension forces dominate over gravitational forces, and have been explored and exploited by some researchers to lift up hinged plates to construct three-dimensional structures. To achieve such a type of 3D assembly, one usually deposits and patterns a thick layer of solder or photoresist at the joint of hinged structures. When the solder or photoresist is reflowed, it changes into a spherical shape to minimize interfacial energies (a spherical shape has the minimum surface-to-volume ratio), and thus the hinged plate attached to the reflowed droplet rotates. With appropriate latching features, some complex 3D microstructures can be constructed [HIL98, HBL99].

Yang et al. developed a method to achieve local assembly by reflowing solder with magnetic induction welding [YLF05]. The heating temperature depends on the area of a layer of magnetic film underneath the solder, and thus different heating temperature regions on a substrate can be photolithographically defined (the magnetic field is assumed to be uniform across the substrate). They demonstrated this local reflowing technique with separating Ni plates from underneath Ti plates.

Zheng et al. used low temperature melting solder to construct some functional LED micro-components which had three-dimensional structures including a LED component, a chip carrier with solder bumps, and an encapsulation body with solder bumps [ZBJ04]. Following is the assembly sequence: (1) LED components and chip carrier components were put in a hot and acidic liquid environment, and then tumbling agitation caused each LED component to mate with a chip carrier component, finally, mated components with the solder bonding were sorted out; (2) mated components from the previous step were placed in a hot and acidic liquid environment together with encapsulation components for another batch assembly.

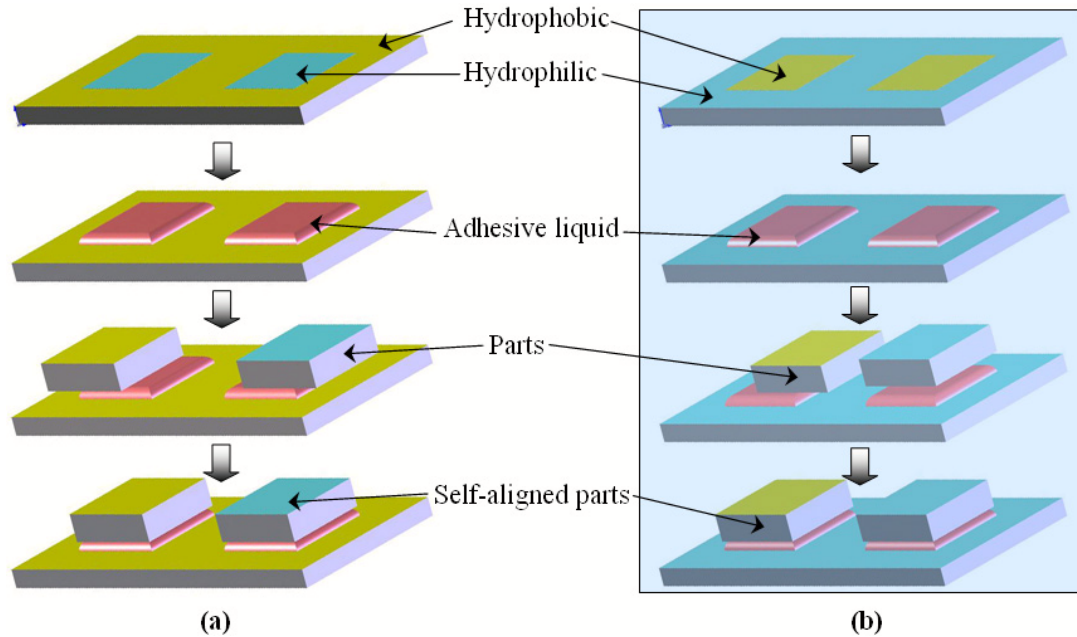


Figure 1.2: Schematic overviews of capillary-driven self-assembly: (a) in an air environment; (b) in an aqueous environment.

### *Parallel 2D Assembly*

In capillary-driven 2D self-assembly processes, agitated flat micro-components contact and attach to adhesive liquid droplets on receptor sites, and then self-align to receptor sites to minimize interfacial energies. Depending on the assembly environments, capillary-driven self-assembly processes can be grouped into two categories: in an aqueous environment and in an air environment. Different adhesive liquids require different hydrophilicity or surface coatings for the receptor sites. For an acrylate-based adhesive liquid, receptor sites should be hydrophobic for aqueous assembly environments and hydrophilic for air assembly environments, respectively (Figure 1.2). For low temperature melting solder, receptor sites should be thin film metals with good solder-wetting capability, e.g., copper and gold.

Low temperature melting solder can be used to assemble flat micro-components

with both electrical and mechanical connections onto a substrate. Jacobs et al. developed a self-assembly process to mount LED arrays on flexible cylindrical templates by low temperature melting solder [JTS<sup>+</sup>02]. The assembly template was patterned with copper squares, and a simple dip coating process left melting solder on these copper squares since copper has very good wetting capability for solder. The dip coating process proceeded in an acid aqueous environment to avoid oxidation of melting solder. Since a LED segment has electrical polarity, i.e., it can only be lighted up with an appropriate positive DC bias, two electrodes on either side of each LED segment should be distinguished with some pattern: the gold covered the whole bottom surface and 1/9 of the top surface. Hundreds of LED components and a flexible assembly template were placed inside a vial full of water at a temperature above the melting point of the solder. The LED components were tumbled inside the vial, and then they were attracted, aligned and bonded to the receptor sites on the template by the surface tension forces of the melting solder. By controlling the agitation intensity, only the bottom surfaces with 100% covered gold instead of the top surface with 1/9 covered gold were bonded to solder droplets because the adhesion is roughly proportional to the gold covering area on the LED segments. Therefore, the LED components self-assembled with unique face orientations. Gold pads on the top surfaces of the bonded LED components were coated with melting solder by another dip coating. As a final assembly step, a flexible transparent film patterned with electrical circuits and solder bumps was roughly and manually aligned to the assembly template, i.e., a wafer-level flip-chip bonding process, and the film was aligned with high accuracy to the assembly template by surface tension of the melting solder. Therefore, the electrical connections to the top electrodes of the LED segments were established. Assembly was successful by testing with a low defect rate of  $\sim 2\%$ .

Srinivasan and coworkers developed and demonstrated another fluidic self-assembly technique [SLH01, SHR<sup>+</sup>02]. They patterned a substrate with an array of hydrophobic thiolated Au binding sites. When the substrate was inserted into water through a

film of hydrophobic adhesive floating on the water surface, the adhesive covered only the hydrophobic binding sites. Then they introduced micro-parts fabricated from silicon-on-insulator wafers to the substrate in the water with a pipette. When the hydrophobic pattern on the micro-parts came into contact with the adhesive, shape matching occurred spontaneously due to interfacial energy minimization. Finally the adhesive was polymerized by heat or UV light depending on the type of the adhesive, so that the bonding became permanent. Binding sites of shapes with in-plane rotational symmetries such as squares gave alignment yields up to 100%. The translational and rotational misalignments were less than  $0.2\mu\text{m}$  and within  $\sim 0.3^\circ$ , respectively. Binding sites without in-plane rotational symmetries (aiming for uniquely oriented alignment) such as semicircles and commas gave alignment yields of approximately 30-40%.

To achieve self-assembly with unique in-plane orientations, Liang et al. designed and demonstrated a capillary-driven self-assembly process with special geometrical designs for binding sites [LXB]. Both the parts and binding sites are of an offset ring shape, which provides a unique global interfacial energy minimum: the interfacial energy calculation is based on the assumption that the interfacial energy is approximately in a linear relationship with the overlap area between a part and a binding site [BSH01].

To introduce bulk micro-components to receptor sites during capillary self-assembly in an air environment, Liang et al. developed a method using an agitated diaphragm to bounce micro-components until some were caught by water droplets on the receptor sites on the downward-facing assembly substrate [LWB]. This process demonstrated fast assembly ( $<30\text{sec}$ ) and high yields ( $>90\%$ ), and fast recycling of redundant components. The glass substrate was coated with hydrophobic thiolated Au, which was patterned with an array of openings (exposure of the glass substrate). The exposed glass receptor sites were hydrophilic and covered with water droplets after a dip coating process. The capillary-driven alignment was a sub-second process.

*Multi-Batch Assembly*

Xiong et al. demonstrated a method for controlled multi-batch self-assembly of micro-components by capillary force [XHF<sup>+</sup>03]. They patterned an oxidized silicon substrate with an array of gold binding sites, and these gold binding sites became hydrophobic after adsorbing a self-assembled monolayer (SAM) from an alkanethiol solution. The self-assembly process proceeded in an aqueous environment. To be active, i.e., to adsorb an adhesive liquid droplet for later anchoring of micro-components, a binding site should be hydrophobic. Without a SAM, Au binding sites are hydrophilic as their background is and inactive for assembly of micro-components. They demonstrated an electrochemical method to desorb the SAM from the gold binding sites: an appropriate electrochemical potential was applied between the gold binding sites and an aqueous environment. Before the first batch assembly, some binding sites were selectively deactivated by SAM desorption, to be reactivated for the next batch assembly. An array of commercial LED components was assembled to the substrate with the heat polymerizable adhesive, and the electrical connections between the substrate and the LED components were established with solder electroplating at two diagonal corners of each binding site. With such programmable multi-batch assembly capabilities, one can fabricate versatile microsystems by integrating various types of micro-components.



## Chapter 2

### CONCEPTS AND MATERIALS

#### **2.1 MEMS Packaging**

Microelectromechanical systems (MEMS) are integrated systems of sensors, actuators and electrical circuits built with micro-fabrication techniques. Sensors extract useful information from their environment by measuring mechanical, thermal, biochemical, optical, radiation and/or electromagnetic responses. Electrical circuits process the collected information and send out control signals to direct actuators to respond by moving, positioning, regulating, pumping and filtering, thereby controlling the environments for some desired outcomes. Sensors can be classified by their applications as: acoustic sensors, mechanic sensors, magnetic sensors, radiation sensors, thermal sensors, chemical sensors, bio sensors and integrated sensors [SZE94]. Actuators can be categorized by their driving mechanisms as: thermal actuators, optical actuators, electrical actuators, magnetic actuators, chemical and biological actuators [Kov98]. The micro-fabrication techniques used for MEMS construction can be broadly categorized as: (1) lithography; (2) pattern transfer with dry etching techniques; (3) pattern transfer with additive techniques; (4) wet bulk micromachining; (5) surface micromachining; (6) LIGA and others [Mad97].

Packaging is a very important step in the fabrication of MEMS devices. Usually interconnect pads on a micro-device chip are too closely spaced to accommodate the interconnection capacity of a traditional printed wiring board, therefore a packaging process should redistribute the interconnect pads over a larger and more manageable surface. A typical packaging theme for MEMS components based on surface mounting

techniques is schematically shown in Figure 2.1, and achieved in three major steps: positioning, bonding and encapsulating. Positioning requires accurate placement, as well as correct face and in-plane orientations. Two conventional bonding methods are wire bonding and flip-chip bonding, and the interconnecting face orientation of the MEMS component depends on the bonding method. Encapsulating protects the assembled devices from possible harsh working environments. More than 70% of a sensor's cost may be determined by its package, and the physical dimension of the sensor is often much smaller than its package size because most of the conventional packaging techniques are space inefficient [Mad97].

No standard packaging theme is suitable for any MEMS device since MEMS devices have a very broad range of application types such as: RF-MEMS, optical-MEMS, and bio-MEMS. Each type of MEMS devices requires a unique packaging theme based on several factors such as process and material compatibilities, heat dissipation, hermetic sealing or open systems, compact volume and cost. However, among the three major packaging steps, positioning has the least dependence on the MEMS device type. Rapid positioning is critical for mass production of MEMS devices, which is the major motivation for us to develop self-assembly techniques.

## ***2.2 Self-Assembly Processes***

Initially the concept of self-assembly came from chemical and biological formation of micro- and nano-scale structures. During recent decades many researchers have shown great interests in constructing two- or three-dimensional patterns or structures by exploiting self-assembly processes: micro-components and substrates are engineered to have patterns of hydrophobicity or other surface properties, and then self-assembly takes place among these engineered surfaces to minimize total energies.

This dissertation research has been focused on two-dimensional self-assembly processes which parallel mount flat micro-components on flat substrates. The mount-

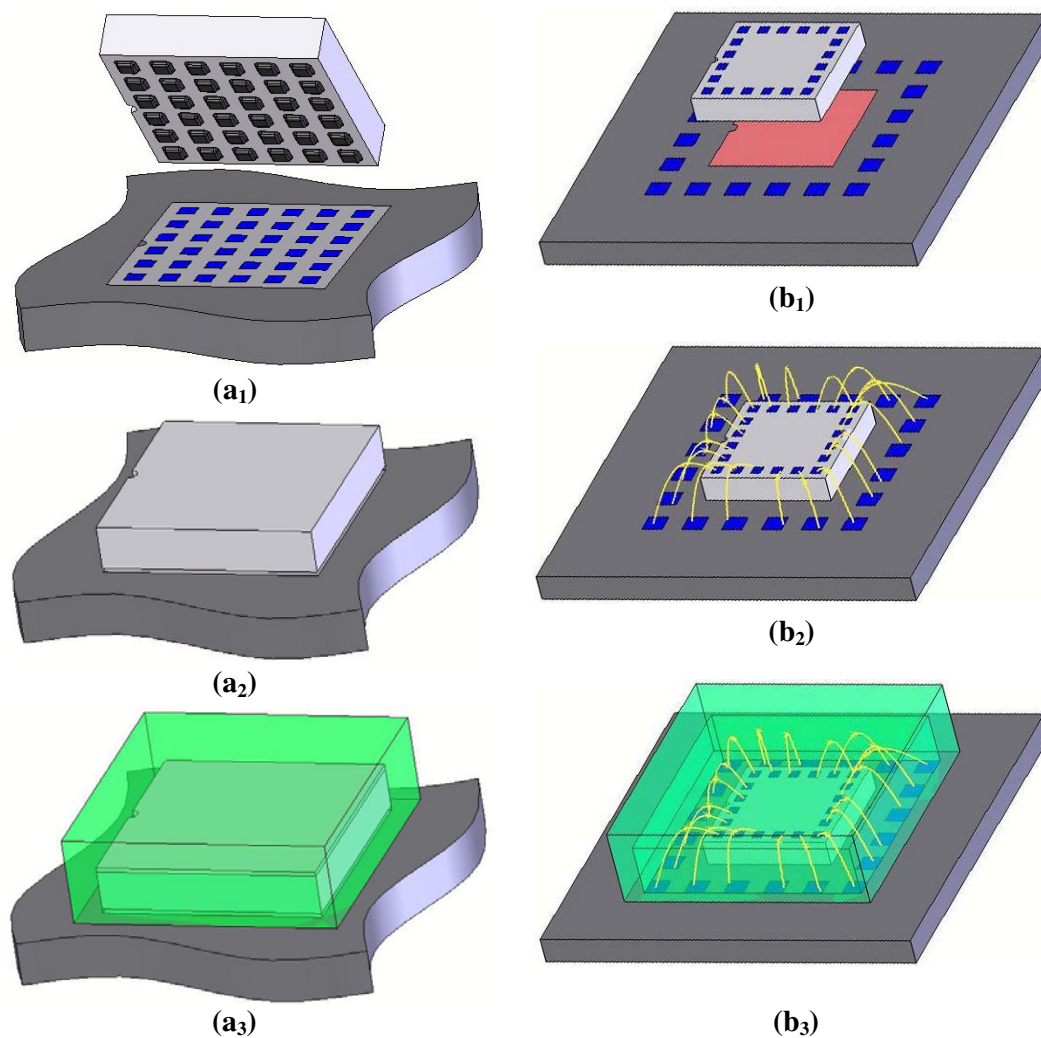


Figure 2.1: Schematic overviews of typical MEMS packaging processes: (a<sub>1</sub>) a rectangular component having an array of solder bump interconnects is placed onto a binding site having metal contacts, and aligned with a correct in-plane orientation indicated by the polarity marks; (a<sub>2</sub>) flip-chip bonding is achieved after correct positioning of the component; (a<sub>3</sub>) the bonded component is encapsulated in a hard body for protection from the environment; (b<sub>1</sub>) a component is placed, aligned and glued to a binding site; (b<sub>2</sub>) wire bonding is achieved to establish all the electrical interconnections from the component to the chip carrier; (b<sub>3</sub>) the assembled component is protected by an encapsulating body.

ing process is a critical step for packaging of micro-devices. Parallel and rapid manipulating of micro-components can enable mass production of micro-devices, thus self-assembly processes have significant advantages over serial robotic pick-and-place assembly methods.

To achieve efficient self-assembly processes, one should take the following factors into account:

**One-to-one registration:** each receptor site adopts exactly one component.

**Part redundancy and recycling:** redundant components improve the assembly yield in a certain period of time, and the redundant components can be collected for reuse in the next run of the self-assembly process.

**Orientation:** components should have correct face and in-plane orientations so that electrical interconnections between the components and the chip carrier can be easily established via wire bonding or flip-chip bonding.

**Surface coverage:** surface coverage, a ratio between receptor sites' area and total substrate area, is a very important factor for some applications such as LED displays (each pixel is a LED component).

**Programmability:** receptor sites are turned on and off for assembly of components by adjusting control signals on individual receptor sites, and thus multiple types of components can be integrated on the same assembly substrate by multiple batches self-assembly.

### **2.3 Self-Assembled Monolayers**

Self-assembled monolayers (SAMs) are widely used to modify surfaces with well-defined chemical composition for a variety of applications such as micro fluidic channels, biomaterial and biosensor surfaces. There are different types of SAMs for different surfaces [Ulm96]: alkanethiols on gold, silver and copper surfaces [LWA<sup>+</sup>91], octylsiloxane SAMs on silicon dioxide [YBJ<sup>+</sup>97], alkane-phosphates on a number of

transition metal oxide surfaces such as titanium oxide, tantalum oxide and niobium oxide.

Alkanethiol SAMs  $\text{CH}_3(\text{CH}_2)_n\text{SH}$  on Au are well understood [Ulm96, SUSE93, KF04] and have been widely used for patterning a substrate with hydrophobic gold areas. When an Au surface is submerged in an alkanethiol solution for an appropriate period of time, the alkanethiol molecules are chemically adsorbed to the Au surface by their -SH groups and form a monolayer with the hydrophobic  $-\text{CH}_3$  groups at the outside surface. The chain length of alkanethiols determines the properties of the monolayer: the longer chain, the more densely packed monolayer, and the higher stability [XHF<sup>+</sup>03]. In our experiments, we use only one type of alkanethiol,  $\text{CH}_3(\text{CH}_2)_{11}\text{SH}$ , to treat Au surfaces: it is a liquid form alkanethiol, and easily dissolved in ethanol to form a solution for the Au surface treatment.

## ***2.4 Hydrophobic and Hydrophilic Surfaces***

Hydrophobicity and hydrophilicity are two types of solid surface properties and defined on the basis of water wetting characteristics. Intermolecular bonds or cohesive forces between water molecules cause surface tension. When water encounters a solid substrate, there is usually attraction between the two materials. The adhesive forces between water and the substrate compete against the cohesive forces in the water: (1) when the adhesive forces are stronger than the cohesive forces, water tends to spread over the substrate; (2) when the adhesive forces are weaker than the cohesive forces, water tends to bead-up or form a droplet on the substrate. Viewing from molecular scales, the type of chemical molecular groups at a surface determines the hydrophobicity or hydrophilicity. Water molecules are polar (positive and negative charge centers are separated), therefore they like to attract polar chemical groups. Polar groups such as -OH can form hydrogen bonds with water molecules, thus a surface having such groups shows hydrophilicity. A surface coated with apolar groups such as  $-\text{CH}_3$  or

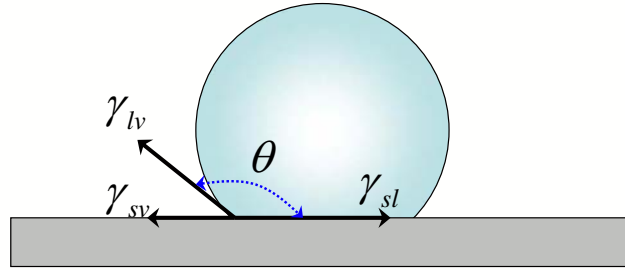


Figure 2.2: Schematic side view of a liquid droplet sitting on a solid surface with a contact angle  $\theta$  determined by interfacial energies  $\gamma_{sl}$ ,  $\gamma_{sv}$  and  $\gamma_{lv}$ .

-CF<sub>3</sub> shows hydrophobicity because interactions among water molecules are stronger than those between water molecules and the surface apolar chemical groups.

Hydrophilicity or hydrophobicity of a solid surface can be characterized by contact angle measurement: a water droplet is dispensed onto the solid surface, and then the contact angle is measured based on a side view of the droplet. Water contact angles are greater and less than 90° on hydrophobic and hydrophilic surfaces, respectively. The contact angle  $\theta$  is determined by the interfacial energies according to Young's Equation (Figure 2.2):

$$\gamma_{sv} = \gamma_{sl} + \gamma_{lv} \cos(\theta) \quad (2.1)$$

Where  $\gamma_{ij}$  is interfacial energy between substances  $i$  and  $j$ : the subscripts  $s/v/l$  respectively stand for the solid substrate, vapor environment and liquid.

## 2.5 Bonding Methods

Bonding is an important process step for packaging of micro-devices. Bonding provides mechanical and/or electrical connections between micro-components and the substrate. Conventional bonding techniques to attach two flat objects can be classified into two categories: direct and indirect bonding.

### 2.5.1 Direct Bonding

Direct bonding techniques attach two flat objects without any intermediate layer, and their examples are: (1) anodic bonding between pyrex and silicon; (2) fusion bonding between silicon and silicon.

**Anodic bonding**, also referred as field assisted glass-silicon sealing, bonds sodium-rich glass to silicon: a typical operating temperature is between 180°C and 500°C, and typical DC voltages range from 200V to 1200V depending on the thickness of the glass wafer and the operation temperature. For minimum thermal mismatch, the glasses should have thermal expansion coefficients very close to that of silicon. The examples of such glasses are: Corning 7740 (Pyrex) and 7070, Schott 8330 and 8329, and 7570 (Iwaki) types. The experimental setup is shown in Figure 2.3. At a rising temperature, positive sodium ions in the glass substrate have an increased mobility, and are gradually depleted from the glass through the top cathode electrode. The remaining negative bound ions in the glass form a space charge layer near the silicon surface, and thus a significant electrical potential drop occurs at the glass/silicon interface. The resulting electric field brings two substrates to contact. Permanent chemical bonding occurs and begins from directly below the cathode, and then spreads across the interface.

**Fusion bonding** bonds two silicon wafers based on the chemical reaction between OH-groups present at the surface of native or grown oxides covering the wafers: the wafer bonding can be achieved by placing two wafers in close contact at an oxidizing ambient and an operating temperature greater than 800°C. The resulting bonding has almost no thermal stress because the thermal expansion coefficients of the two substrates are identical.

Both anodic bonding and fusion bonding require very clean and flat substrates. Micro-particles at the bonding interface will form voids which can affect applications for some types of devices. A high degree of flatness of both surfaces ensures them to

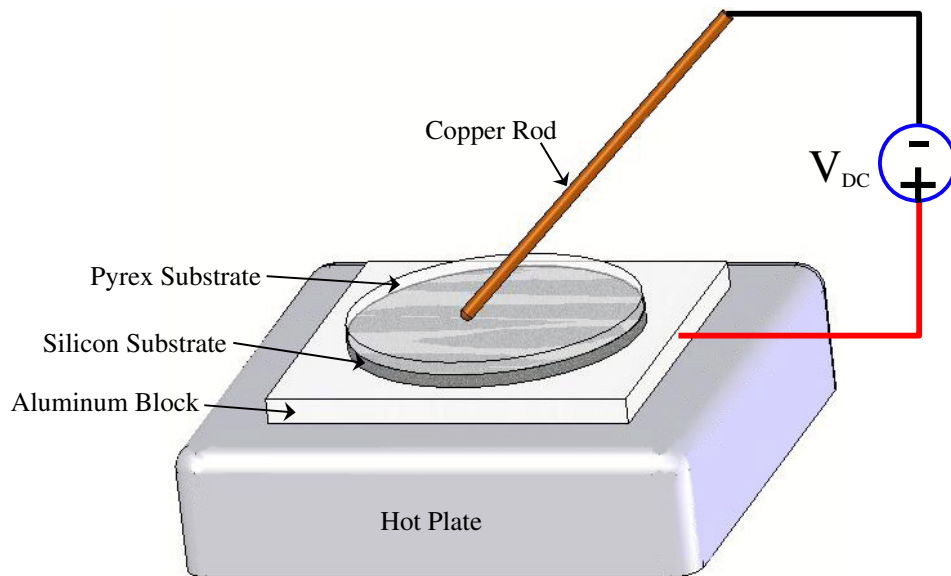


Figure 2.3: Schematic view of a typical anodic bonding setup.

contact fully so that bonding occurs across the interface.

### 2.5.2 Indirect Bonding

Indirect bonding techniques rely on intermediate layers which are reflowable or sticky. Typical examples for wafer bonding are: glass frit bonding, thermocompression bonding, adhesive bonding, solder bonding and eutectic bonding.

**Glass frit bonding:** The intermediate layer is a kind of low melting point glass, which can be applied by preforming, spin-on, screen printing, sputtering, etc., and patterned to define bonding areas. The bonding processes are typically carried out in the temperature range of 400-650°C and contact pressures of  $\sim 10^5$  Pa. For less thermal residual stress, the thermal expansion coefficient of the glass is normally chosen to be between the two values for the wafers being bonded.

**Thermocompression bonding:** The intermediate bonding material is a soft



metal deposited on both substrates. For MEMS applications, the most common metal is Au with a suitable adhesion layer such as Cr. The bonding processes require moderate temperatures ( $\sim 300^\circ\text{C}$ ) and pressures (106Pa). This technique has very low outgassing and therefore is promising for vacuum sealing.

**Eutectic bonding:** The intermediate layer is a two-component system having the lowest melting point composition of the two components respectively on the two substrates to be bonded. Because the eutectic composition alloy at the interface has a lower melting point than either component and diffusion occurs at a limited depth, the melting is restricted to a thin layer at the interface. Typically used eutectic in MEMS applications is the Au/Si alloy (97.1 Wt % Au : 2.85 Wt % Si) with a melting point of  $363^\circ\text{C}$ .

**Solder bonding:** The intermediate layer is a low melting point metal alloy applied by various thin film deposition techniques such as thermal/ebeam evaporation and dip-coating. Typical alloys are Pb/Sn, Au/Sn and Cu/Sn. This bonding technique is highly tolerant to particles on surfaces and is most widely used for electrical interconnections, e.g., flip-chip bonding.

**Adhesive bonding:** The intermediate layer is a sticky adhesive. Typical adhesives for wafer bonding are epoxies, silicones, photoresists, polyimides, etc., and can be applied by spinning or spraying. For better bonding performance, heating and pressure are usually required. This bonding technique is also tolerant to particles on bonding interfaces, and its low process temperature benefits bonding or sealing some devices with severe temperature limitations. Conductive adhesives such as anisotropic conductive film (ACF) can be used to establish both mechanical and electrical connections. In our experiments, we used an acrylate-based adhesive, which is a liquid with water-like viscosity (storing in a refrigerator for slow aging effect) and completely polymerized by heating at  $\sim 80^\circ\text{C}$  for  $\sim 30\text{min}$ .

## Chapter 3

**CAPILLARY-DRIVEN SELF-ASSEMBLY****3.1 Introduction**

PZT actuators can convert electrical energy to mechanical energy with fast response and are widely used as driving elements for several types of micro fluidics devices such as micro pumps [FBA<sup>+</sup>95], micro mixers [YGMM00, JMH02] and micro dispensers [KBdR03], among others. Typically, PZT actuators are manually mounted onto a silicon, glass, or polymer substrate with batch-fabricated micro fluidic components using highly viscous silver epoxy, a slow serial process without good control of process parameters such as placement of PZT actuators, adhesive thickness and PZT actuator tilting; therefore this assembly process cannot achieve good repeatability and does not scale well to wafer level packaging.

Capillary forces have been exploited to assemble microstructures in two or three dimensions by several research groups [JTS<sup>+</sup>02, SLH01, SY93, HZBL99, SYBW03]. We previously reported capillary-driven self-assembly of surface mounted light emitting diodes (LEDs) in a water environment [XHF<sup>+</sup>03]: a hydrophilic substrate was patterned with hydrophobic binding sites, then adhesive liquid was dispensed across the substrate in air and wet only the binding sites when the substrate was submerged in the water, and the adhesive droplets on the binding sites attracted and aligned the introduced LEDs to minimize interfacial energies, finally the adhesive liquid was polymerized by heating for permanent bonding. This assembly technique has the following properties: (1) micro-components to be assembled are soaked in an aqueous environment for quite a long time; (2) the adhesive volume on each binding site

cannot be effectively controlled; (3) part tilting is hard to avoid [SHR03]; (4) bonding strength is poor because the binding site is hydrophobic with low interfacial energy, which will be demonstrated by a de-bonding test in Section 3.4.6; (5) electroplating is required to establish electrical connections from the substrate to the LEDs. To achieve good and repeatable performance for PZT driven devices, PZT actuators should be bonded with the following requirements: strong and tilt free bonding, accurate placement and precisely controlled adhesive thickness. These requirements indicate the above method to assemble LEDs cannot be the optimal choice to bond PZT actuators.

We have developed a novel method to bond PZT actuators with a well-controlled self-assembly process. This method is a parallel process in an air environment and provides controlled adhesive thickness, highly accurate placement and tilt free bonding. The bonding adhesive (an acrylate-based liquid) has very low viscosity and significant surface tension to align PZT actuators, and can be polymerized by heating to 85°C for about half an hour [SHR<sup>+</sup>02]. The adhesive only bonds PZT actuators mechanically because it is not electrically conductive. We use a design strategy with precisely recessed binding sites to establish mechanical bonding and electrical bonding, respectively, at the center and rim of a PZT actuator. This technique has been demonstrated by mounting PZT actuators for 28 diffuser valve micro pumps on a 4" pump substrate.

## **3.2 Capillary-Driven Self-Assembly Mechanism**

### *3.2.1 Interfacial Energy Minimization*

A schematic top view of a part captured but not yet aligned by a binding site via a layer of adhesive liquid film is shown in Figure 3.1:  $P$  stands for the bottom surface of a part,  $B$  for a binding site, and  $S$  for the binding site background. For most capillary-driven self-assembly processes,  $B$  and  $P$  are of an identical shape. Our self-

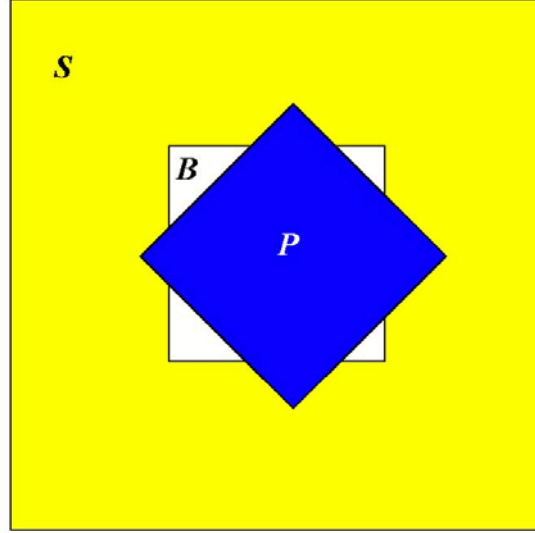


Figure 3.1: A schematic top view of a part  $P$  captured but not yet aligned by a hydrophilic binding site  $B$  with hydrophobic background  $S$  via a layer of adhesive liquid film.

assembly process in an air environment is assumed to have the following properties: (a)  $P$  and  $B$  are hydrophilic; (b)  $S$  is hydrophobic; (c) adhesive liquid exclusively and completely wets hydrophilic surfaces  $P$  and  $B$ , i.e., the small gap between  $P$  and  $S$  is also wetted. To estimate the total interfacial energy  $E$  of the arrangement in Figure 3.1, we observe that the adhesive film thickness is much less than the lateral size of  $P$  or  $B$ , and that interfacial energy is proportional to interfacial area. Therefore, the interfacial energy at the sidewalls of the adhesive film can be neglected, and total interfacial energy of this system can be approximated with:

$$\begin{aligned}
 E = & \gamma_{fp}|P| + \gamma_{fa}|B - P \cap B| + \gamma_{fb}|B| \\
 & + \gamma_{fs}|P \cap S| + \gamma_{sa}|S - P \cap S|
 \end{aligned} \tag{3.1}$$

Where  $\gamma_{ij}$  is interfacial energy between material  $i$  and material  $j$ , and subscript  $f$  stands for adhesive film,  $a$  for air, and  $p/b/s$  for surface  $P/B/S$ .  $|A|$  denotes the area of a surface  $A$ . The operators “ $\cap$ ” and “ $-$ ” are respectively geometric intersection

and difference. The terms of the right hand side of Equation (3.1) come respectively from the following interfaces: complete adhesive wetting of  $P$ ; part of adhesive on  $B$  that is exposed to air; complete adhesive wetting of  $B$ ; adhesive wetting of the part of  $S$  that is overlapped by  $P$ ; the part of  $S$  exposed to air.

Overlap area between  $P$  and  $S$  can be defined by:  $|P \cap S| = |P| - |P \cap B|$ . By replacing  $|P \cap S|$  in Equation (3.1), we can get:

$$\begin{aligned}
 E &= \gamma_{fp}|P| + \gamma_{fa}(|B| - |P \cap B|) + \gamma_{fb}|B| \\
 &\quad + \gamma_{fs}(|P| - |P \cap B|) \\
 &\quad + \gamma_{sa}(|S| - |P| + |P \cap B|)
 \end{aligned} \tag{3.2}$$

In Equation (3.2),  $|P \cap B|$  is the only variable factor depending on the position of  $P$  relative to  $B$ . By collecting the constant and the variable terms, we can rewrite Equation (3.2) as:

$$\begin{aligned}
 E &= [\gamma_{fp}|P| + \gamma_{fa}|B| + \gamma_{fb}|B| \\
 &\quad + \gamma_{fs}|P| + \gamma_{sa}(|S| - |P|)] \\
 &\quad - (\gamma_{fa} + \gamma_{fs} - \gamma_{sa})|P \cap B| \\
 &= C_1 - C_2|P \cap B|
 \end{aligned} \tag{3.3}$$

where  $C_1 = \gamma_{fp}|P| + \gamma_{fa}|B| + \gamma_{fb}|B| + \gamma_{fs}|P| + \gamma_{sa}(|S| - |P|)$  and  $C_2 = \gamma_{fa} + \gamma_{fs} - \gamma_{sa}$  are constants. Usually  $\gamma_{sa}$  is much smaller than  $\gamma_{fa}$ , which leads to a positive  $C_2$ . Therefore, the total interfacial energy is a linear function of the overlap area  $|P \cap B|$  with a minimum when  $P$  and  $B$  exactly align.

### 3.2.2 Self-Alignment of Rectangular Parts

According to Equation (3.3), the overlap area between a part and a binding site during self-alignment of the part provides a scalar value that can be used to find a final stable state. In practice, most micro-parts are rectangular because of easy mechanical

dicing along straight lines. During the following discussions, only rectangular parts are considered, but our analysis generalizes directly to parts of arbitrary shapes. Self-alignment motion of a part is a combination of translation and rotation. For simplicity, we visualize the overlap area  $|P \cap B|$  for translation and rotation separately: for translation (Figure 3.2a), the result shows a unique maximum overlap area when the part is exactly aligned with the binding site; for rotation (Figure 3.2b), the result indicates that the number of maximum overlap states or minimum energy states depends on the width-to-length ratio of the rectangular part: a square part has four preferred in-plane orientations with rotation angle intervals of  $90^\circ$ ; as the width-to-length ratio decreases, the overlap area peaks near  $90^\circ$  and  $270^\circ$  shrink and become valleys when the width-to-length ratio reaches approximately 1:1.3, thus a typical rectangular part has two preferred in-plane orientations.

Square PZT actuators can be aligned to any of the four in-plane orientations with minimum interfacial energy during an assembly process. A PZT actuator has two large opposite faces used as two electrodes, i.e., the bonding face has only one electrode. Electrical connections to the bonding face can be established correctly no matter which in-plane orientation with minimum interfacial energy the PZT actuator takes. Connection to the opposite, outward facing electrode can be achieved, e.g., with a wire bond.

### **3.3 Diffuser Valve Micro Pumps**

#### *3.3.1 Working Principle*

We choose diffuser valve micro pumps for the demonstration of PZT self-assembly because this type of pump is a good candidate to control the transport of liquids from microliters to nanoliters [WF01] and the diffuser valve is well understood [OSS99, HMB97, YCSW04]. The diffuser valve micro pump (Figure 3.3) consists of a large shallow chamber, two diffuser check valves, two channels connecting the valves and the

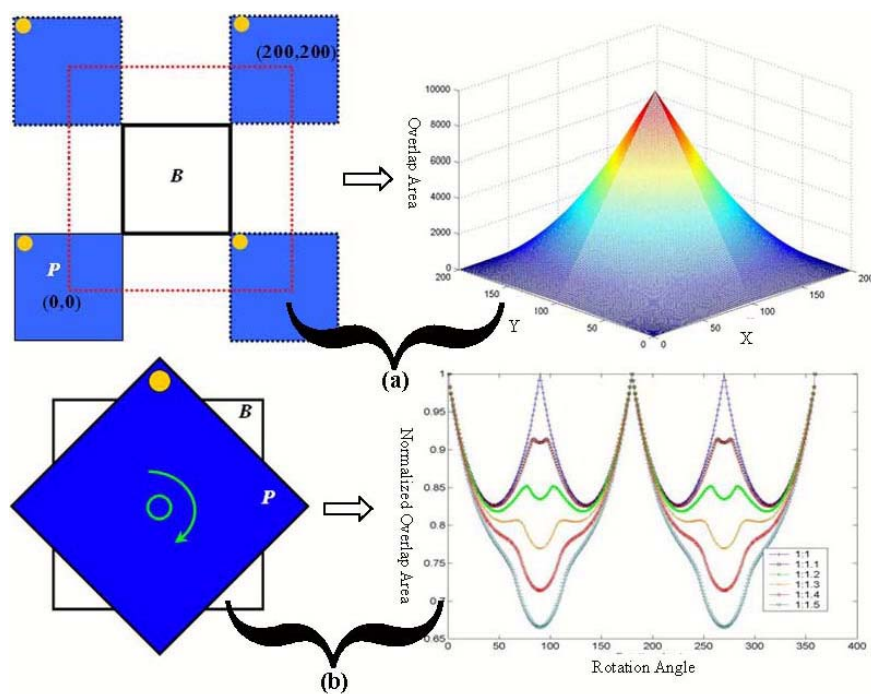


Figure 3.2: Visualization of overlap area between a moving part and a binding site: (a) translation of a square part (size:  $100 \times 100$  units); (b) rotation of a rectangular part with different aspect ratios. For parts that are nearly square, 4 overlap maxima exist. For more elongated rectangles (aspect ratio beyond 1:1.3) only 2 overlap maxima remain.

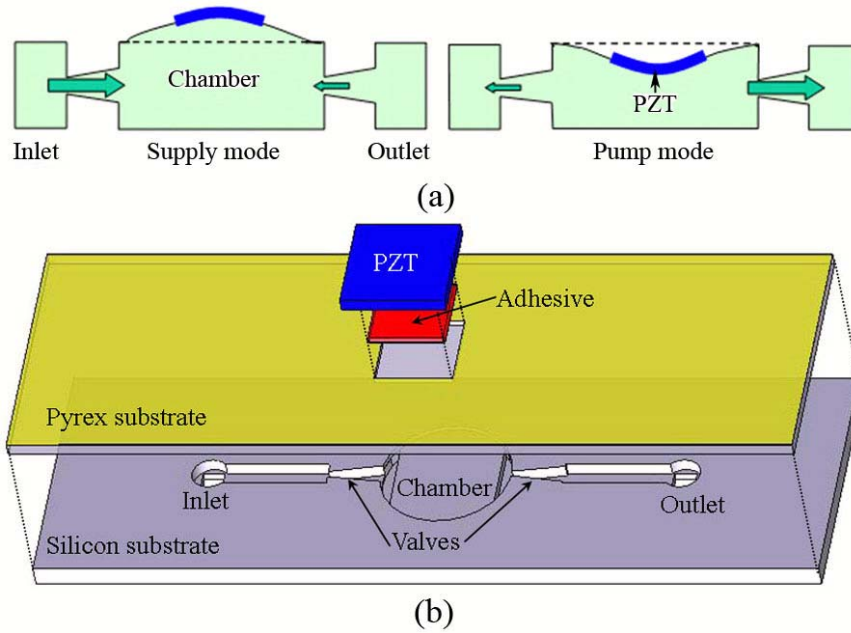


Figure 3.3: Schematic views of a diffuser valve micro pump: (a) supply and pump modes, net flow to the right; (b) an exploded view.

inlet/outlet holes, and the pump diaphragm is actuated by a unimorph structure - a single layer PZT bonded to the diaphragm: the PZT actuator expands and contracts in the diaphragm plane during a cycle of an AC driving voltage, which causes the diaphragm to bend upwards and downwards. A diffuser valve has lower resistance for flow from the narrow port to the wide port than the reverse flow. During a half AC cycle, the pump chamber volume increases, and more flow comes from the inlet valve; during the other half AC cycle, the pump chamber volume decreases, and more flow goes out through the outlet valve.

### 3.3.2 Fabrication

The silicon pump substrate was etched by two deep reactive ion etching (DRIE) processes. Photoresist AZ4620 was used as the mask for each DRIE process and



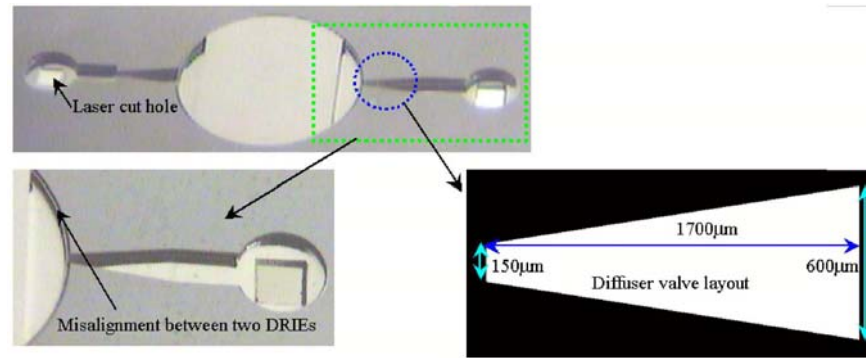


Figure 3.4: Microscope images of DRIEed silicon substrate and the diffuser valve layout.

patterned by photolithography with the following steps: (1) singe the substrate on a 110°C hotplate for 1 minute; (2) spincoat primer P10 and photoresist AZ4620 subsequently at the speed of 2200rpm for 30sec (AZ4620 thickness is about 8µm); (3) prebake AZ4620 on a 110°C hotplate for 3 minutes; (4) expose AZ4620 with a mask for 30sec to 10mW/cm<sup>2</sup> UV light; (5) develop AZ4620 in a solution of AZ400K : DI water = 1 : 4 for 2 minutes, then rinse the substrate in DI water and dry it with a N<sub>2</sub> gun; (6) hardbake AZ4620 on a 110°C hotplate for 15 minutes. The first DRIE was to etch pump chambers, which were 5mm in diameter and 24µm in depth. The large and shallow features of the chambers made spincoating of another layer of AZ4620 feasible, producing a sufficiently conformal coating of photoresist over this step feature. The second DRIE was used to etch diffuser valves and channels with a total depth of 275µm. After each DRIE was done, the photoresist was stripped with the following process: soak in 60°C EKC solution for 10 minutes and in 75°C AZ300T solution for 5 minutes, and then rinse in DI water and dry with a N<sub>2</sub> gun. A laser cutter (Model 4410, ESI, OR) was run in a raster mode to drill 0.8mm square inlet and outlet holes to the back side of the substrate (Figure 3.4).

A 500µm thick pyrex wafer was anodically bonded to the etched silicon substrate

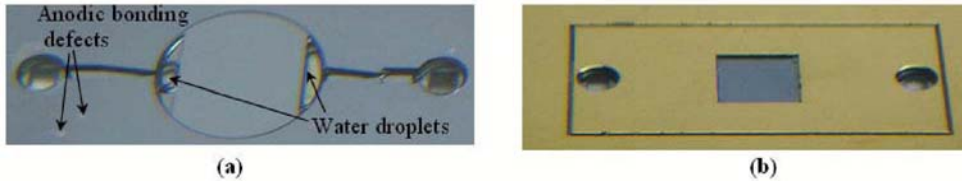


Figure 3.5: (a) An optical image of the anodically bonded pyrex/silicon stack (water droplets were intentionally introduced to the channels to indicate the pyrex capping); (b) an optical image of patterned Au covering the pyrex surface (the square receptor site at the center of the pump chamber was recessed by  $24\mu\text{m}$ , and two circular openings were used for later alignment with fluid interconnects on the pumping test stage, see Figure 3.13).

(Figure 3.5a). Before bonding, both the silicon substrate and the pyrex wafer were cleaned with the following process: the silicon substrate was dipped in buffered oxide etchant (BOE) for 1 minute to remove native oxide, and soaked in a Nano-strip solution (Rockwood Electronic Materials, CA, USA) for 15 minutes together with the pyrex wafer to strip organic residues, then both wafers were soaked in flowing DI water for about 5 minutes and dried in a spin dryer. After thorough cleaning both wafers were transferred to a  $250^\circ\text{C}$  hotplate and heated for about 2 minutes, and then immediately transferred to a  $500^\circ\text{C}$  hotplate to be baked for 5 minutes. Two-stage heating prevents wafers from cracking by a significant thermal stress due to sudden change of temperature. Then the pyrex wafer was placed on the silicon substrate and a DC voltage of 1200V was applied to the stack with the cathode electrode probe touching the pyrex surface, so that the pyrex wafer was permanently bonded to the silicon substrate.

To get a thinner pump diaphragm, HF (49%wt) was used to etch pyrex. A piece of dicing blue tape was attached to the back side of the pump substrate to cover inlet and outlet holes, which kept the pump cavities clean from the etchant. The pyrex wafer was thinned down to  $230\mu\text{m}$  in thickness within 45 minutes. Finally the substrate was cleaned in DI water and dried by a  $\text{N}_2$  gun, and the blue tape was

manually peeled off.

### **3.4 PZT Self-Assembly**

#### *3.4.1 Hydrophilic Recessed Binding Sites*

The binding sites for self-alignment of the PZT actuators were designed as recessed hydrophilic wells in a hydrophobic surface (Figure 3.5b). These shallow wells contained the adhesive liquid that drove the assembly, and were slightly smaller than the PZT actuators, such that the well rims can make electrical contacts with the PZT actuators. A layer of Cr/Au (50/1000Å) was deposited on the pyrex surface of the bonded pump substrate and patterned by an etching process. The etching mask was photoresist AZ1512 patterned by photolithography to expose the 3mm square binding sites directly above the centers of the pump chambers. After Cr/Au etching, pyrex in the binding sites was etched by HF (49%wt) until 24μm deep wells were formed, and the etching rate was about 6.75μm/min.

#### *3.4.2 Fabrication of PZT Parts*

PZT actuators were fabricated from a piece of 2.85"×2.85"×0.0075" PZT sheet (T107-H4E-602, Piezo Systems, Cambridge, MA) which was coated with ~3000Å thick nickel on both sides. Following are the fabrication steps: (1) AZ1512 was spincoated and UV exposed with a mask protecting 3mm square areas used for later bonding (space between two squares was 1mm), after developing only the square bonding areas were coated with AZ1512; (2) Cr/Au (50/1000Å) was deposited on both sides of the PZT sheet by two thermal evaporations; (3) the PZT sheet was rinsed in acetone to strip AZ1512 along with Cr/Au on it, then the square bonding areas were exposed (Figure 3.6a); (4) the PZT sheet was diced by a laser cutter into 4mm square parts with the 3mm square bonding area at the center; (5) the diced parts were cleaned with acetone, IPA and DI water in sequence inside a sonicator. Finally the cleaned

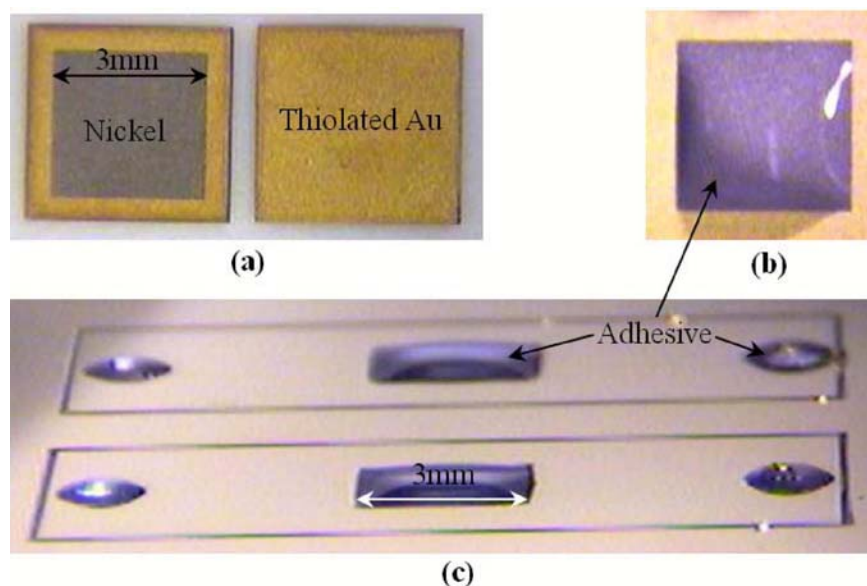


Figure 3.6: Wetting property of PZT parts and the pump substrate: (a) top and bottom views of a PZT part; (b) adhesive liquid wets only the nickel bonding area on the PZT part; (c) adhesive wets the recessed pyrex binding sites on the pump substrate.

parts were collected to a piece of filter paper and dried by baking on a 100°C hotplate for 5 minutes.

### 3.4.3 Surface Treatment for the Pump Substrate and PZT Parts

The pump substrate and the PZT parts were soaked overnight in a 1mmol alkanethiol solution (diluted in ethanol) for gold surfaces to adsorb a self-assembled monolayer (SAM). Contact angles of water and the adhesive liquid on the treated surfaces were respectively measured by a FTA200 goniometer (First Ten Angstroms, Inc.), and the results in (Table 3.1) indicate that the thiolated Au surfaces on either pyrex or PZT substrates have much less attraction for both water and the adhesive liquid than pyrex and nickel surfaces. Flushing of the adhesive liquid across the pump substrate or the bonding face of a PZT part left droplets only on the pyrex binding sites or nickel

Table 3.1: Contact angles of water and the adhesive liquid on different surfaces

	Pyrex	Thiolated Au on Pyrex	PZT	Thiolated Au on PZT
Water	32°	108°	40°	102°
Adhesive liquid	4°	51°	0° <sup>a</sup>	40°

<sup>a</sup>0° indicates super high wettability, i.e., a droplet spreads quickly into a thin film on a substrate.

bonding areas on the PZT parts (Figure 3.6b-c).

#### 3.4.4 Orbital Shaking Assisted Self-Assembly

This self-assembly technique exploits surface tension force to self-align PZT parts to the photolithography-defined 3mm×3mm×24μm hydrophilic recessed binding sites. In an air environment the acrylate-based adhesive only wets the hydrophilic areas of the recessed binding sites and nickel areas on the PZT parts (Figure 3.6). Dry PZT parts were introduced manually without alignment onto the adhesive droplets on the binding sites with the exposed nickel surface facing down. According to the capillary-driven self-assembly mechanism described in Section 3.2, the minimum interfacial energy state can be achieved when the PZT part is aligned with the recessed binding site. But because the 4mm square PZT part is larger than the 3mm square binding site, the unaligned PZT parts tended to tilt and touched the substrate with their corners or edges, which caused significant friction, preventing surface tension from aligning the parts. As a remedy, an orbital shaker (Model 51300-00, Cole-Parmer Instrument Company) was used to provide centrifugal forces to the PZT parts. The centrifugal forces dragged and balanced the parts on the adhesive droplets temporarily so that surface tension can drive self-alignment of these PZT parts (Figure 3.7). To assist self-assembly, orbital shaking introduced centrifugal force  $m\omega^2 R_s$  should be less

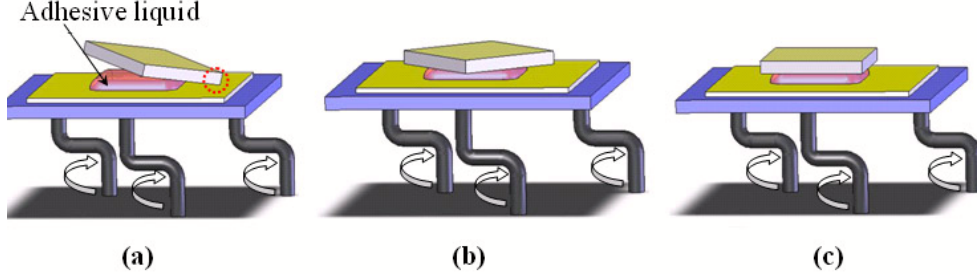


Figure 3.7: Schematic diagrams for orbital shaking assisted self-assembly: (a) a part sticks to the substrate by its right corner; (b) a temporarily left-directed centrifugal force from the orbital shaking releases and balances the tilted part; (c) the balanced part immediately self-aligns to the binding site, and keeps its alignment at the minimum interfacial energy state when the centrifugal force changes direction.

than the surface tension  $F_{st}$  on the part by the adhesive, therefore the shaking speed  $\omega$  should stay below an upper limit  $\omega_{max}$

$$\omega_{max} = \sqrt{\frac{F_{st}}{mR_s}} = \sqrt{\frac{F_{st}}{\rho s^2 t R_s}} \quad (3.4)$$

Where  $R_s$  is the rotating arm length of the orbital shaker,  $m$  is the mass of the part. The mass of a square part  $m$  is equal to  $\rho s^2 t$ , where  $\rho/s/t$  are density/side length/thickness, respectively. For the 4mm square PZT part,  $\rho=7.8\text{g/cm}^3$ ,  $s=4\text{mm}$ ,  $t=190\mu\text{m}$ .

We observed that alignment between PZT actuators and binding sites took place within 1sec, i.e., immediately after the orbital shaker ( $R_s=1.27\text{cm}$ ) was turned on and ramped up from 0rpm to 200rpm (the shaking speed we set), so that  $F_{st}$  in Equation (3.4) should be the surface tension on the PZT part when the part starts to leave the aligned state. According to reference [GLK<sup>+</sup>02], the maximum surface tension or restoring force by the acrylate-based adhesive on a 1mm square part leaving the aligned state is about  $0.9 \times 10^{-4}\text{N}$ . Due to the linear relation between surface tension and part side length, the maximum surface tension on the PZT part having 3mm square hydrophilic bonding area is  $F_{st} = 3 \times 0.9 \times 10^{-4}\text{N} = 2.7 \times 10^{-4}\text{N}$ . By plug-

ging the values of  $\rho/s/t/R_s/F_{st}$  into Equation (3.4), we get the shaking speed limit  $\omega_{max}=286\text{rpm}$ , which is close to the experimental result 300rpm, when the PZT part left the binding site.

#### 3.4.5 *Electrical Connections by a Pressing Plate Method*

A pressing plate (Figure 3.8) method was utilized to establish electrical connections between the PZT parts and the pump substrate (Figure 3.9). The non-conductive adhesive can only provide mechanical bonding at the center of a PZT part. Because the PZT part is larger than the binding site and has an Au rim on the bonding face, electrical connections can be established through the Au rim. We applied a glass plate on the aligned PZT parts to squeezed out excess adhesive with a pressure of about  $2 \times 10^4 \text{N/m}^2$ , such that the Au rims touched the substrate (Figure 3.10a). The PZT part has a surface with about  $1\mu\text{m}$  roughness, which guarantees electrical connection even though the Au rim is coated with a thiol monolayer, and some adhesive residue may be trapped underneath it. Finally the electromechanical bonding was made permanent by polymerizing the adhesive on an  $85^\circ\text{C}$  hotplate for half an hour. The top electrodes of the PZT parts and the substrate were connected by wire bonding (Figure 3.10b). Our later experimental tests showed that all the 28 PZT actuators assembled on the 4" pump substrate were electrically connected, which indicates a 100% yield for the pressing plate method.

#### 3.4.6 *Adhesion Test*

A de-bonding test was performed in order to evaluate the bonding strength which is a key factor for PZT actuators. An experimental setup for the de-bonding test is schematically shown in Figure 3.11: the bonded stack of substrate, cured adhesive and PZT actuator was held vertically with the edge of the PZT resting on a pushing tip attached to a digital scale. The digital scale reading for the total mass of all the items was zeroed out, and then a pressing force applied to the top of the bonded

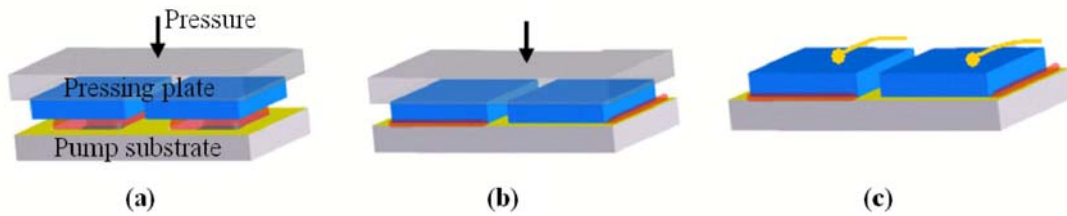


Figure 3.8: Schematic overview of a pressing plate method to establish electrical connections at the rims of PZT parts: (a) a glass plate is introduced to press the aligned PZT parts; (b) excess adhesive is squeezed out of the wells and the rims of PZT parts contact the substrate; (c) adhesive is polymerized, the pressing plate is removed and the top electrical connections are made with solder bonding.

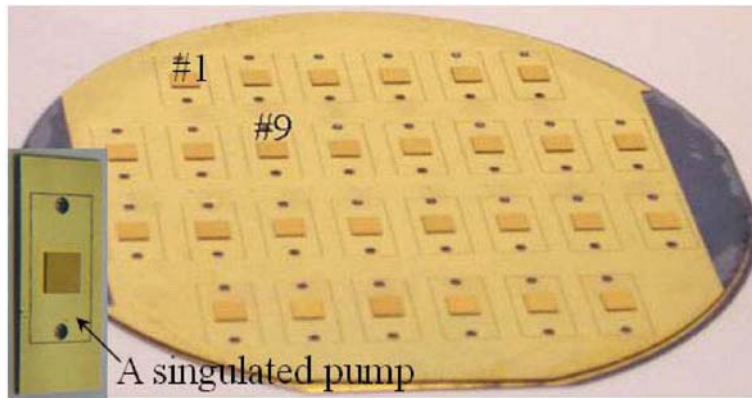


Figure 3.9: Optical images of twenty-eight PZT actuators self-assembled on a 4'' pump substrate and a singulated micro pump.

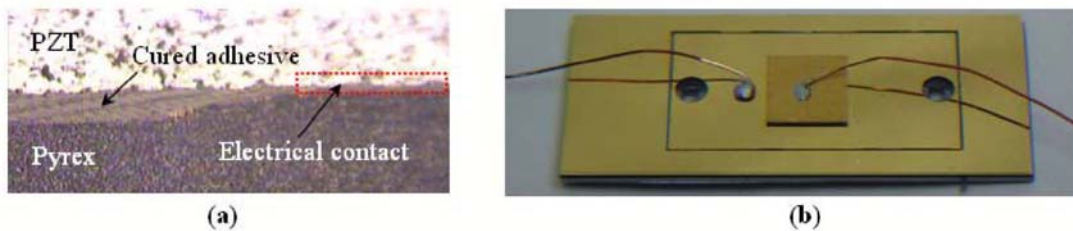


Figure 3.10: Optical images showing the electrical connections to a PZT actuator: (a) a cross-section microscope image taken after a through cut of an assembled pump across the recessed pyrex binding site; (b) two thin electrical wires respectively solder bonded to the PZT top surface and the pump substrate, thus a driving voltage can be applied to activate the PZT actuator through these two leads.



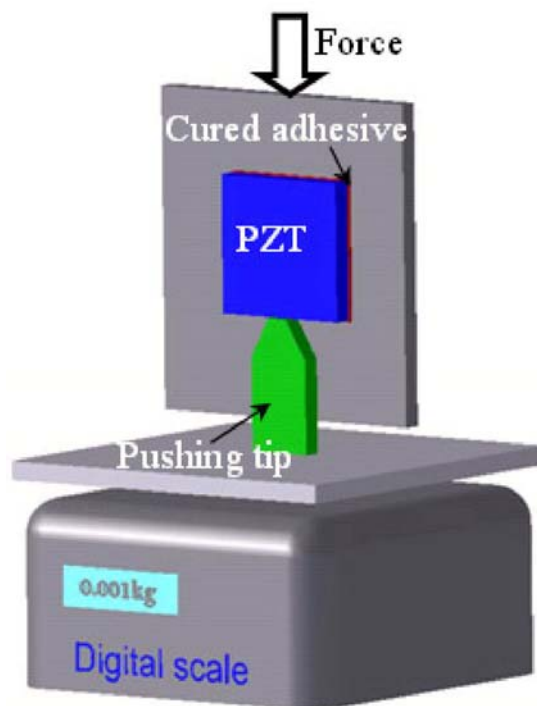


Figure 3.11: Schematic experimental setup for de-bonding tests. A PZT actuator bonded to a substrate is pushed against a tip attached to a digital scale, and the applied force is increased and recorded until failure.

stack was increased until the PZT part was de-bonded, so the final reading in unit of kilograms multiplied by  $g=9.81\text{N/kg}$  was the de-bonding force.

Hydrophilicity of binding sites, determined by interfacial energies, affects the bonding strength of PZT actuators. The binding sites for the above in-air assembly process were hydrophilic, while the binding sites were hydrophobic thiolated gold for our previously reported in-water assembly process [XHF<sup>+</sup>03]. In order to compare the bonding strength of these two assembly processes, we assembled eight 3mm square PZTs (same bonding area as that in the above in-air assembly process) in a single batch with the same curable adhesive using the in-water assembly process. These eight PZT actuators were respectively de-bonded by forces of 8N, 5N, 7N, 5N, 9N,

Table 3.2: Ethanol pumping results of the eight pumps

Pump No.	1	2	3	4	5	6	7	8
Res. Freq. (kHz) <sup>a</sup>	7.0	7.0	6.8	6.9	7.0	7.0	7.1	7.1
Flow Rate ( $\mu\text{l}/\text{sec}$ ) <sup>b</sup>	0.387	0.408	0.365	0.385	0.365	0.390	0.385	0.386

<sup>a</sup>Fundamental resonant frequency

<sup>b</sup>Flow rate at the resonant frequency, and the driving voltage is  $90V_{\text{p-p}}$ .

7N, 4N and 6N. All the de-bonding processes took place at the interfaces between the cured adhesive and hydrophobic thiolated gold binding sites, which indicates the alkanethiol monolayer weakened the bonding. Five out of 28 PZT actuators assembled in air were randomly chosen for the de-bonding test, and none of them were de-bonded at the force of  $\sim 20\text{N}$ , but the PZT edges contacting the pushing tip were broken.

### 3.5 Pumping Tests

#### 3.5.1 Resonant Frequencies

To demonstrate performance uniformity of all the 28 pumps assembled simultaneously on the 4-inch substrate (Figure 3.9), we used a laser vibrometer to measure their resonant frequencies without any fluid load. The frequency of the driving sinusoidal voltage signal was changed continuously from 1kHz to 150kHz, and the maximum output of the laser vibrometer indicated a resonant frequency. The average of all the 28 fundamental resonant frequencies is 80.1kHz, and the standard deviation is 2.0kHz (Figure 3.12). The following factors may contribute to this 2.5% relative deviation: (1) PZT actuator tolerances of  $\pm 50\mu\text{m}$  in length and width; (2) residual stress variance among the pump chamber diaphragms introduced by the anodic bonding process;

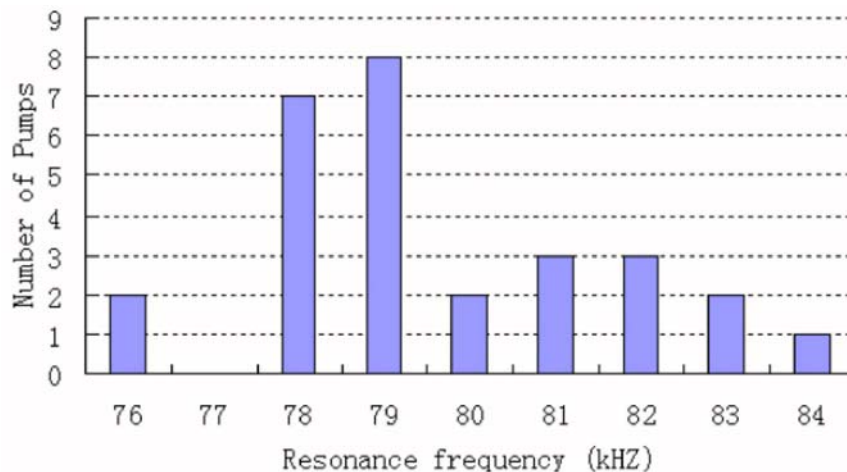


Figure 3.12: Distribution of resonant frequencies for all the 28 pumps on a 4" substrate.

(3) dimension variance among pump cavities in the silicon substrate due to non-uniformity of the DRIE processes (standard deviations of chamber depth and channel depth are respectively  $0.55\mu\text{m}$  and  $1.15\mu\text{m}$ ).

### 3.5.2 Pumping Rates

Eight pumps were chosen for pumping tests with ethanol on a reusable testing stage (Figure 3.13). Each pump substrate was mounted onto the testing stage with silicon rubber rings. During the pumping tests, the inlet and outlet Teflon tubes (both tubes were about 15cm long) were taped to a level workstation, and time was counted for the ethanol front end to move through a chosen 1cm long region in the outlet tube. Because fluidic resistance of a tube increases with its length [MF03], the ethanol front end has a decreased speed as it moves towards the outlet tube end if the driving signal on the PZT actuator is kept constant. To keep consistency between different driving frequencies, the ethanol front end was reset to the same initial position before applying a new driving frequency. The pumping results shown in Table 3.2 indicate:

(1) the average and standard deviation of the fundamental resonant frequencies of the eight pumps are 6.99kHz and 0.10kHz, respectively; (2) when the driving voltages are  $90V_{p-p}$ , the average and standard deviation of the pumping rates at resonant frequencies are respectively  $0.384\mu\text{l}/\text{sec}$  and  $0.014\mu\text{l}/\text{sec}$ .

### **3.6 Conclusions and Discussions**

We have demonstrated a capillary-driven self-assembly technique by assembling PZT actuators for 28 diffuser valve micro pumps on a 4" substrate. All the 28 pumps worked with high uniformity, which is indicated by small standard deviations of their resonant frequencies. This assembly technique has several major advantages over the conventional bonding method, manual bonding with highly viscous silver epoxy, for PZT actuators: precise placement by capillary-driven self-alignment [SHR<sup>+</sup>02], tilt free and strong bonding, well-controlled adhesive thickness, electrical and mechanical connections established respectively at the rim and center of the assembled part, low process temperature.

Performance uniformity among the micro pumps constructed in the same or different batches depends on both the fabrication steps for the pump substrates and the final assembly processes for PZT actuators. DRIE processes brought about various depths of the pump cavities even on the same substrate, and the anodic bonding process introduced different residual stresses on each pump diaphragm. The uniformity of DRIE processes relies on the improvement of the DRIE equipment and optimized process parameters. Low stress wafer bonding processes, e.g. low temperature anodic bonding [WXN<sup>+</sup>03], can improve the residual stress problem. Repeatability of the assembly process for PZT actuators relies on two major factors: recessed binding sites and placement of the PZT actuators. Recessed pyrex binding sites were formed by HF etching and the etching rate depended on the HF concentration. Provided good control of the HF concentration, the etching rate can be accurately

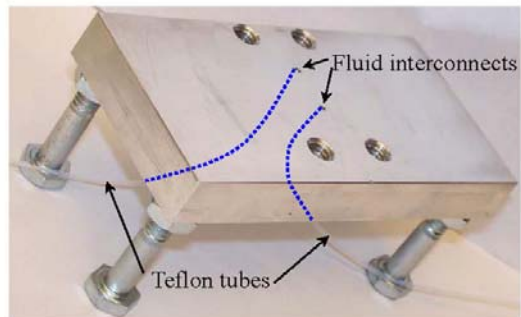
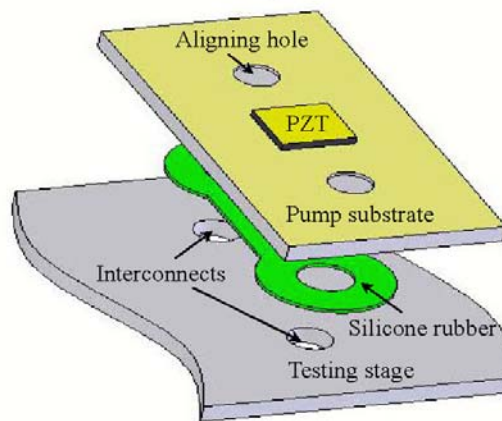
**(a)****(b)**

Figure 3.13: A reusable testing stage: (a) an optical photograph of the stage before mounting a pump substrate; (b) a schematic exploded view of mounting a pump substrate with silicone rubber, which can be de-bonded without any residue by an appropriate shear force.

controlled [KBNG97, KCBG99], and so can the recessed depth for the binding sites. Accurate placement of the PZT actuators was achieved by the self-alignment process driven by surface tension forces, which has been shown to be highly repeatable.

This self-assembly process can also be applied to other types of electromechanical microchips. Especially for microchips with materials or structures sensitive to aqueous assembly environments, this dry assembly method shows a significant advantage over other wet assembly techniques. With batch process capabilities, this self-assembly technique supports construction of more versatile and miniaturized microsystems.

## Chapter 4

**UNIQUELY ORIENTING SELF-ASSEMBLY  
(DUO-SPASS PROCESSES)****4.1 Introduction**

Micro-assembly is required in both packaging of micro-device chips and integration of complex hybrid microsystems. Current micro-assembly technologies can be categorized as: micromanipulator based assembly [CBN<sup>+</sup>98, RVN00, SF98, TF01, WS00, YGN01, EVK01], wafer-to-wafer devices transfer [CLHP96, HS98, PKPL04, SHC<sup>+</sup>99], fluidic shape-directed self-assembly [YS94, ZBJ04], and capillary-driven self-assembly [JTS<sup>+</sup>02, SLH01, FWB04]. Each of these assembly techniques has its limitations: micromanipulator based assembly processes are serial and slow, and micro-parts tend to stick to micromanipulators because adhesive forces dominate gravitational forces; wafer-to-wafer pattern transfer is limited to microstructures fabricated on the same substrate; most types of microchips have rectangular shapes due to mechanical dicing along straight lines, but neither fluidic shape-directed self-assembly nor capillary-driven self-assembly can align them to unique in-plane orientations, which is required, for example, for a microchip with multiple interconnect pads so that correct electrical connections can be achieved via flip-chip bonding [Mil69, Goo69] to a carrier substrate.

Many methods to orient flat parts have been developed for part feeders of robotic assembly systems. Vibratory bowl methods [BPM82] pick parts with desired orientations via track filters. Programmable squeezing fields [BDM99] uniquely orient some types of flat polygonal parts. Neither of these two methods can uniquely orient parts

with rotationally symmetrical shapes. Usually visual feedback systems are used for flexible part feeders (“flexible” means that multiple types of parts can be handled by a single feeder) to present parts with correct orientations [SS99]. But all these part feeding methods are serial processes and not suitable to handle very large numbers of parts, e.g. for mass packaging of radio frequency identification (RFID) chips.

Uniquely orienting assembly is the key requirement to package micro-device chips having multiple interconnect pads. This chapter demonstrates two different processes satisfying this requirement: a semi dry process based on gravity driven self-alignment and a dry process based on two-stage shape recognition between complementary features on parts and receptor sites.

## ***4.2 Wafer Level Packaging Strategy***

Usually bulk micro-device chips having multiple interconnect pads on one face (“bonding face”) are stored in a container with random face orientations. To package these chips at the wafer level, we propose the following process steps (Figure 4.1): (1) bulk parts are oriented to face the same direction with their bonding faces and spread in a single layer; (2) parts are palletized onto an alignment template (AT) with the face orientation preserved; (3) parts are distributed and anchored to receptor sites in a one-to-one mode; (4) parts are uniquely aligned on the receptor sites; (5) aligned parts are transferred to a chip carrier template (CCT) via wafer level flip-chip bonding. This packaging strategy except step 5, a well-established process in the IC industry, is demonstrated in each of the following two types of self-organizing parallel assembly processes (SPASS): the semi dry uniquely orienting process (semi-DUO-SPASS) and the dry uniquely orienting process (DUO-SPASS).



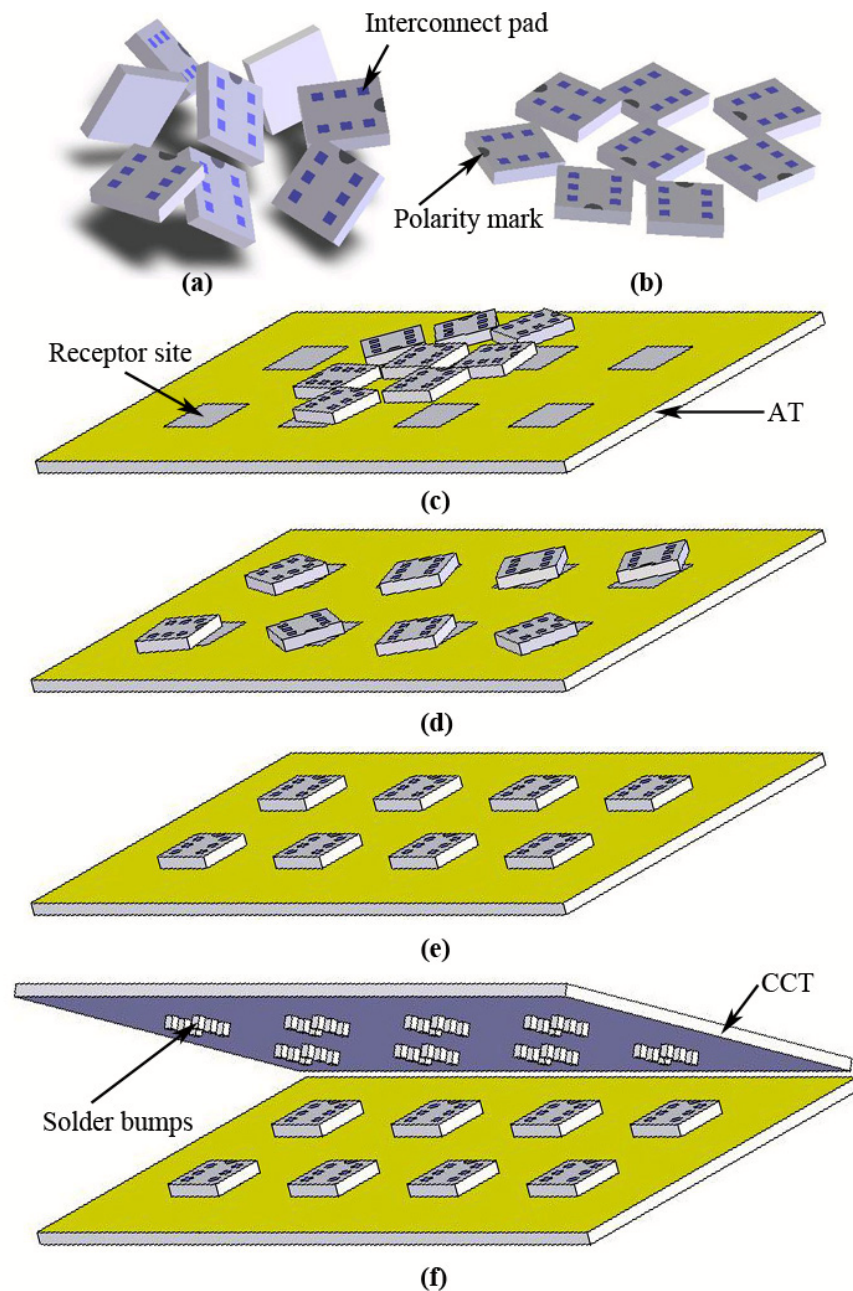


Figure 4.1: Wafer level packaging strategy: (a) randomly oriented bulk parts; (b) bulk parts are uniquely face-oriented and spread in a single layer; (c) parts palletized onto an alignment template (AT); (d) parts are distributed one-to-one to receptor sites; (e) parts are aligned to the receptor sites with unique in-plane orientations; (f) parts are bonded to a chip carrier template (CCT) via wafer level flip-chip bonding.

### 4.3 The Semi Dry Assembly Process (SEMI-DUO-SPASS)

This process consisted of 2 wet steps and 2 dry steps: bulk parts having only one hydrophobic face (used as a bonding face) were uniquely oriented with their hydrophobic faces upwards on an agitated water surface, and stayed together in a single layer; a hydrophobic substrate picked up the floating parts and transferred them onto an alignment template; orbital shaking moved the parts randomly across the alignment template until they were anchored to the receptor sites; anchored parts roughly self-aligned to the receptor sites on an appropriately tilted alignment template to minimize their potential energies. The accuracy of the coarse alignment was greatly improved by capillary-driven self-alignment when an appropriate amount of steam condensate was introduced onto the parts.

#### 4.3.1 Design Rule for Features on Parts and Receptor Sites

The semi dry assembly process is based on the peg-in-hole mechanism: the part has a circular peg (CP) offset from the center of mass, and the receptor site has a circular trench (CT) with a greater diameter than the circular peg. The larger trench is used for faster trapping of the peg, i.e., anchoring of a part. For one-to-one registration of parts, the trench diameter must stay below an upper limit  $\bar{\mathcal{O}}_{CT}$  which is determined by:

$$\bar{\mathcal{O}}_{CT} = \bar{\mathcal{O}}_{CP} + 2d \quad (4.1)$$

where  $\bar{\mathcal{O}}_{CP}$  is the diameter of the peg, and  $d$  is the smallest distance from the peg center to the part edge (Figure 4.2). If this condition is satisfied, no more than one peg can be trapped simultaneously in one trench.

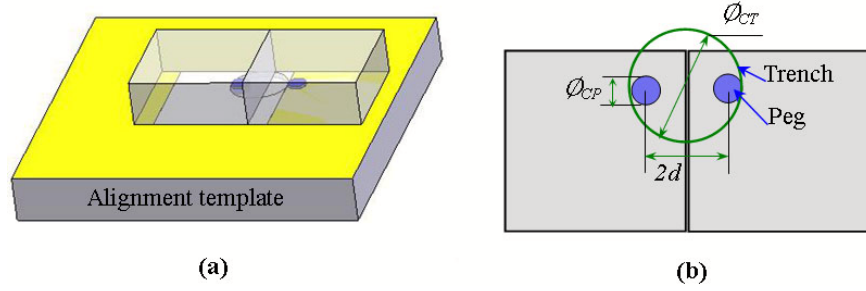


Figure 4.2: One-to-one registration design rule: (a) two parts competing for one receptor site; (b) top view of the parts and receptor site.

#### 4.3.2 Fabrication of Parts and Alignment Template

##### *Parts*

Square diced silicon parts (side length = 2mm) were used to demonstrate the semi dry assembly process. We fabricated the parts from a 4-inch single side polished (SSP) silicon wafer with the following steps: (1) spincoat photoresist AZ4620 on the polished side and lithographically pattern AZ4620 to cover only circular peg areas ( $\text{\O}0.3\text{mm}$ ); (2) deep reactive ion etch (DRIE) the polished side for about 20 minutes to form the protruding pegs with  $45\mu\text{m}$  height; (3) spincoat photoresist AZ1512 on the rough side and lithographically pattern AZ1512 using double side alignment (ABM IR aligner) to cover the circular areas directly opposite to the pegs; (4) sputter deposit a layer of TiW/Au ( $50/800\text{\AA}$ ) on the rough side; (5) strip all the photoresist together with TiW/Au on it in acetone, then rinse the wafer in IPA and DI water, and dry it with a  $\text{N}_2$  gun. Finally the silicon wafer was mechanically diced into 2mm square parts (Figure 4.3a). The opening in the gold layer marks the position of the peg on the other side, as well as the part polarity.

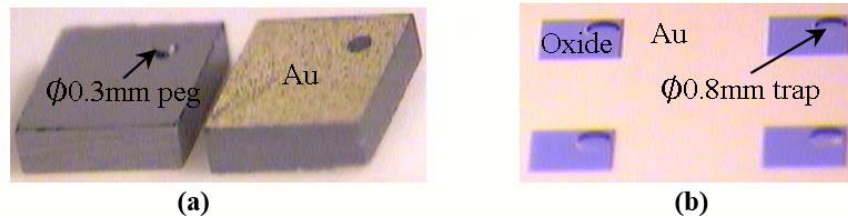


Figure 4.3: Microscope images of parts and receptor sites: (a) top and bottom views of 2mm square silicon parts; (b) a  $2 \times 2$  section of an array of 2mm square receptor sites on a 4-inch alignment template.

### *Alignment Template*

An alignment template with an array of 168 receptor sites was fabricated from a 4-inch oxidized SSP silicon wafer (thermal oxide thickness is about  $3900\text{\AA}$ ) with a DRIE process and a lift-off process. Patterning of the receptor sites on the polished wafer surface was accomplished with the following steps: (1) spincoat AZ4620 and lithographically pattern it to expose only the circular trench areas ( $\text{\AA}0.8\text{mm}$ ), then completely remove the exposed oxide in a buffered oxide etchant (BOE) with an etching rate of about  $600\text{\AA}/\text{min}$ ; (2) DRIE the wafer for 20 minutes to form  $60\mu\text{m}$  deep trenches (this etching rate is greater than that for the pegs because of the loading effect [BBA98] in the DRIE process), and then strip AZ4620; (3) spincoat AZ1512 and pattern it to cover only square receptor site areas and sputter deposit  $50/800\text{\AA}$  TiW/Au; (4) strip AZ1512 and lift off metal in acetone. An array of receptor sites is shown in Figure 4.3(b).

### *Surface Treatment*

Surface treatment was applied to the silicon parts and the alignment template to prepare them for the assembly process. First, the parts and the template were soaked in a Nano-strip solution (Rockwood Electronic Materials, CA, USA) for half an hour, and then rinsed with DI water. The Nano-strip solution oxidized the silicon surfaces

and removed photoresist residues from the gold surfaces. Second, the parts and the template were soaked in a 1mmol alkanethiol  $\text{CH}_3(\text{CH}_2)_{11}\text{SH}$  (in ethanol) solution overnight. The gold surfaces became hydrophobic after adsorbing a self-assembled monolayer (SAM) from the alkanethiol solution. Then each silicon part had only one hydrophobic thiolated gold face, and all the other faces were hydrophilic silicon oxide. The receptor site area was hydrophilic silicon oxide, and its background was a hydrophobic thiolated gold surface. Finally, the parts and the alignment template were dried respectively with heating on a 120°C hotplate and blowing  $\text{N}_2$ .

### 4.3.3 *Uniquely Face-orienting Bulk Parts*

#### *Orbital Shaken Water Surface*

Water in a stationary glass beaker has a horizontal plane surface when neglecting the slight bending near the hydrophilic beaker sidewall. When the beaker is attached onto a running orbital shaker, the water surface becomes a tilted plane (Figure 4.4a). The slope of the tilted plane is determined by the shaking speed, which can be calculated by the following approximate physical model.

Considering a finite element at the tilted water surface, it has three forces (Figure 4.4b): gravity (downwards), centrifugal force (horizontal) and supporting force by the nearby water (normal to water surface). The vector sum of these forces goes to zero at a steady state, which indicates that the slope  $s$  of the water surface is determined by:

$$s = \frac{\omega^2 R_s}{g} \quad (4.2)$$

where  $\omega$  is the shaking speed,  $R_s$  is the shaker arm length, and  $g$  is the gravitational constant.

When neglecting the dragging force from the beaker sidewall, the orbital shaken water surface is still a plane, because both the centrifugal force and gravity are uniform across the water surface, and so is the slope  $s$ . The water surface plane is always

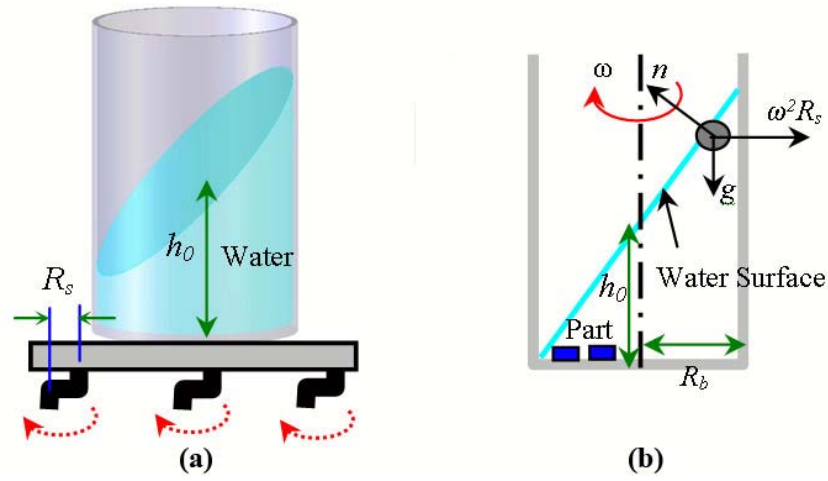


Figure 4.4: Schematic view of orbitally shaken water surface: (a) tilted water surface plane; (b) cross section view perpendicular to the tilted water surface.

perpendicular to the vector sum of gravity and centrifugal force.

### *The Face-orienting Process*

Initially bulk parts were randomly oriented, and we invented the following new agitating process to orient all the parts to face the same direction with their pegs before palletizing. The 2mm square silicon parts can float on a water surface because surface tension is sufficient to balance their gravitational forces. For a smaller part with side length  $L$  and thickness  $t$ , surface tension ( $\propto L$ ) is even more significant compared with the gravitational force ( $\propto L^2 \times t$ ). We put the 2mm square silicon parts in a beaker and submerged them with water, and then shook the beaker on an orbital shaker (Model 513500, Cole-Parmer) to tilt the water surface above a speed of  $\omega_c$  so that some parts were exposed to air. According to Equation (4.2) and Figure 4.4(b), we can calculate this critical shaking speed:

$$\omega_c = \sqrt{\frac{h_0 g}{R_b R_s}} \quad (4.3)$$

where  $h_0$  is the still water level and  $R_b$  is the radius of the beaker bottom. In our experiment, these parameters were:  $h_0 = 12\text{mm}$ ,  $R_s = 12.7\text{mm}$ ,  $R_b = 12\text{mm}$ . The theoretical and experimental values of  $\omega_c$  were respectively 268rpm and 310rpm, and the difference came from the assumption of neglecting friction from the beaker sidewall for the above approximate physical model. Water surface tension dragged and floated the exposed parts. After 1 minute shaking, most of the submerged parts floated, and all floating parts had their hydrophobic thiolated gold faces upwards (the only stable state on an agitated water surface) and stayed together in a single layer to minimize potential and interfacial energies.

#### 4.3.4 Palletizing Floating Parts

##### *Carrier Wafer*

A carrier wafer (CW) was used to pick up the floating parts and palletize them onto an alignment template. The carrier wafer was a 3-inch pyrex wafer coated with hydrophobic fluorocarbon polymer PFC802 (Cytonix Corp., MD, USA) on one side. When the carrier wafer was inserted into the water vertically, the water surface bent downwards near the hydrophobic PFC802 surface and bent upwards near the hydrophilic pyrex surface (Figure 4.5). The contact angle of water on a PFC802 surface is  $\theta_c = 110^\circ$ . The intersection angle  $\alpha$  (Figure 4.6a) between the carrier wafer and the water surface should be greater than  $180^\circ - \theta_c = 70^\circ$  so that the water surface bends downwards near the PFC802 surface, and the water valley near the PFC802 surface attracts nearby floating parts by minimizing their potential energies. If  $\alpha$  is less than  $70^\circ$ , then the water surface bends upwards near the PFC802 surface and the carrier wafer repels nearby floating parts.

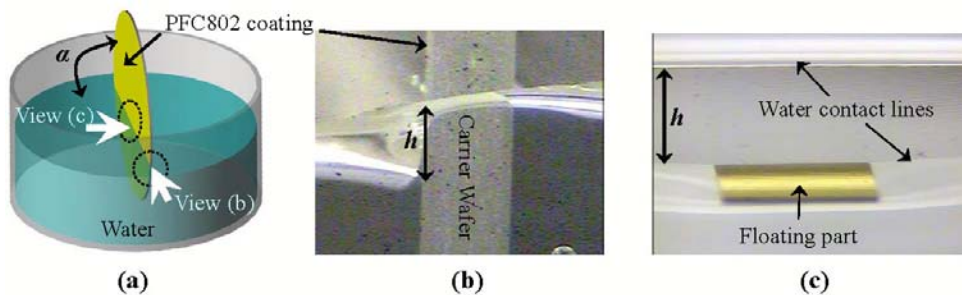


Figure 4.5: Water surface bending near carrier wafer (CW) surfaces: (a) schematic view of a carrier wafer inserted vertically in water; (b) side view of water surface bending near both sides of the carrier wafer; (c) front view of water surface bending near carrier wafer surfaces, and a floating part trapped in the water valley close to the hydrophobic PFC802 surface (the variations in the top surface color of the part is due to lighting effects, in reality, the top surface is uniformly covered with gold except a small mark hole).

### *The Palletizing Process*

When the carrier wafer continuously entered the water vertically ( $\alpha > 70^\circ$ ), the parts adhered to the carrier wafer firmly (Figure 4.6a) due to significant capillary forces caused by trapped air bubbles underneath them (Figure 4.7). After all the floating parts stuck to the carrier wafer, it was withdrawn completely from water, and more than 98% of the parts kept sticking to it due to capillarity of the residual water on the hydrophilic part surfaces. Finally the carrier wafer was brought approximately parallel to the alignment template (Figure 4.6b) on a  $120^\circ\text{C}$  hotplate, and the parts were released to touch the template with their pegs when water evaporated. The carrier wafer was brought very close to the alignment template to preserve the face orientations of all the parts during the releasing.

### *Trapping Parts*

We utilized orbital shaking to move the parts across the surface of the alignment template. This template was attached to an orbital shaker platform, and a Petri



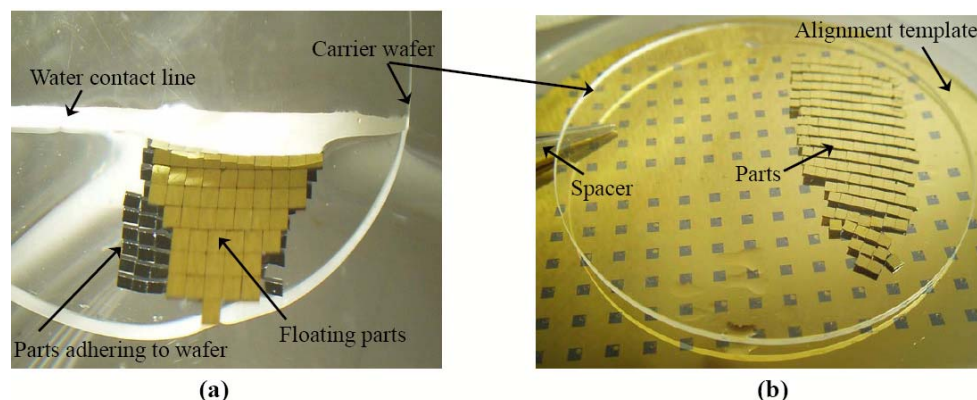


Figure 4.6: The palletizing process: (a) a carrier wafer inserted into water, and floating parts adhere to the hydrophobic PFC802 surface firmly; (b) the carrier wafer brought approximately parallel to an alignment template to release the adhering parts when water evaporates.

dish which was flipped over the template defined the moving range for all the parts. Orbital shaking can produce centrifugal forces which are evenly distributed across the shaker platform. The centrifugal forces are proportional to the square of the shaking speed and should be large enough to overcome sliding friction for the parts to move around. The 2mm square silicon parts started to move at a shaking speed of about 150rpm, which indicated that the sliding friction coefficient ( $= \omega^2 R_s / g$ ) of the alignment template was about 0.3. According to reference [Jia02], a thiolated gold surface has a friction coefficient of about 0.04 - 0.12, which was measured by atomic force microscope (AFM) tips. The friction coefficient in our experiment was greater because of several factors such as moisture or other contaminants adsorbed from the environment at the interface between the parts and the alignment template.

The moving parts were anchored by the trenches of the receptor sites. The four corner receptor sites are blocked by the Petri dish, and the remaining 164 receptor sites are open to receive parts. We performed four trapping experiments without and with 10%, 20%, 30% redundant parts (Figure 4.8). During the first 10sec, the

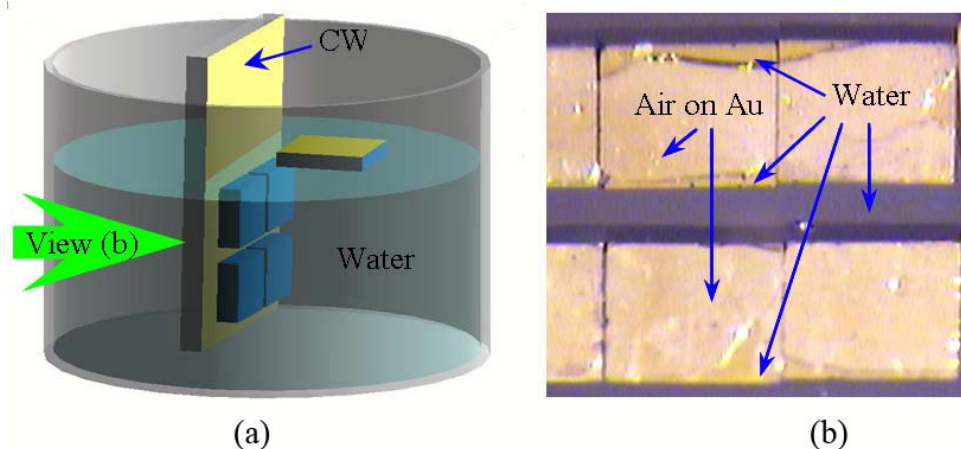


Figure 4.7: Mechanism of parts adhering to the hydrophobic surface: (a) a schematic view of a carrier wafer inserted vertically into water to pick up floating parts; (b) a microscope image of trapped air bubbles underneath the parts adhering to the carrier wafer in water.

shaking speed was 200rpm, and the trapping yield (number of occupied receptor sites / 164) reached about 80% for all 4 cases. A slow shaking speed for the first 10sec can avoid parts flipping due to violent collisions among the crowded parts. After that, the shaking speed was raised to 250rpm. With most of the parts anchored to the uniformly distributed receptor sites, a higher shaking speed can cause the remaining free parts to move faster to get trapped, and no part flipping was observed for all the 4 cases. After 3 minutes shaking, 95% to 99% of the receptor sites were occupied, with higher part redundancies producing higher yields.

#### 4.3.5 Uniquely Aligning Parts

##### *Rough Alignment*

We first roughly aligned the anchored parts towards a unique in-plane orientation using gravity as the driving force. On a tilted alignment template, the free parts slid away, and the anchored parts tended to rotate about their pegs until the minimum

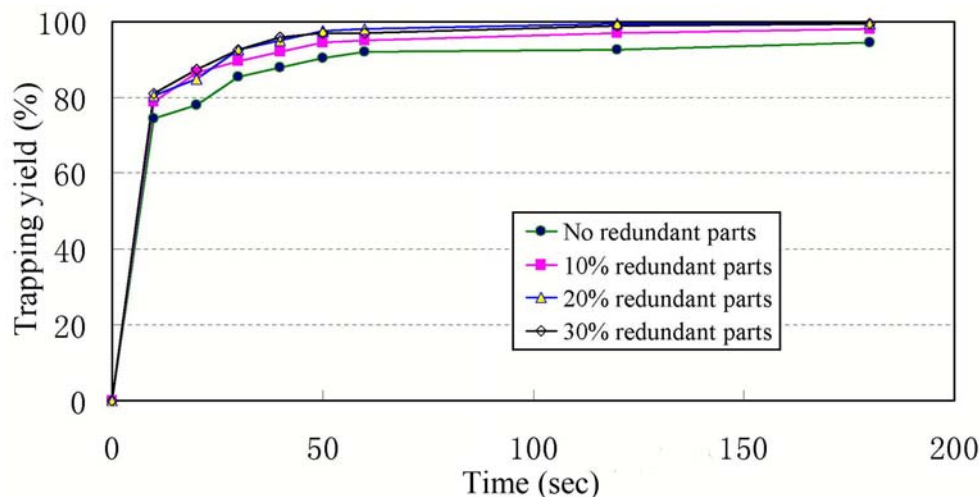


Figure 4.8: Trapping results of 2mm square silicon parts on a 164-receptor-site alignment template without and with 10-30% redundancy of parts.

potential energy was achieved, when their centers of mass arrived at the lowest height (Figure 4.9a-b). Friction blocking the rotation of the parts was relieved with gentle knocking on the edge of the alignment template. This alignment was rough because of three factors: (1) the tilt orientation of the alignment template was roughly controlled; (2) friction from the alignment template prevented exact alignment; (3) the layout design for the parts and the receptor sites defined the exact alignment when the pegs were concentric with the trenches. The maximum translational misalignment was the difference between the radii of the circular peg and the circular trench, which was 0.25mm. The maximum rotational misalignment we observed was about  $18^\circ$ .

#### *Fine Alignment*

Capillary-driven self-alignment can produce very high accuracy [SLH01], so we introduced capillary forces to minimize the misalignment of the previous gravity-driven assembly. The alignment template with anchored parts was placed in a steam environment, i.e., a chamber having a beaker of boiling water heated by a hotplate,

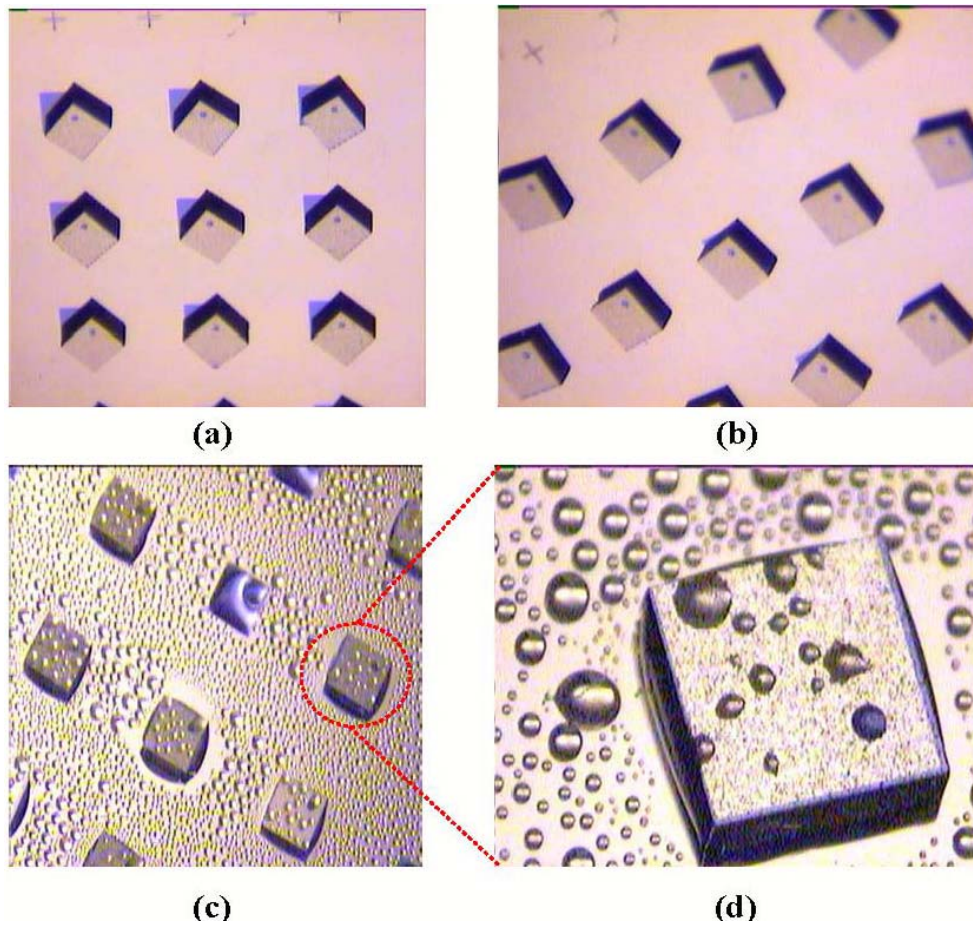


Figure 4.9: Unique aligning of 2mm square silicon parts: (a) parts roughly aligned by gravity on a tilted alignment template; (b) parts roughly aligned to the receptor sites on an appropriately tilted alignment template; (c) misalignment corrected by capillary-driven self-alignment when water steam is introduced to condensate on the alignment template and parts surface; (d) a zoom view of a part with water condensate.

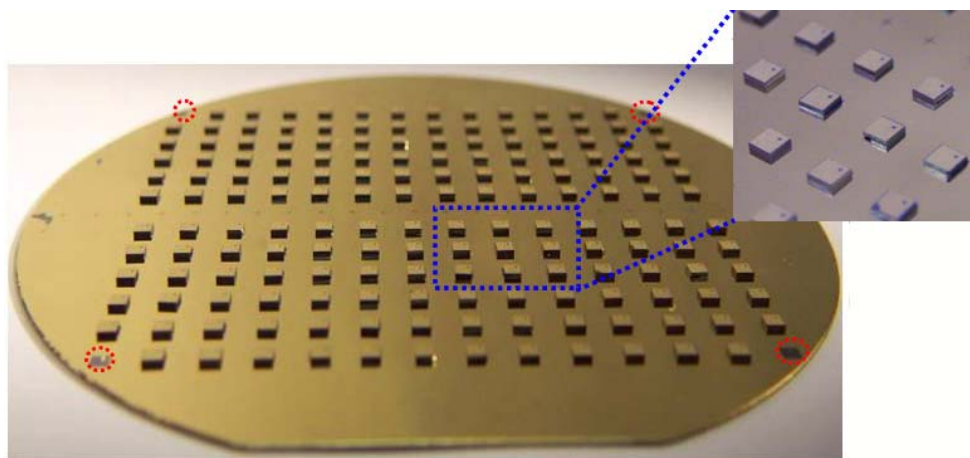


Figure 4.10: The assembly result: 164 2mm square silicon parts correctly assembled on a 4-inch alignment template (the 4 corner receptor sites were blocked by the covering Petri dish during the trapping experiment).

where water formed droplet-wise condensation on hydrophobic surfaces and film-wise condensation on hydrophilic surfaces (Figure 4.9c-d). The hydrophilic sidewall of the parts was continuously covered with water. The water on the sidewalls entered the capillary gaps between the parts and the hydrophilic receptor sites, and then lubricated the parts so that they could self-align to the receptor sites to minimize total interfacial energies. Finally water was evaporated when the alignment template was placed on a hotplate. The final assembled array of parts is shown in Figure 4.10. We observed that the misalignments from the previous rough alignment were greatly reduced: maximum rotational and translational misalignments became  $3^\circ$  and  $50\mu\text{m}$ , respectively.

#### 4.4 *The Dry Assembly Process (DUO-SPASS)*

Virtually all current assembly techniques having parallel assembly capabilities are performed in aqueous environments, e.g. fluidic shape-directed self-assembly [SY98, SYHV99] and capillary-driven self-assembly [JTS<sup>+</sup>02,SLH01,FWB04]. In an aqueous

environment, liquid flow introduces parts to receptor sites and removes unassembled parts from the assembly template. But for microchips with exposed movable microstructures, a completely dry assembly process is a better choice because these microstructures are easily stuck by surface tension of liquid residue from a wet assembly process. A completely dry assembly process is also required for microchips with materials sensitive to aqueous environments.

#### 4.4.1 *Design Rules for Alignment Features*

The dry assembly process is based on two-stage shape recognition between complementary features on parts and receptor sites, and is schematically shown in Figure 4.11. The first shape recognition takes place between a circular peg (CP) on the part and a circular trench (CT) on the receptor site, and the second shape recognition is accomplished between a cross peg (XP) on the part and a cross trench (XT) on the receptor site. The following design rules should be observed for appropriate two-stage shape recognition: (1) The circular peg is offset from the center of mass and two times as high as the cross peg. (2) The circular trench has a greater diameter than the cross peg for fast anchoring of parts, but the circular trench diameter has an upper limit, which prevents two circular pegs of two neighboring parts or one cross peg from entering one circular trench, i.e., one circular trench is assigned exclusively to one circular peg to guarantee one-to-one registration and correct alignment. This is analogous to the condition in Section 4.3, Equation (4.1). (3) The cross trench has a greater width than the cross peg beam to anchor the cross peg quickly, but a smaller width than the diameter of the circular peg to exclude the circular peg. (4) The space between receptor sites is large enough for two neighboring parts to rotate without blocking each other and unassembled parts to slide through it. From the exact alignment layout (Figure 4.12), we can determine the maximum misalignments: the maximum translational misalignment is equal to the clearance between the cross trench and cross peg, and the maximum rotational misalignment is  $\tan^{-1}(2\Delta/L)$ ,

where  $L$  is the length of the longer cross peg beam. Clearance  $\Delta$  is chosen for the cross peg to enter the cross trench easily and is independent of the part size, while  $L$  can be as large as possible to obtain a minimum rotational misalignment.

#### *4.4.2 Fabrication of Parts and the Alignment Template*

##### *Parts*

Diced silicon parts with dimension  $1\text{mm} \times 1\text{mm} \times 0.5\text{mm}$  were used to demonstrate the dry assembly process. The dimension of the longer cross peg beam is  $1\text{mm} \times 50\mu\text{m} \times 35\mu\text{m}$ , and the diameter and height of the circular peg are  $200\mu\text{m}$  and  $65\mu\text{m}$ , respectively. We fabricated the circular pegs and cross pegs with different heights on a  $\text{Ø}100\text{mm}$  silicon substrate by using two subsequent DRIE processes (Figure 4.13): a layer of  $3900\text{Å}$  thermal oxide was grown on the silicon substrate and patterned by etching to be left only on the cross peg areas, then photoresist AZ4620 was spincoated and patterned to be a DRIE mask protecting only the circular peg areas, and the patterned oxide acted as a DRIE mask with a very slow etching rate (approximately 1% of silicon etching rate) during the 1<sup>st</sup> DRIE and was completely removed by an oxide etchant before the 2<sup>nd</sup> DRIE, therefore the heights of the cross pegs and circular pegs were respectively determined by the 1<sup>st</sup> DRIE and both DRIEs. After the pegs were fabricated on the silicon substrate, we deposited a layer of TiW/Au ( $50/800\text{Å}$ ) on the backside of the silicon substrate and patterned it via double-sided lithography to form marks indicating the positions of the circular pegs.

##### *Alignment Template*

The recessed features for the receptor site have complementary shapes with larger dimensions for easier shape-matching: a cross trench is  $40\mu\text{m}$  greater in width than the cross peg, and the diameter of the circular trench is  $300\mu\text{m}$  greater than that of the circular peg, and both the cross trench and circular trench are  $70\mu\text{m}$  in depth.

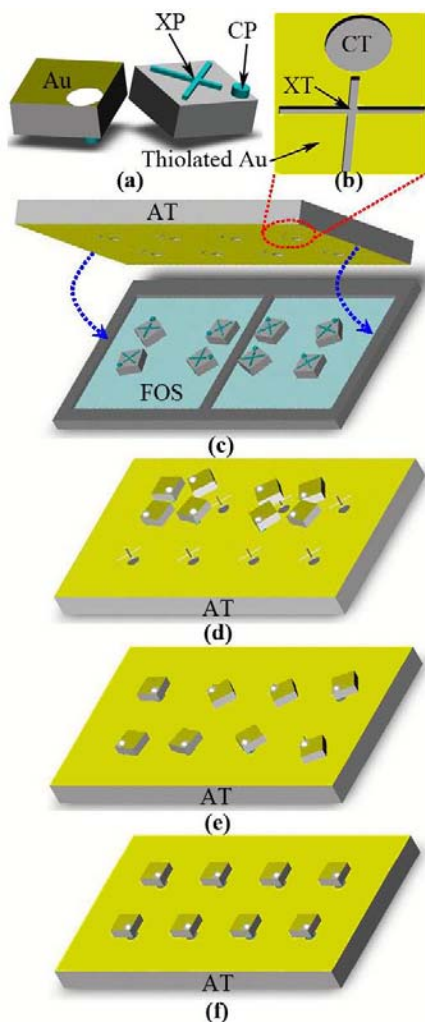


Figure 4.11: Schematic overview of the DUO-SPASS process to parallel assemble square micro-parts: (a) top and bottom views of a silicon part (the bottom face has a circular peg (CP) and a cross peg (XP), and the circular peg has twice the height of the cross peg; the top face is coated with gold, and the opening in the gold layer marks the position of the circular peg); (b) trenches of a receptor site on the alignment template (AT); (c) bulk parts face-oriented on an orbital shaken face-orienting substrate (FOS) and then sandwiched by adding an alignment template; (d) parts palletized to the alignment template with their peg sides facing downwards; (e) parts one-to-one anchored to receptor sites by orbital shaking: the circular pegs fall into the circular trenches (1<sup>st</sup> shape recognition); (f) parts rotated by orbital shaking introduced torques until their cross pegs fall into the cross trenches (2<sup>nd</sup> shape recognition).



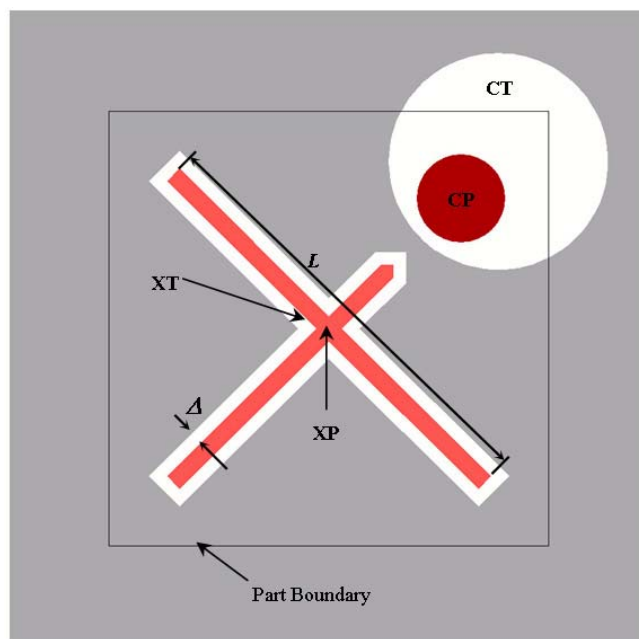


Figure 4.12: A schematic top view of the exact alignment between a part and a receptor site: the clearance  $\Delta$  between the cross peg (XP) and cross trench (XT) determines maximum alignment error.

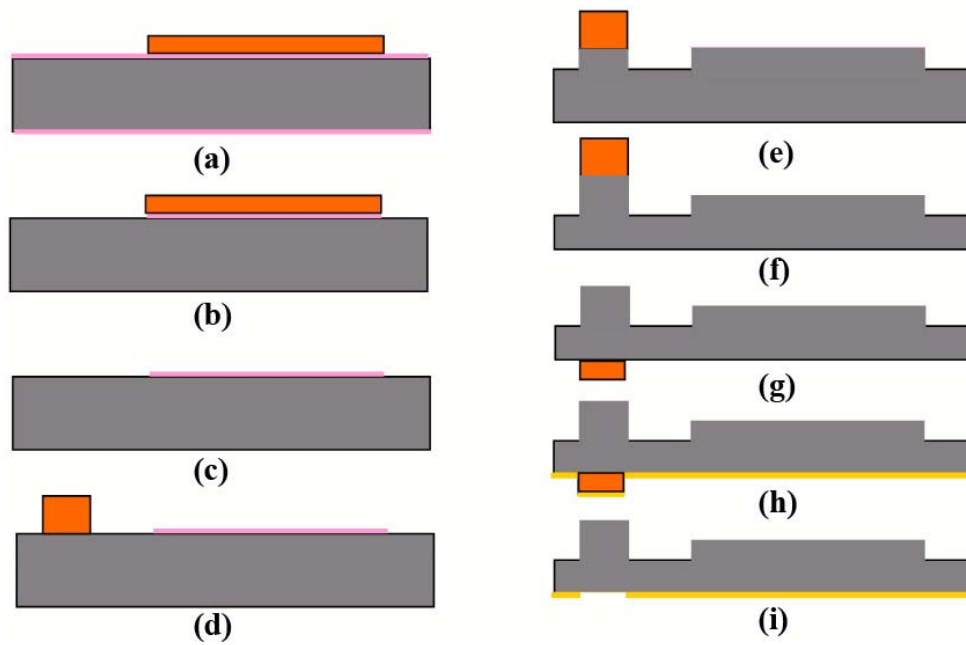


Figure 4.13: Fabrication steps for the aligning features on a part with double DRIE processes: (a) AZ1512 spincoated and patterned on an oxidized silicon wafer; (b) exposed oxide etched by BOE; (c) AZ1512 stripped; (d) AZ4620 spincoated and patterned; (e) exposed silicon etched by DRIE; (f) remaining oxide etched by BOE; (g) AZ4620 stripped and AZ1512 spincoated and patterned on backside of wafer; (h) Au deposited on backside; (i) AZ1512 stripped and Au on top of it lifted off.

The receptor site trenches were fabricated by a single DRIE process. We fabricated two Ø100mm alignment templates respectively having a polar/orthogonal array of 397/720 receptor sites. For simplicity, we describe the complete assembly process only for the polar 397-receptor-site alignment template.

To reduce sliding friction of the silicon alignment template, we deposited a layer of TiW/Au (50/800Å) and soaked the alignment template in a 1mmol alkanethiol  $\text{CH}_3(\text{CH}_2)_{11}\text{SH}$  (diluted in ethanol) solution overnight for the Au surface to adsorb a SAM. The thiolated gold surface has a lower friction coefficient than that of a silicon surface, so that less agitation is required to move parts on the alignment template.

#### 4.4.3 *Uniquely Face-orienting Bulk Parts*

On an orbitally shaken substrate, the silicon part can not rest on its face with alignment pegs in a stable way, because the part is tilted by its cross peg and easily flipped by the centrifugal force introduced by orbital shaking. Initially bulk silicon parts were stored in a container with random face orientations. We used orbital shaking to orient all the parts to face the same direction with their pegs on a substrate.

A face-orienting substrate (FOS) has an array of trenches, which confine parts locally. We fabricated this substrate out of an oxidized Ø100mm silicon substrate with TAMH etching: oxide was first patterned to produce the silicon etching mask, and 4 hours etching at 90°C resulted in 240µm deep trenches.

Bulk silicon parts were uniquely face-oriented on a face-orienting substrate by orbital shaking. 600 parts (about 50% redundant parts aiming for a high assembly yield) were poured with an approximately uniform distribution onto a face-orienting substrate attached to the platform of an orbital shaker. Then the shaker ran at 200rpm for about 1 minute and its centrifugal force flipped over all but 4 tilted parts onto their flat faces, while all the other parts stayed resting on their flat faces (Figure 4.14a). All the remaining 4 tilted parts had been kept immobile by surrounding parts. In order to face-orient bulk parts and keep them locally confined, the orbital shaker needs to

be run within a narrow speed range of about 50rpm: a speed higher than 230rpm can cause parts moving across the face-orienting substrate and parts tend to be crowded into a few substrate trenches, and a speed lower than 180rpm cannot flip the tilted parts<sup>1</sup>. The upper speed limit is determined by the trench depth. The lower speed limit depends on the part tilt angle or the ratio between the peg height and the part side length. The parts' "preference" not to rest on their peg sides is due to the higher centers of gravity in this position and the higher friction at the off-center peg tips, which in combination cause larger torques during orbital shaking.

#### *4.4.4 Palletizing Parts*

We placed the alignment template (Figure 4.14b) with its receptor sites facing the face-orienting substrate to sandwich the parts, and turned them over. Thereby, the patterned ridges on the substrate kept the parts in place. Then we removed the substrate, and 99% of the parts were transferred to the alignment template except very few parts sticking to the face-orienting substrate due to adhesive forces.

#### *4.4.5 The Assembly Process*

We utilized a mechanism based on two-stage shape recognition to assemble the palletized parts. The alignment template surface coated with thiolated Au has less sliding friction than a silicon surface, and to reduce friction effects even further, we attached the alignment template to an ultrasonic stage mounted on an orbital shaker. To move the parts around without flipping over, the orbital shaker was run in a speed range whose limits were given as follows: the lower speed limit introduced a centrifugal force just enough to overcome the friction; the upper speed limit caused the tilted

---

<sup>1</sup>This bound is lower than that in Section 4.3.5 (>250rpm) because here parts are smaller (1mm) with taller pegs, and thus are less stable to rest on their pegs.

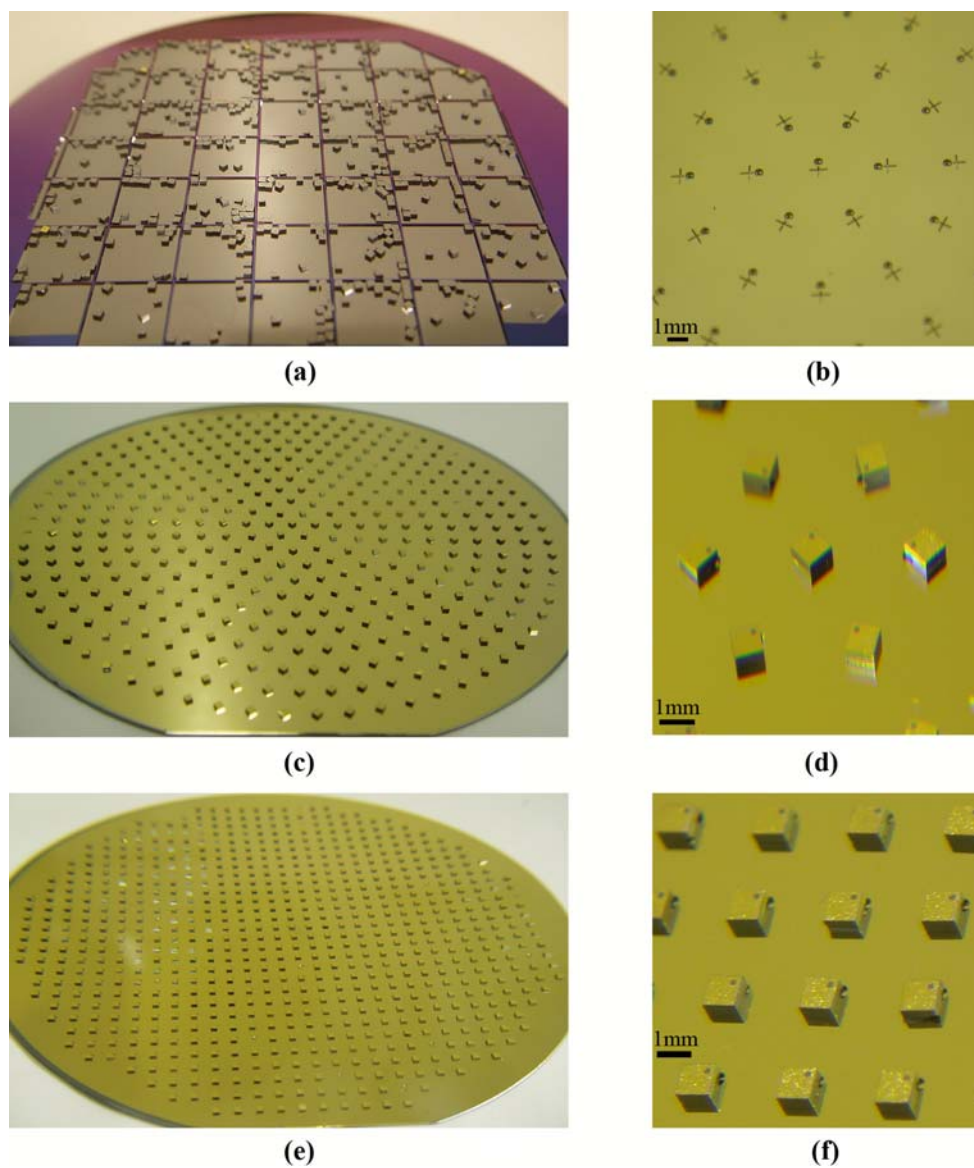


Figure 4.14: Optical photographs of templates and assembly results: (a) after 1 minute of orbital shaking, only 4 silicon parts stay tilted by their pegs on the  $\text{\O}100\text{mm}$  face-orienting substrate; (b) a partial view of an alignment template with a polar array of receptor sites; (c) 388 silicon parts assembled on the  $\text{\O}100\text{mm}$  alignment template with a polar array of 397 receptor sites; (d) zoom-in view of the center of the alignment template; (e) 710 silicon parts assembled on the  $\text{\O}100\text{mm}$  alignment template with an orthogonal array of 720 receptor sites; (f) zoom-in view of a  $4\times 3$  section of the array of receptor sites.

parts to flip over. We ran the orbital shaker at 110rpm<sup>2</sup>. The moving parts were first anchored to the receptor sites when their circular pegs fell into the circular trenches, and came to rest horizontally on their cross pegs. Because the circular pegs were offset from the center of mass, the centrifugal force from orbital shaking exerted torques on the anchored parts to drive them to rotate about their circular pegs until their cross pegs fell into the cross trenches; at this point the parts were fixed to the uniquely defined orientations. After 10 minutes agitation, 388 receptor sites were correctly registered with parts, which indicated a yield of 97.7% (Figure 4.14c-d). We removed the unassembled parts from the alignment template by tilting the ultrasonic stage so that gravity drove them to slide away.

We also assembled the same silicon parts on a Ø100mm alignment template with 720 receptor sites according to the above process steps. 50% redundant parts were used. 710 parts were correctly assembled within 10 minutes, i.e., the assembly yield reached 98.6% (Figure 4.14e-f).

The maximum alignment errors are determined by the design of the complementary features on the parts and the receptor sites. The maximum translational misalignment is equal to the clearance  $\Delta$  between the cross peg and the cross trench, which is 20 $\mu$ m in our design. The maximum rotational misalignment is about 2°.

#### 4.4.6 *Assembly Defects*

During the assembly process, we noticed two major types of defects: (1) occasionally unassembled parts adhered to the assembled parts; (2) parts resting on their flat faces were immobile during the agitation, which blocked other moving parts. The part sticking was mainly caused by contamination from the previous process steps. Because the face-orienting process did not have perfect 100% yield, some parts rested on their flat faces after palletizing. We manually removed these parts to avoid the 2<sup>nd</sup>

---

<sup>2</sup>This speed is lower than that in Section 4.3.5 mainly because here an ultrasonic vibration stage is used to reduce sliding friction.

type of defects. In addition, we kept the vibration intensity of the ultrasonic stage low enough to prevent parts from flipping over.

#### **4.5 Wafer-Level Flip-chip Bonding**

In this dissertation, we focus on a novel approach for palletizing and assembling of parts using uniquely orienting self-assembly, so that we used dummy silicon parts without any functional circuit or interconnect pad to demonstrate all the previous process steps. As for the final step of our packaging strategy, we propose a wafer level flip-chip bonding technique to package functional microchips onto a chip carrier template (CCT). The flip-chip bonding can be achieved via solder bumps deposited on a chip carrier template (Figure 4.1f) or a layer of anisotropic conductive film [fii], as currently done in well-established industrial IC packaging processes.

#### **4.6 Application to Non-silicon Parts**

Both the semi dry (semi-DUO-SPASS) and dry (DUO-SPASS) assembly processes can be also applicable to parts made of non-silicon materials, when combined with additive fabrication techniques for the pegs on the parts. For the semi dry process, the single circular peg can be easily fabricated with a single SU8 casting process. For the dry process, we fabricated two high-aspect-ratio pegs on each part with different heights out of the photodefinable polymer SU8-2025 (MicroChem Corp., MA, USA) with the following major fabrication process steps (Figure 4.15): (1) 1<sup>st</sup> layer of SU8 was spincoated and UV light exposed with a mask having transparent areas for cross pegs; (2) 2<sup>nd</sup> layer of SU8 was spincoated and UV light exposed with a mask having transparent areas for circular pegs; (3) SU8 was developed, and then only the circular pegs and cross pegs exposed by UV light were left on the substrate. An array of SU8 pegs is shown in Figure 4.16. During the assembly of the parts with SU8 pegs (also 50% redundant parts provided) on the previous 397-receptor-site alignment template,

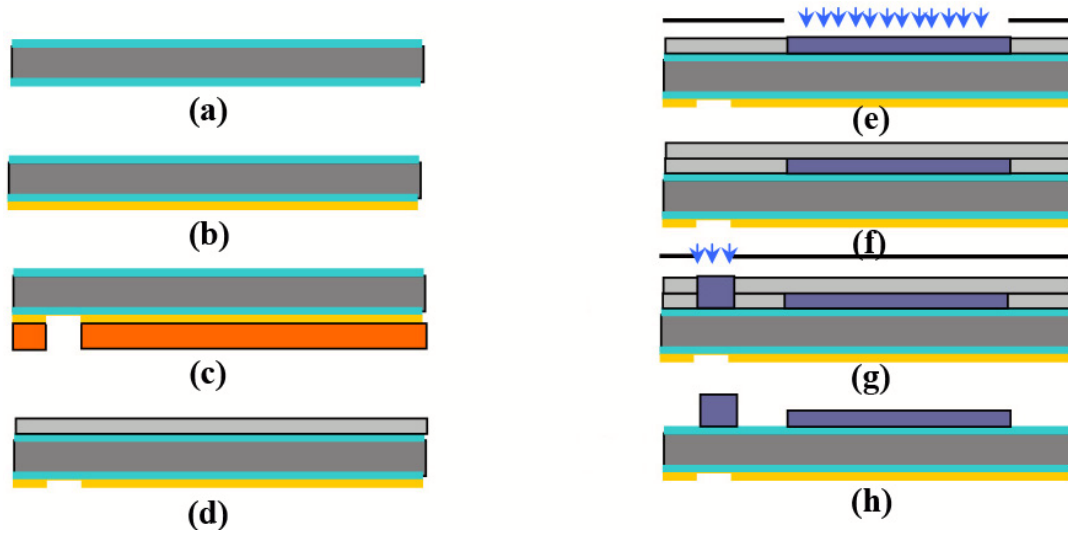


Figure 4.15: Fabrication steps for the aligning features on a part with double layers of SU8: (a) LPCVD nitride deposited on the silicon wafer; (b) Au deposited on backside of wafer; (c) AZ1512 is photolithographically patterned on Au to expose peg marker areas and Au etched in an Au etchant; (d) a layer of SU8 spincoated on the front side; (e) SU8 exposed to UV light with a mask protecting the areas other than cross alignment pegs; (f) second layer of SU8 spincoated; (g) SU8 in the circular peg areas exposed to UV light; (h) SU8 developed.

we obtained a lower yield (about 80%) within longer time (half an hour) than the parts with silicon pegs, which is mainly because SU8 has a greater friction coefficient than silicon.

#### 4.7 Conclusions and Discussions

We have presented a wafer level packaging strategy for micro-device chips based on uniquely orienting self-assembly, and demonstrated semi dry assembly of 2mm square silicon parts and completely dry assembly of 1mm square silicon parts on 4-inch alignment templates. Both assembly processes have yields close to 100%. Our assembly strategy can also be applied to flat parts of any shape with a larger or smaller scale if the alignment feature design rules are observed. Adhesive and friction forces, which



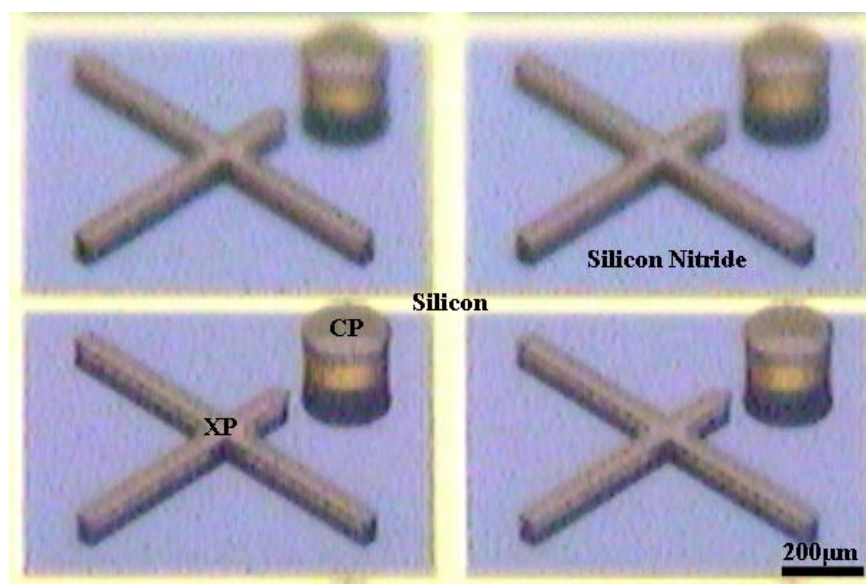


Figure 4.16: An optical microscope image of a  $2 \times 2$  section of an array with SU8-2025 circular pegs (CP) and cross pegs (XP) on a 3-inch silicon substrate, before dicing into individual parts.

are the major causes for potential failures of our assembly techniques, become more significant compared with gravitational forces for smaller parts. Our assembly method has been demonstrated with 1mm and 2mm square parts, and we believe that it can assemble larger device chips with dimension up to centimeters which are less affected by adhesive forces. In micro-domains, both the adhesive and frictional forces are approximately proportional to contact area. The adhesive forces come mainly from electrostatic interactions, van der Waals attractive forces and surface tension from adsorbed moisture on the part and the substrate [Fea95b]. The gold face of the alignment template can eliminate the electrostatic charges at the bottom faces of parts, but not the charges at the sidewalls of parts, which can cause parts sticking to each other. A photoionizer can effectively neutralize electrostatic charges on any exposed surface by introducing ions into the surrounding atmosphere. Adsorbed moisture can be reduced by heating the alignment template or performing the assembly in

a vacuum environment. With good control of environmental humidity, electrostatic charges and sliding friction, we believe that our assembly process can handle parts of much smaller size.

An accurate model for the friction and stiction forces at the part edges and peg tips would be valuable for design optimization. A systematic approach would study the balance between these stiction forces and the orbital shaker-induced torque that causes part flipping. Parts with minimal peg heights may be desired because of manufacturing constraints.

Peg height is a key factor for proper assembly of parts in both assembly processes: (1) a minimum height of the circular peg is required for reliable anchoring of parts:  $\sim 20\mu\text{m}$  for the semi DUO-SPASS process,  $\sim 30\mu\text{m}$  higher than the cross peg for the DUO-SPASS process due to ultrasonic vibration to relieve sliding friction; (2) minimum orbital shaking speeds to move and flip over parts (denoted as  $\omega_m$  and  $\omega_f$ ) depend on the part/substrate contact area and the ratio between height of the circular peg and side length of the part, respectively.

In our experiments we continuously monitored the progress of the assembly, but the goal is to run these processes completely open-loop. We believe that in an industrial setting, simply following a timed recipe will suffice (see Fig. 8 with the trapping yield as a function of time). But expecting 100% yield may be unrealistic for large assemblies, and an automated vision system with a precision robot could be used to fix the few remaining defects.

Our packaging mechanism itself applies no upper limit on the alignment template size. All the agitations required in the assembly process are orbital shaking, which introduces centrifugal forces evenly distributed all across the shaker platform. The orbital shaker platform supported by three rotating arms can be easily expanded. High-aspect-ratio trench features on the alignment template can be fabricated with many available techniques such as DRIE (only for silicon templates), molding, and others [CP97,KPL<sup>+</sup>02,ZC03]. These trench fabrication techniques limit the alignment

template size.

In addition to wafer level packaging of micro-device chips, our assembly techniques without the final bonding step can also be used as part feeding and palletizing for robotic assembly systems.

## Chapter 5

**VERTICAL AND HORIZONTAL PARALLEL ASSEMBLY****5.1 Introduction**

Parallel micro-assembly techniques enable fast integrating and packaging of micro-devices. During the past decade, several parallel micro-assembly techniques have been developed and published: (1) fluidic shape-directed self-assembly [YS94]; (2) capillary-driven self-assembly [JTS<sup>+</sup>02, SLH01, XHF<sup>+</sup>03, ZBJ04, FWB04]; (3) electrostatically driven self-assembly [BGC<sup>+</sup>98, CHP95]; (4) magnetically assisted self-assembly [PRF02]. Micro-components are usually singulated in rectangular (or square) shapes from a substrate by dicing (the last fabrication step), thus they have vertical edges, i.e., the top and bottom surfaces are geometrically identical and can therefore not be distinguished solely based on shape by any type of receptor site. In addition, a rectangle has rotational symmetry of order 2, and a square has order 4. To assemble such components, none of the above assembly techniques can effectively avoid uncertainties of face and/or in-plane orientations. Usually a micro-component has electrical interconnects on a single face, so it must be mounted with unique face-orientation onto a substrate to achieve electrical connections to a circuit on the substrate via flip-chip bonding. Such a component face having electrical interconnects is usually called “bonding face”.

The DUO-SPASS processes described in Chapter 4, based on one- or two-stage shape recognition, require protruding pegs on parts, thus they are not suitable for applications requiring flat part surfaces. This chapter presents a novel assembly process based on both shape recognition and capillary-driven mechanisms. This assembly

process has the following capabilities: (1) highly dense assembly of peg-free micro-components (e.g., useful for assembly of an LED display to achieve good resolution); (2) process in an air environment; (3) two controlled modes of part mounting: vertical and horizontal; (4) unique face-orienting of parts for horizontal mounting; (5) multi-batch assembly of various types of components, even with same dimensions; (6) high surface coverage on a substrate achieved by multi-batch assembly. With this list of capabilities available to satisfy a wide range of manufacturing requirements, applications such as, e.g., micro-device packaging, mass production of RFID tags and fabrication of LED displays may benefit from this parallel micro component-to-substrate assembly process. Mechanically diced  $790\mu\text{m}$  square silicon parts with a single hydrophobic face are used for the following proof-of-concept demonstrations.

## **5.2 Parallel Assembly Strategy**

A typical parallel micro-assembly process has two major goals: (a) micro-components are delivered to receptor sites with one-to-one registration; (b) micro-components contact receptor sites with their bonding faces. To achieve these assembly goals, we develop the following strategy (see Figure 5.1, each component has one unique hydrophobic face). (1) Bulk components are distributed into apertures on an aperture plate and each aperture is occupied with exactly one vertically standing component due to geometric constraints, and the top edge of the component levels with the aperture plate surface. (2) Components from the evenly populated aperture plate are transferred onto an array of water covered receptor sites on a palletizing plate via surface tension forces, i.e., the first assembly goal is achieved and the components are vertically attached or mounted. (3) Vertically standing components are laid down to be horizontally mounted with unique face orientations, and then they self-align with the receptor sites by minimizing interfacial energies (such a capillary-driven self-alignment process can achieve sub-micron accuracy [SLH01]). (4) Components are

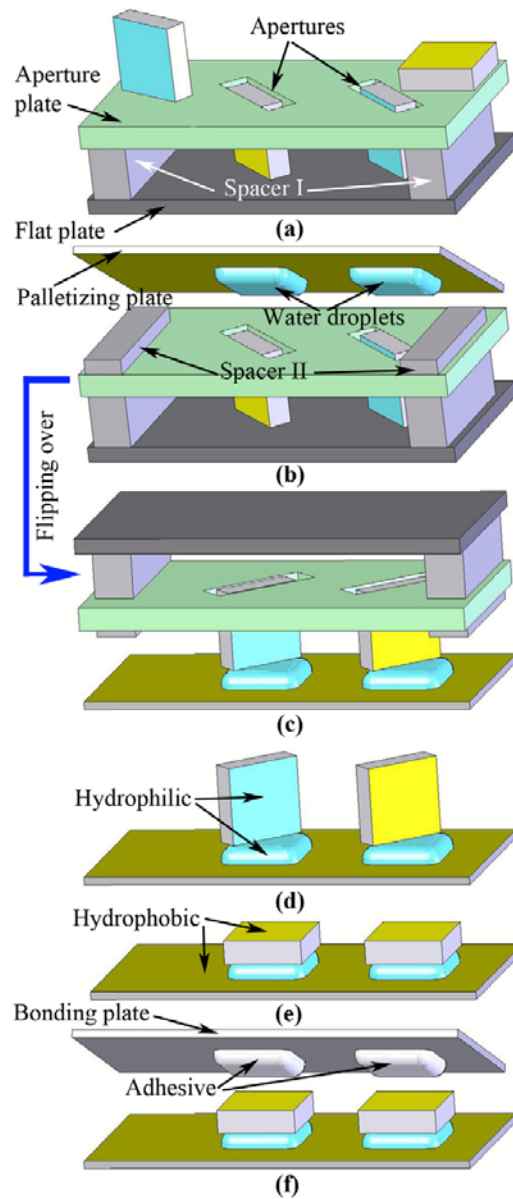


Figure 5.1: Schematic overview of the assembly process: (a) bulk parts fall into apertures vertically; (b) a palletizing plate carrying water droplets is aligned with the aperture plate; (c) the plates are flipped over to transfer parts onto water droplets; (d) parts stand on receptor sites; (e) parts rotate to adhere to the palletizing plate with their hydrophilic oxide faces; (f) parts are permanently bonded to a bonding plate via wafer level flip chip bonding.

permanently bonded to a bonding plate via wafer level flip-chip bonding. If step (3) is skipped, then components are vertically mounted, which indicates (a) capability to achieve denser assembly with smaller footprints and (b) benefits for assembly of optical or radio frequency micro-components due to the special face orientations.

### 5.3 *Fabrication and Surface Treatment*

During the experiments, we used two types of silicon parts (flat-edge and step-edge), a silicon aperture plate, a glass palletizing plate and a bonding plate.

**Flat-edge** and **step-edge silicon parts** were respectively fabricated by mechanical dicing from two 4-inch thermally oxidized silicon wafers with thickness of  $330\mu\text{m}$ . Before dicing, both wafers were sputter deposited with a layer of TiW/Au ( $50\text{\AA}/1000\text{\AA}$ ) on a single side, and the wafer for step-edge parts underwent an extra three-step process: (1) photoresist AZ4620 was spincoated and lithographically patterned (see Appendix for the recipe) to cover an array of  $590\mu\text{m}$  squares on the side without Au; (2) exposed silicon oxide was stripped in a buffered oxide etchant (BOE) with an etching rate of  $\sim 600\text{\AA}/\text{min}$ ; (3) exposed silicon was etched for 60 minutes by deep reactive ion etching (DRIE) to form  $\sim 190\mu\text{m}$  deep trenches. Then the silicon wafers were mechanically diced into  $790\mu\text{m}$  square parts (Figure 5.2). Diced parts were subsequently cleaned in acetone, isopropanol (IPA), and de-ionized (DI) water in a sonicator, and then collected onto a piece of filter paper and baked dry on a  $100^\circ\text{C}$  hotplate for 5 minutes. Finally bulk parts were soaked in a 1mmol alkanethiol  $\text{CH}_3(\text{CH}_2)_{11}\text{SH}$  solution (solvent is ethanol) overnight for a self-assembled monolayer (SAM) to selectively cover the Au surfaces. The results of water contact angle measurement using a FTA200 system (First Ten Angstroms Inc.) indicated: the thiolated Au surface was hydrophobic with a  $\sim 106^\circ$  contact angle, while the other part faces with native and thermal oxide (the edges have native oxide) remained hydrophilic with contact angles of  $\sim 35^\circ$  and  $\sim 45^\circ$ , respectively (Figure 5.3).

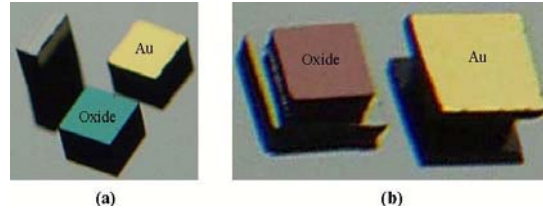


Figure 5.2: Optical images of flat-edge and step-edge parts: (a) top, bottom and side views of flat-edge parts ( $790\mu\text{m} \times 790\mu\text{m} \times 330\mu\text{m}$ ); (b) top and bottom views of step-edge parts (base dimension is  $790\mu\text{m} \times 790\mu\text{m} \times 140\mu\text{m}$ , and top dimension is  $590\mu\text{m} \times 590\mu\text{m} \times 190\mu\text{m}$ ).

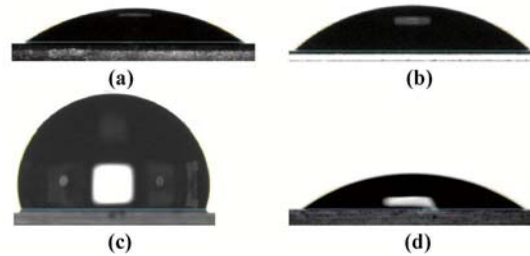


Figure 5.3: Microscope images of water droplets with different contact angles on different surfaces: (a) native oxide ( $35^\circ \pm 3^\circ$ ); (b) thermal oxide ( $45^\circ \pm 3^\circ$ ); (c) thiolated Au ( $106^\circ \pm 3^\circ$ ); (d) glass ( $35^\circ \pm 3^\circ$ ). **Note:** diced silicon parts have very limited surface areas for contact angle measurement, thus we used large silicon substrates, which were of the same type as the substrate used to fabricate the  $790\mu\text{m}$  square parts, with different surface coatings for (a)-(c).



A 4-inch **aperture plate** having 1000 apertures was fabricated from a  $330\mu\text{m}$  thick oxidized silicon wafer by a deep reactive ion etching (DRIE) process. First, photoresist AZ4620 was deposited and lithographically patterned on the silicon substrate. Second, a piece of dicing blue tape covered the back side of the substrate, and then the substrate was soaked in a BOE solution to completely remove exposed thermal oxide. The oxide on the back side was left to be an etch stop for the following DRIE process. Third, the substrate underwent a DRIE process for about 110 minutes, and then soaked in a BOE solution to remove oxide on the backside, thus through-hole apertures were formed. Finally, photoresist was stripped with acetone, and then the substrate was cleaned in IPA and DI water.

A **glass palletizing plate** was coated with patterned thiolated Au. First, a layer of TiW/Au ( $50\text{\AA}/1000\text{\AA}$ ) was sputter deposited on the glass substrate. Second, photoresist AZ1512 was spincoated and lithographically patterned to expose an array of  $790\mu\text{m}$  square gold areas. Third, exposed Au and TiW underneath were subsequently etched in an Au etchant (TFA type) and  $\text{H}_2\text{O}_2$ . Finally photoresist AZ1512 was stripped with acetone and the substrate was cleaned in IPA and DI water. The cleaned substrate was soaked in a 1mmol alkanethiol  $\text{CH}_3(\text{CH}_2)_{11}\text{SH}$  solution for Au areas to become hydrophobic by adsorbing a SAM, while the exposed glass squares were used as hydrophilic (Figure 5.3d) receptor sites.

A **glass bonding plate** was spincoated with AZ4620 and then AZ4620 was lithographically patterned to cover an array of  $790\mu\text{m}$  square bonding sites. The photoresist AZ4620 can be reflowed at  $\sim 175^\circ\text{C}$  [PCH04] for final bonding of micro-components.

#### 5.4 *Physical Modeling*

Unique face-orienting of micro-components, shown in Figure 5.1e, is a key factor to achieve correct mounting with electrical interconnections between the substrate and

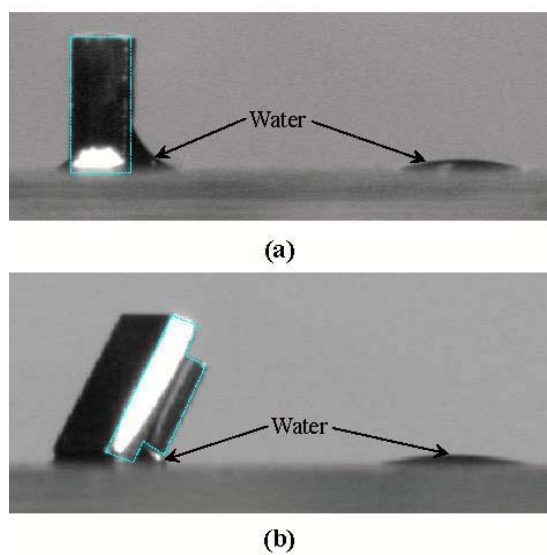


Figure 5.4: Microscopic side views of parts attached to receptor sites (the neighboring receptor sites are left unoccupied for comparison): (a) a flat-edge part standing vertically with its hydrophilic face to the right; (b) a step-edge part tilted with water gathering at the part's lower edge.

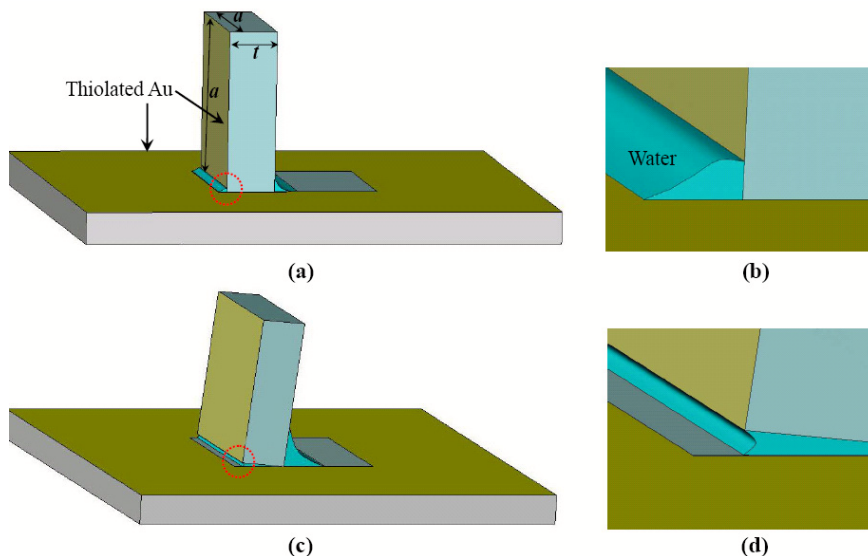


Figure 5.5: Schematic views of a vertically standing square part on a receptor site: (a) before steam condensation; (b) a zoom-in view of the circled area in (a); (c) after steam condensation (water condensate favors the hydrophilic part surface); (d) a zoom-in view of the circled area in (c).

the components. Microscopic views of a flat-edge silicon part and a step-edge silicon part respectively attached to two receptor sites by water droplets are shown in Figure 5.4. The required conditions to lay down the flat-edge and step-edge parts with unique face-orienting are respectively evaluated with the following two approximate physical models.

#### 5.4.1 Flat-Edge Parts

In Figure 5.4a, a flat-edge silicon part stands vertically with a significantly larger water meniscus on its right hydrophilic oxide face than its left hydrophobic Au face. Considering a part rotating about its lower right edge (shown in Figure 5.5), in total, there are three torques on the part: a clockwise (driving) capillary torque  $\tau_{cr}$  on the right face, a counterclockwise (restraining) capillary torque on the three left bottom

edges  $\tau_{cl}$ , and a counterclockwise (restraining) gravitational torque  $\tau_g$ . For simplicity, we consider the following situation: the part is rotating about its lower right edge for a very small angle  $\alpha$  and all the water left to the axis edge enters the small gap underneath the part as shown in Figure 5.5d, which brings about a maximum possible restraining capillary torque. In the following calculations, we assume the same contact angle  $\theta_c$  on all wetting surfaces.

According to the definition of a torque  $\boldsymbol{\tau}$ :

$$\tau = |\boldsymbol{\tau}| = |\mathbf{r} \times \mathbf{F}| = |\mathbf{r}||\mathbf{F}| \sin \theta \quad (5.1)$$

where  $\mathbf{F}$  and  $\mathbf{r}$  are respectively a force vector and its moment arm vector,  $\theta$  is the intersection angle between  $\mathbf{F}$  and  $\mathbf{r}$ . The gravitational and driving capillary torques can be respectively denoted by:

$$\tau_g = \rho a^2 t g t / 2 = \rho a^2 g t^2 / 2 \quad (5.2)$$

and

$$\tau_{cr} = \sigma a h_w \sin \theta_c \quad (5.3)$$

where  $\sigma$  is water surface tension;  $a$ ,  $t$  and  $\rho$  are respectively width (or length), thickness and mass density of the part;  $h_w$  is the wetting line height on the right face; and  $g$  is the gravitational constant.

The capillary torque  $\tau_{cl}$  consists of three components respectively along three edges. The component along the edge parallel to the axis is given by:

$$\tau_{cl1} = \sigma a t \sin \theta_c \quad (5.4)$$

To calculate the other two identical torque components respectively along the front and back lower edges which are perpendicular to the axis, we have to integrate over the thickness of the part  $t$ :

$$\tau_{cl2} = \int_0^t \sigma x \sin \theta_c dx = \sigma t^2 \sin \theta_c / 2 \quad (5.5)$$

Therefore, the counterclockwise capillary torque is represented by:

$$\tau_{cl} = \sigma t \sin \theta_c (a + t) \quad (5.6)$$

The following condition must be satisfied for the part to start rotating:

$$\tau_{cr} > \tau_{cl} + \tau_g \quad (5.7)$$

By combining Equations (5.2)-(5.7), we can calculate and obtain the minimum  $h_w$ :

$$h_w = \left[ 1 + \frac{\rho a^2 t g + 2 \sigma t \sin \theta_c}{2 \sigma a \sin \theta_c} \right] t \quad (5.8)$$

To evaluate the minimum  $h_w$  for our fabricated flat-edge silicon parts, we plug the following values into Equation (5.8):  $\rho=2.23\text{g/cm}^3$ ,  $a=790\mu\text{m}$ ,  $t=330\mu\text{m}$ ,  $g=9.8\text{N/kg}$ ,  $\sigma=72\text{dyne/cm}$ ,  $\theta_c=45^\circ$ . The minimum  $h_w$  is about  $486\mu\text{m}$ , which is greater than the value  $\sim 290\mu\text{m}$  in Figure 5.4(a). To raise the wetting level, we introduced steam condensation on the part surfaces (details in Section 5.5.3).

As the part starts to rotate, the rotating continues because (1) the initially counterclockwise gravitational torque becomes less and less, and then clockwise when the center of mass goes across the axis; (2) the capillary torques  $\tau_{cr}$  and  $\tau_{cl}$  respectively become greater and less with an assumption of constant water volumes: as  $\alpha$  increases, the wetting areas on the right face and bottom edge face of the part becomes greater and less, respectively, and the capillary torques are proportional to the wetting areas when the contact angle  $\theta_c$  is assumed to be constant.

#### 5.4.2 Step-Edge Parts

A step-edge part consisting of two segments, respectively called “base segment” and “top segment” (the base segment is larger), stands on a receptor site in a leaning pose (edges of both segments in contact with the receptor site) rather than a vertical pose (only the edge of the base segment in contact with the receptor site) with an

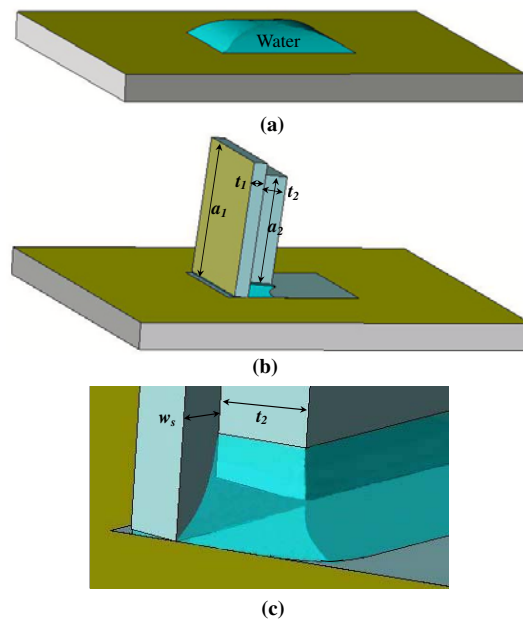


Figure 5.6: Schematic views of mounting of a step-edge part: (a) a receptor site covered with a water droplet; (b) a step-edge part in a near-vertical state; (c) a zoom-in view of the lower right corner of the part wetted by water.

appropriate design, which can be derived from the following approximate physical modeling. The dimension labels  $a_1$ ,  $a_2$ ,  $t_1$ ,  $t_2$  and  $w_s$  are shown in Figure 5.6b-c.

Similar to the modeling of a flat-edge part, we consider a simple situation shown in Figure 5.6b-c: the part is rotating for a very small angle  $\beta$  about the lower right edge of the base segment, and there are three torques: a clockwise (driving) capillary torque  $\tau'_{cr}$  along the right lower edges, a counterclockwise (restraining) capillary torque  $\tau'_{cl}$  along the left lower edges, and a gravitational torque  $\tau'_g$ .

By using the formula of the center of mass (COM) position for a composite object:

$$x_{com} = \frac{x_1 m_1 + x_2 m_2}{m_1 + m_2} \quad (5.9)$$

where  $x_i$  and  $m_i$  are respectively COM position and mass of an individual component of the object, we can calculate the COM position of the step-edge part (the coordinate origin is chosen at the segment interface, and the positive axis perpendicular to the segment interface points towards the top smaller segment):

$$x_{com}^{sep} = \frac{a_2^2 t_2^2 - a_1^2 t_1^2}{2(a_2^2 t_2 + a_1^2 t_1)} \quad (5.10)$$

The COM will be at the segment interface when the following relation is satisfied:

$$a_1 t_1 = a_2 t_2 \quad (5.11)$$

Our part design shown in Figure 5.2b is according to Equation (5.11), thus the gravitational torque  $\tau'_g$  is zero when the part starts to rotate.

Now we calculate the other two capillary torques  $\tau'_{cl}$  and  $\tau'_{cr}$ . The situation of wetting along the three lower edges left to the axis is the same as the flat-edge part, therefore we can write the following expression according to Equation (5.6):

$$\tau'_{cl} = \sigma t_1 \sin \theta_c (a_1 + t_1) \quad (5.12)$$

By comparing two neighboring receptor sites in Figure 5.4b, we can find: a water droplet covers 100% of the unoccupied receptor site, and an attached step-edge part

causes the water droplet to shrink its base and wet only the area directly below the step edge. For simplicity, we assume (1) wetting along the lower edges of the top segment as schematically shown in Figure 5.6c, (2) minimum wetting areas (i.e. the moment arm length is calculated from the axis to the part edge) and the same contact angle  $\theta_c$  on all three vertical faces of the top segment. The torque component along the right lower edge of the top segment can be expressed as:

$$\tau'_{cr1} = \sigma a_2 \sqrt{w_s^2 + t_2^2} \sin \left[ \tan^{-1} \left( \frac{t_2}{w_s} \right) + \theta_c \right] \quad (5.13)$$

The other two identical torque components respectively along the front and back lower edges (perpendicular to the axis) of the top segment should be integrated over the thickness  $t_2$ :

$$\tau'_{cr2} = \int_0^{t_2} \sigma x \cos \theta_c dx = \sigma t_2^2 \cos \theta_c / 2 \quad (5.14)$$

The driving capillary torque is the sum of the above three components:

$$\tau'_{cr} = \sigma a_2 \sqrt{w_s^2 + t_2^2} \sin \left[ \tan^{-1} \left( \frac{t_2}{w_s} \right) + \theta_c \right] + \sigma t_2^2 \cos \theta_c \quad (5.15)$$

The following relation must be satisfied for the step-edge part to start rotating from its vertical state.

$$\frac{\tau'_{cl}}{\tau'_{cr}} < 1 \quad (5.16)$$

By calculating with the following values:  $\sigma = 72 \text{ dyne/cm}$ ,  $\theta_c = 45^\circ$ ,  $a_1 = 790 \mu\text{m}$ ,  $a_2 = 590 \mu\text{m}$ ,  $t_1 = 140 \mu\text{m}$ ,  $t_2 = 190 \mu\text{m}$  and  $w_s = 100 \mu\text{m}$ , we can get the ratio of these two torques:

$$\frac{\tau'_{cl}}{\tau'_{cr}} \approx 0.67 < 1 \quad (5.17)$$

Equation (5.17) explicitly indicates that such a step-edge part can not stand steadily in a vertical pose due to the unbalanced capillary torques. The steady state for the part is resting on its step edge in a leaning pose.

To lay down such leaning parts, we can apply a pressing plate on the top edges and parallel to the substrate (Figure 5.7). The pressing applies a torque on the titled



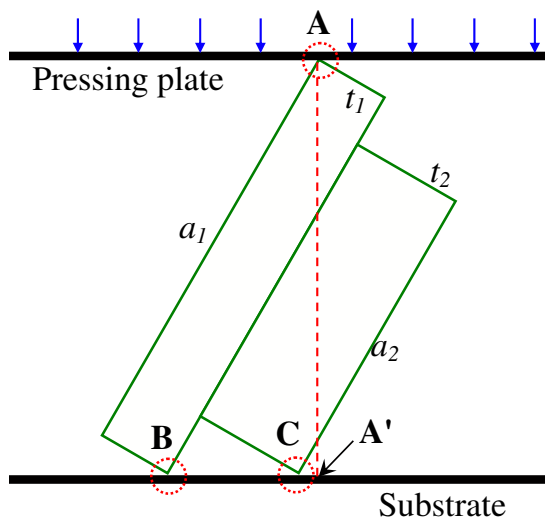


Figure 5.7: A schematic graph for a pressing plate to lay down a tilted step-edge part: the projection of point  $A$  on the substrate, denoted as  $A'$ , must be to the right of the point  $C$ .

part, but the rotation direction depends on the projection of the contact point  $A$  on the substrate, denoted as  $A'$ : the part stays in the leaning pose if  $A'$  is between  $B$  and  $C$ ; the part is laid down if  $A'$  is located to the right of  $C$ . For our part design,  $A'$  is about  $30\mu\text{m}$  to the right of  $C$ .

### 5.5 Experimental Implementation

We accomplished parallel mounting of micro-components on a substrate with three major steps: positioning, orienting and bonding of micro-components, i.e., bulk micro-components were first distributed to an array of receptor sites, and then uniquely face-oriented, and finally permanently bonded to a bonding substrate. We demonstrate a complete assembly process for the flat-edge parts in Sections 5.5.1-4. The step-edge parts share all the assembly steps with the flat-edge parts except the intermediate orienting step in Section 5.5.3, and Section 5.5.5 presents the special orienting step

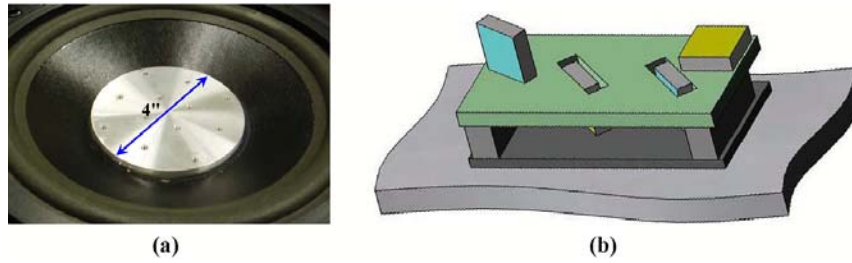


Figure 5.8: Experimental setup for parts falling into apertures: (a) an optical image of a modified subwoofer diaphragm with a 4-inch aluminum platform mounted at the center; (b) schematic view of plates mounted on the vibrating aluminum platform, where parts tumble randomly until falling into apertures.

for the step-edge parts.

#### 5.5.1 Positioning with One-to-one Registration

Bulk parts were distributed by vibration into an array of apertures. The experimental setup is shown in Figure 5.8. The vibrating stage was a 4-inch aluminum plate glued to the center of the diaphragm of a Samson resolv 120a active subwoofer (Samson Technologies Corp., NY), and the subwoofer was driven by AC voltage signals from a function generator. The plates with 1000 apertures were mounted on the aluminum stage. When the vibrating stage was turned on, a paper funnel carrying about 3000 bulk parts was scanned across the aperture plate to dispense parts, thus parts were uniformly fed. On the vibrating aperture plate, parts tumbled randomly until falling into the apertures. Due to geometric constraints shown in Figure 5.9, one aperture adopted exactly one part, and the part stood vertically with a  $790\mu\text{m} \times 330\mu\text{m}$  footprint. The vibration amplitude was controlled to be less than  $500\mu\text{m}$  so that the trapped parts stayed in place and other free parts kept tumbling randomly until being trapped: the frequency and peak-to-peak amplitude of the sinusoidal driving voltage were respectively 50Hz and 120mV, and the volume of the subwoofer was set at level 5. Finally, redundant parts were easily wiped off since trapped parts made

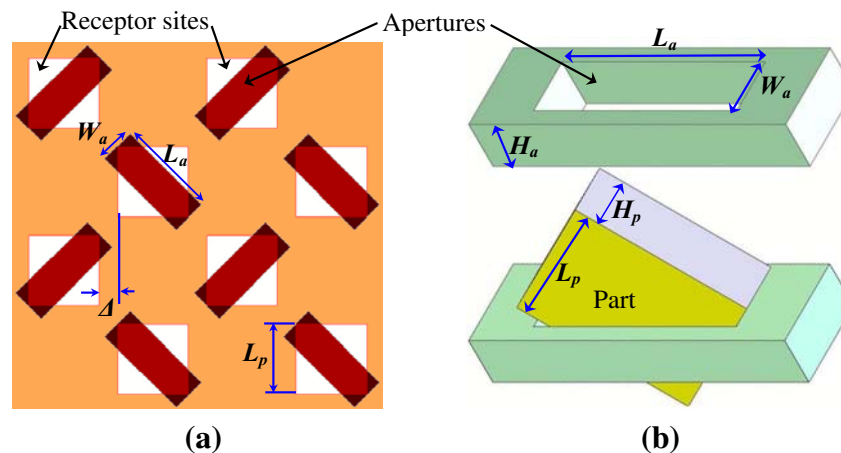


Figure 5.9: Schematic design rule for parts, apertures and receptor sites: (a) a partial view of the overlapped layouts of the aperture plate and the palletizing plate; (b) a diagonally wedged part can be avoided when the aperture length  $L_a$  is greater than the diagonal of the part  $L_p$ . We use:  $L_p = 790\mu\text{m}$ ,  $H_p = 330\mu\text{m}$ ,  $L_a = 1130\mu\text{m}$ ,  $W_a = 400\mu\text{m}$ ,  $H_a = 330\mu\text{m}$ ,  $\Delta = 210\mu\text{m}$  and the height of spacer I (Figure 5.1a)  $H_s = 460\mu\text{m}$ , such that  $H_s + H_a = L_p$ .

a flat surface on the aperture plate. We ran the trapping experiment 6 times with 3000 bulk parts, and observed yields ranging from 98.5% to 99.8% in about 2 minutes (Figure 5.10).

### 5.5.2 Palletizing

Trapped parts were then transferred to a glass palletizing plate via temporary bonding by capillary forces. The palletizing plate had an array of hydrophilic receptor sites and hydrophobic thiolated gold background. A dip coating process left water droplets on the receptor sites (Figure 5.11a and Figure 5.12a). The part transfer process is schematically shown in Figure 5.1b-d. The palletizing plate was placed on top of the aperture plate with two  $150\mu\text{m}$  thick spacers between them, and two plates were roughly aligned with  $\sim 200\mu\text{m}$  tolerance for each water droplet to oppose a part directly. These spacers prevented water droplets from contacting the hydrophilic

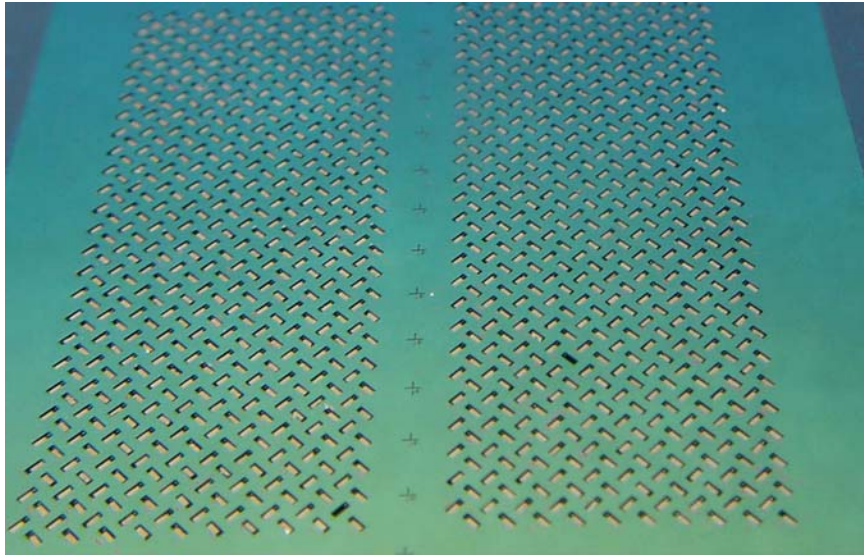
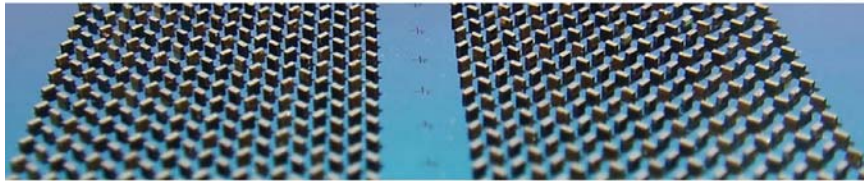
**(a)****(b)**

Figure 5.10: Optical images of  $790\mu\text{m}$  square parts falling into apertures vertically: (a) an aperture plate with 1000 apertures, two apertures are empty (yield = 99.8%); (b) parts protruding out of the aperture plate when the spacers (Figure 5.1a) were removed.

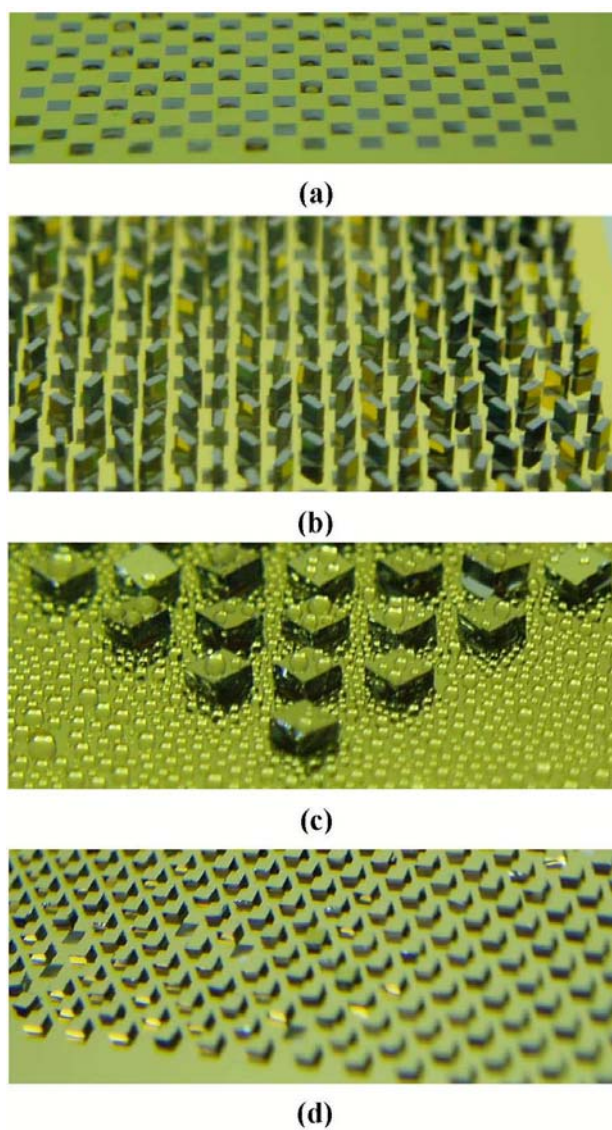
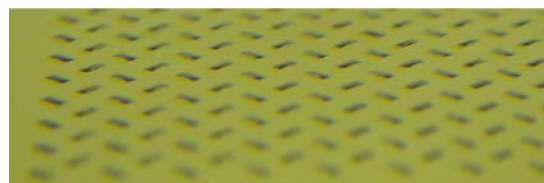
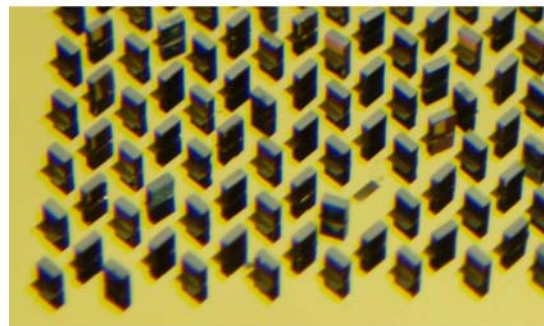


Figure 5.11: Optical images of  $790\mu\text{m}$  square parts transferred to a palletizing pyrex plate via water droplets: (a) a partial view of an array of  $790\mu\text{m}$  square hydrophilic receptor sites covered with water droplets; (b) parts were transferred to stand vertically (see Figure 5.1d); (c) water steam condensation was introduced on the palletizing plate, where steam formed film-wise and droplet-wise condensation respectively on hydrophilic and hydrophobic areas; (d) parts attached to receptor sites horizontally after steam condensation, with their only hydrophobic Au surface facing outward.



(a)



(b)

Figure 5.12: Optical images of vertically mounted  $790\mu\text{m}$  square parts: (a) droplets wetted only receptor sites with same dimension as the flat edge of parts; (b) parts vertically attached.

aperture plate and parts, which must be avoided because water can cause parts to be stuck in the apertures by capillary forces (significantly greater than gravity of the  $790\mu\text{m}$  square part). When the stack of plates was flipped over, parts slid down and stood vertically on the receptor sites (Figure 5.11b and Figure 5.12b), i.e. parts have been vertically assembled.

### 5.5.3 *Wet Horizontal Mounting with Unique Face Orientations*

To assemble parts horizontally with  $790\mu\text{m}\times 790\mu\text{m}$  footprints, we introduced water steam to condense on the surfaces (droplet-wise and film-wise condensation respectively on hydrophobic and hydrophilic surfaces, see Figure 5.11c), thus the receptor sites gained more water. Since water condensate favored the hydrophilic oxide face of each part and the hydrophilic receptor sites, water wetting lines on the hydrophilic part faces were higher than those on the hydrophobic part faces. This height difference brought about a capillary torque on each part. The longer the steam condensation time, the greater the height difference and the greater the capillary torque. When the capillary torques were greater than reversely directed gravitational torques on parts, net torques drove parts to rotate to face the receptor sites with their hydrophilic oxide faces (Figure 5.11d). A slight agitation on the palletizing plate caused parts to rotate with less water condensate because vibration brought about additional torques to overcome gravitational torques. Finally excess water was evaporated by heating at about  $70^\circ\text{C}$  and parts self-aligned with high precision to minimize interfacial energies. The less water remained underneath the parts, the more accurate the alignment became.

### 5.5.4 *Permanent Bonding*

Finally parts were permanently bonded to a glass bonding plate with patterned AZ4620 squares (Figure 5.13a). When the bonding plate was in contact and aligned with the palletizing plate, parts were bonded by reflowed AZ4620. High surface

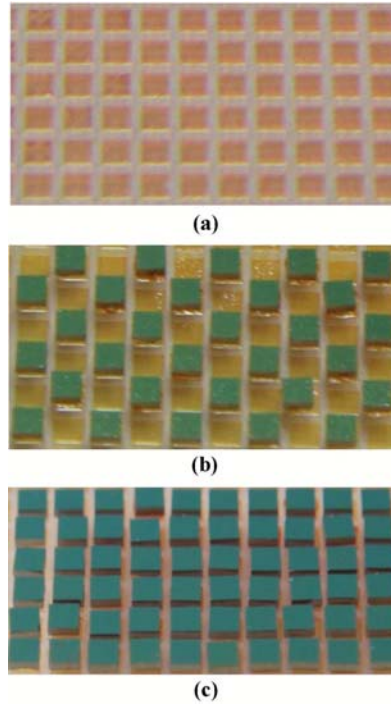


Figure 5.13: Permanent bonding of  $790\mu\text{m}$  square parts: (a) an array of bonding sites covered with photoresist AZ4620; (b) parts bonded by the reflowed AZ4620 after one batch transfer (Figure 5.1f); (c) parts bonded by reflowed AZ4620 after 2<sup>nd</sup> batch transfer.

coverage ratio of  $\frac{1}{2}L_P^2/(L_P + \Delta)^2 = 31\%$  was achieved by a single batch transfer (Figure 5.13b). By using the same plates (aperture, palletizing and bonding plates), and offsetting the alignment between the palletizing plate and the bonding plate by a row or column ( $L_P + \Delta$ ), a 2<sup>nd</sup> batch transfer increased this ratio to 62% (Figure 5.13c). Melting solder is another option for the permanent mechanical bonding together with electrical connections (Figure 5.14), and we demonstrated this with low melting point solder (LMA-117 with a melting point of  $\sim 47^\circ\text{C}$ ; Small Parts, FL).



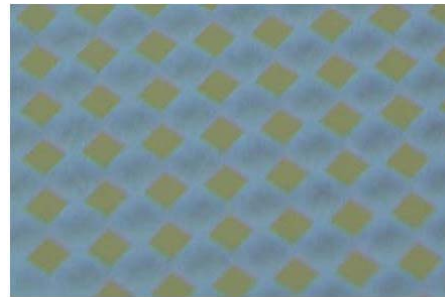
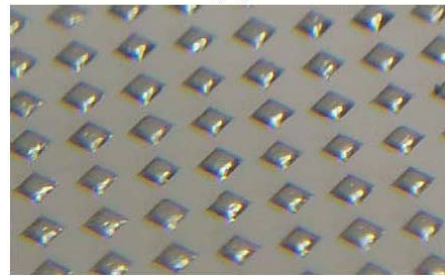
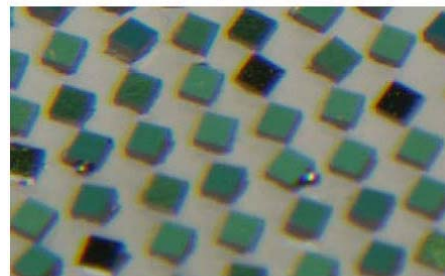
**(a)****(b)****(c)**

Figure 5.14: Optical images of parts bonded with melting solder: (a) an array of  $790\mu\text{m}$  square Au bonding sites on a glass substrate; (b) melting solder left on the Au bonding sites by a dip coating process; (c) parts bonded by the solder.

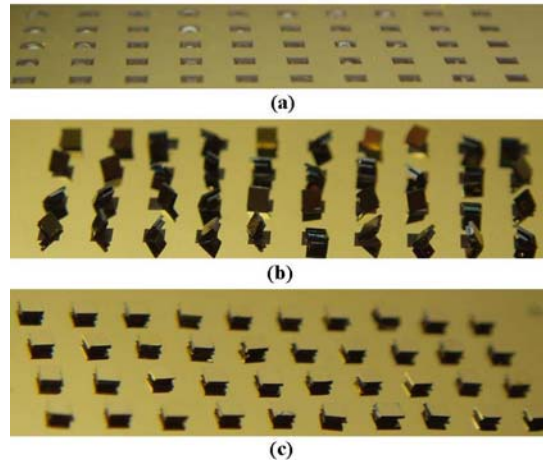


Figure 5.15: Optical images of horizontal mounting of  $790\mu\text{m}$  square step-edge parts: (a) droplets wetting only hydrophilic receptor sites; (b) parts were attached to receptor sites via droplets and stayed tilted due to their step edges; (c) titled parts were laid down on their oxide faces by pressing.

#### 5.5.5 Dry Horizontal Mounting with Unique Face Orientations

Steam environment should be avoided for micro-components with exposed microstructures such as cantilever beams because water residue can immobilize or even damage such fragile structures due to its surface tension force. To avoid the wet face-orienting by steam condensation in Section 5.5.3, we demonstrated a dry face-orienting process with the  $790\mu\text{m}$  square step-edge parts (Figure 5.15): (1) the parts were attached to droplets on the receptor sites by the same method as that for the flat-edge parts and they stayed titled due to their step edges (detailed discussion in Section 5.4.2); (2) a pressing plate laid down all the parts (the pressing plate was introduced approximately parallel to the palletizing substrate); (3) all parts self-aligned with the receptor sites to achieve interfacial energy minimization.

## 5.6 *Discussions*

### 5.6.1 *Part Feeding into Apertures*

Successful feeding of parts into apertures required proper vibrating of the aperture plate. Provided a constant driving voltage, the vibrating amplitude of the subwoofer diaphragm changed with the driving frequency: we ran the vibrating stage at 50Hz to achieve proper capturing of parts; lower frequencies such as 30Hz and 20Hz could vibrate the captured parts out of apertures; at higher frequencies, parts kept horizontal poses due to smaller vibrating amplitude and therefore had no chances to slide into the narrow apertures. Literature [SBK95] also reported several vibrating strategies to orient agitated parts including vertical standing.

Vibratory part feeding requires protection for fragile structures on microelectromechanical components to avoid sliding (possibly devastating) contact with apertures. Such protection can be provided by a solid frame around these fragile structures, e.g. microstructures constructed by bulk silicon etching processes.

### 5.6.2 *Surface Hydrophobicity or Hydrophilicity*

In the above demonstrated assembly process, both the palletizing and wet face-orienting steps require significant contrast of water wettability for different surface areas and different part faces. Especially for the wet face-orienting step to lay down vertically standing parts, the greater wettability contrast between the hydrophobic and hydrophilic part faces, the easier to accomplish this process step. Literature [KSK<sup>+</sup>97] showed that water contact angles on a silicon oxide surface increased with time, ranging from 5° to 75°, which indicates silicon parts with fresh silicon oxide are favorable for our demonstrated assembly process.

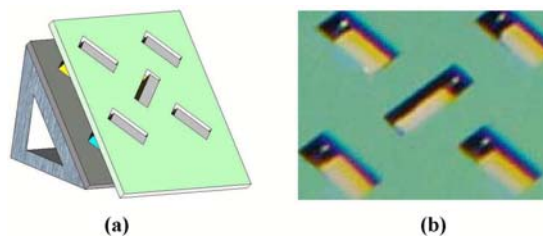


Figure 5.16: Fine alignment for vertically standing parts by gravity: (a) schematic experiment setup; (b) an optical image of well aligned parts in the apertures.

### 5.6.3 Fine Alignment for Vertically Standing Parts

In case that vertically standing parts are transferred to receptor sites without droplets, i.e., no capillary forces drive the final high precision alignment, gravity driven fine alignment can be used before the transfer (Figure 5.16): when the aperture plate is tilted and slightly agitated, all the trapped parts reach their lowest accessible heights inside their aperture by minimizing potential energies. After the spacers are removed, parts are protruding as shown in Figure 5.10b and ready for transfer.

### 5.6.4 Different Types of Liquid Droplets on Receptor Sites

The evaporation rate of a liquid droplet, defined as lost volume per unit time ( $dV/dt$ ), is approximately proportional to the exposed surface area  $S$ , which can be expressed with the following equation.

$$\frac{dV}{dt} = k_1 S \quad (5.18)$$

where  $k_1$  is a constant. For a droplet with a circular base (radius =  $r$ ) on a substrate, its exposed surface area  $S$  and volume  $V$  are respectively proportional to  $r^2$  and  $r^3$ . Therefore, Equation (5.18) can be rewritten as:

$$\frac{dV}{dt} = k_2 V^{2/3} \quad (5.19)$$

or

$$dt = k_2^{-1}V^{-2/3}dV \quad (5.20)$$

By integrating both sides of Equation (5.20), we can obtain the total time  $T$  to evaporate a whole droplet with initial volume  $V_0$  and base radius  $r_0$ :

$$T = 3k_2^{-1}V_0^{1/3} = k_3r_0 \quad (5.21)$$

where  $k_2$  and  $k_3$  are constants. Equation (5.21) indicates a proportional relationship between total evaporation time  $T$  and initial base radius  $r_0$  of the droplet. We observed that a water droplet on a  $790\mu\text{m}$  square glass receptor site disappeared in about 2 minutes under a normal lab environment and at room temperature. Air temperature and humidity also affect evaporation with warm, dry air increasing evaporation and cold moist air decreasing the rate. For smaller parts, humidity and air temperature should be well controlled to achieve the complete assembly process.

Without requiring good control of humidity or air temperature, involatile liquid can be used for assembly of the step-edge parts. According to Equation (5.12) and 5.15, the ratio of capillary torques in Equation (5.17), the only determinant factor for a step-edge part to stand in a leaning pose, is independent of the surface tension of the liquid droplet. An acrylate-based liquid was tested for transferring of step-edge parts to a palletizing plate, and all the parts stayed leaning after attaching to the receptor sites. Finally, they were laid down by a pressing plate to be horizontally assembled.

## 5.7 Conclusions

We have demonstrated a parallel micro-assembly process based on both shape recognition and capillary-driven self-assembly in an air environment, which assembled parts in a vertical or horizontal mode to densely packed receptor sites with a defect rate of

~1%. The vertical mode is useful, e.g., for edge-emitting or vertical cavity surface-emitting laser (VCSEL) components, laser beam routing, or RF MEMS components. The horizontal mode can be applied to assembly of LED displays, RFID chips, and other types of flat micro-components. Additionally, the multi-batch assembly capability of this assembly process enables packaging single or multiple types of micro-components with high surface coverage ratios on a single substrate.

## Chapter 6

# CONCLUSION

### **6.1 Results Summary**

Aiming for rapid and massively parallel packaging of micro-scale device components, we have focused our research on developing and optimizing self-assembly techniques to satisfy different manufacturing requirements of various types of micro-components.

Chapter 3 introduces a capillary-driven self-organizing parallel assembly (C-SPASS) process which proceeds in an air environment. This assembly process relies on interfacial energy minimization to achieve highly accurate placement of flat micro-components onto an array of hydrophilic receptor sites on a hydrophobic substrate: a simple dip coating process can leave liquid droplets only on hydrophilic receptor sites, and micro-components self align to the receptor sites, the minimum interfacial energy state, as soon as they contact the droplets. The alignment time depends on several factors such as surface tension of the liquid, mass of the component, translational and rotation offsets from the aligned state. For a millimeter or sub-millimeter scale flat component, the capillary alignment is usually a sub-second process. The C-SPASS process was demonstrated with assembly of PZT actuators for diffuser valve micro fluidic pumps (an acrylate-based adhesive was used to establish permanent bonding when it was heated), and showed many advantages over conventional mounting methods using highly viscous silver epoxy: (1) a parallel assembly process; (2) much higher alignment accuracy; (3) controlled adhesive thickness; (4) PZT actuators assembled flat on top of pump diaphragms; (5) lower process temperature (80°C *vs.* 200°C); (6) much higher process repeatability.

Chapter 4 presents a semi dry uniquely orienting self-organizing parallel assembly (semi DUO-SPASS) process and a DUO-SPASS process. Both assembly processes can achieve unique face and in-plane orientations of flat micro-components with arbitrary shapes. **The semi DUO-SPASS process** is designed for flat micro-components having a circular peg located offset from the center of mass on one face and a unique hydrophobic face opposite to the peg face, and it contains two wet steps followed by two dry steps: (1) bulk parts are uniquely face-oriented on an agitated water surface where they can only float with their unique hydrophobic faces in the air; (2) floating parts are picked up by a hydrophobic carrier wafer (parts attach to the carrier wafer by their flat hydrophobic faces) and transferred to an alignment template patterned with an array of receptor sites having a circular holes, and the pegs touch the alignment template; (3) parts are driven to move by centrifugal forces from orbital shaking, and then anchored to receptor sites as their pegs fall into holes; (4) the alignment template is tilted in a certain orientation so that redundant parts slide away from the alignment template and anchored parts self-align with receptor sites by rotating about their pegs to minimize their potential energies. An optional capillary-driven alignment step can greatly reduce misalignment of the dry alignment by gravitational forces: steam is introduced to condense on the exposed surfaces, and then water condensate enters the gaps underneath parts so that the part/template interfaces are lubricated and parts self-align to the patterned hydrophilic receptor sites with higher accuracy due to interfacial energy minimization. The semi DUO-SPASS process was demonstrated with assembly of 2mm square dummy silicon parts on an alignment template having 168 receptor sites, and an assembly yield of  $\sim 99\%$  was achieved within around 5 minutes. **The DUO-SPASS process** is mainly based on two-stage shape recognition: two types of pegs on each part respectively and subsequently mate with two types of recessed features on each receptor site. One peg is of a cross shape (called XP), and the other one is circular (called CP) and higher than XP. The dry assembly process is achieved with the following steps: (1) bulk parts are agitated by orbital shaking on a



flat substrate, and they tend to rest on their flat faces to gain higher motion stability, i.e., their pegs point upwards and they are uniquely face-oriented; (2) these parts are transferred to an alignment template having an array of receptor sites by a method similar to flipping over a sandwich, and pegs touch the template; (3) centrifugal forces, from orbital shaking with a lower shaking speed than step 1, drive the parts to move randomly without flipping until they are anchored by their taller CPs' falling into circular holes, i.e., 1<sup>st</sup> shape recognition is completed; (4) centrifugal forces introduce torques on the anchored parts (the CP is located offset from the center of mass) to rotate them until their XPs fit into the cross trenches, and thus 2<sup>nd</sup> shape recognition is accomplished. The alignment accuracy is determined by the clearance between a XP and its counterpart cross trench. The DUO-SPASS process was demonstrated with assembly of 1mm square dummy silicon parts and assembly yields of  $\sim 98\%$  were achieved on two alignment templates respectively having 391 and 720 receptor sites. The alignment accuracy is  $20\mu\text{m}$ . Due to its dry nature, the DUO-SPASS process will not introduce sticking effects for MEMS components having flexible microstructures as a wet assembly process will.

Chapter 5 describes a vertical/horizontal self-organizing parallel assembly (VH-SPASS) process. This assembly process, based on shape recognition and capillary forces, is achieved with the following steps: (1) agitated bulk parts fall into apertures in a flat substrate, and each aperture traps exactly one vertically standing part due to the geometrical constraints; (2) trapped parts are transferred onto water covered hydrophilic receptor sites due to capillary forces, and parts keep their standing poses, i.e., parts are vertically assembled; (3) parts are laid down by adding more water to exposed surfaces through steam condensation (two large vertical faces are respectively hydrophilic and hydrophobic), because hydrophilic surfaces gain more water than hydrophobic surfaces, and such a difference introduce an extra capillary torque on a standing part. The process was demonstrated with assembly of  $790\mu\text{m}$  square silicon parts, and assembly results showed  $\sim 1\%$  defect rates for 1000 receptor sites on a 4''

substrate.

## **6.2 Research Outlook**

Self-assembly techniques enable rapid and parallel construction processes for MEMS devices. With appropriate driving forces, self-assembly techniques can assemble components ranging from sub-microns to millimeters or larger scales, while conventional robotic pick-and-place assembly methods can only handle components larger than about  $500\mu\text{m}$  due to sticking effects between grippers and components. The following research directions are worthy of efforts to further extend the capabilities of self-assembly techniques.

Three-dimensional self-assembly methods will most likely play a key role in building MEMS devices with more complicated architectures. Most of the currently available self-assembly techniques mount micro-components on a substrate surface, i.e., a 2-dimensional assembly process. To achieve multiple functions or stand-alone applications, a MEMS device can be integrated with a variety of components such as MEMS sensing units, MEMS actuating units, or CMOS signal processing units. Three-dimensional assembly enables dense packaging of these components, which can greatly reduce environmental disturbances and signal transmission losses among different functional units.

Assembly programmability will greatly widen the application range of self-assembly techniques and enable construction of more versatile MEMS devices. This programmability can indicate several situations such as: (1) integration of different types of components by multiple batches of self-assembly; (2) self-assembly of same types of components into various patterns in different batches; (3) selective disassembly of some components by breaking up their bonds to receptor sites; (4) assembly of multiple components in appropriate sequences to form three-dimensional structures.

Assembly process automation enables running the self-assembly process contin-

uously to improve assembly throughput. To automate a self-assembly system, one needs to take the following factors into account: parts feeding, parts sorting, redundant parts recycling, assembly defect recognition and remedy.

## BIBLIOGRAPHY

- [Adl94] L. Adleman. Molecular computation of solutions to combinatorial problems. *Science*, 266:1021–1024, 1994.
- [Asa00] H. Asakura. First wafer-scale packages show up in commercial products. *Solid State Technology*, 43(10):39, 2000.
- [BB03] L. Balan and G.M. Bone. Automated gripper jaw design and grasp planning for sets of 3d objects. *Journal of Robotic Systems*, 20(3):147–162, 2003.
- [BBA98] R.L. Bayt, K.S. Breuer, and A.A. Ayon. Drie-fabricated nozzles for generating supersonic flows in micropropulsion systems. In *Proceedings of Solid State Sensor, Actuator, and Microsystems Workshop*, Hilton Head Island, SC, 1998.
- [BDKL00] Böhringer, B. R. Donald, L. E. Kavraki, and F. Lamiraux. Part orientation with one or two stable equilibria using programmable force fields. *IEEE Transactions on Robotics and Automation*, 16(2):157–170, 2000.
- [BDM99] K.F. Böhringer, B. R. Donald, and N. C. MacDonald. Programmable vector fields for distributed manipulation, with applications to mems actuator arrays and vibratory parts feeders. *International Journal of Robotics Research*, 18(2):168–200, 1999.
- [BGC<sup>+</sup>98] K.F. Böhringer, K. Goldberg, M. Cohn, R. T. Howe, and A. Pisano. Parallel microassembly with electrostatic force fields. In *Proc. International Conference on Robotics and Automation*, Leuven, Belgium, 1998.
- [BHJ04] C.R. Barry, C.J. Hoon, and H.O. Jacobs. Approaching programmable self-assembly from nanoparticle-based devices to integrated circuits. *Proceedings of the Foundations of Nanoscience*, 2004.
- [BPM82] G. Boothroyd, C. Poli, and L. Murch, editors. *Automatic Assembly*. Marcel Dekker, INC., 1982.

- [BPT00] S. Balakrishnan, N. Popplewell, and M. Thomlinson. Intelligent robotic assembly. *Computers and Industrial Engineering*, 38(4):467–478, 2000.
- [BSH01] K.F. Böhringer, U. Srinivasan, and R.T. Howe. Modeling of fluidic forces and binding sites for fluidic self-assembly. In *Proceedings of IEEE International Conference on Micro Electromechanical Systems*, Interlaken, Switzerland, 2001.
- [BZB98] R. Boudreau, P. Zhou, and T. Bowen. Wafer scale photonic-die attachment. *IEEE Transactions on Components Packaging and Manufacturing Technology Part B-Advanced Packaging*, 21(2):136–139, 1998.
- [CBN+98] M.B. Cohn, K.F. Böhringer, J.M. Noworolski, A. Singh, C.G. Keller, K.Y. Goldberg, and R.T. Howe. Microassembly technologies for mems. In *Proc. SPIE Micromachining and Microfabrication*, pages 2–16, Santa Clara, CA, 1998.
- [CGO+02] J. Chen, K. Goldberg, M.H. Overmars, D. Halperin, K.F. Böhringer, and Y. Zhuang. Computing tolerance parameters for fixturing and feeding. *Assembly Automation*, 22(2):163–172, 2002.
- [CHP95] M.B. Cohn, R.T. Howe, and A.P. Pisano. Self-assembly of microsystems using non-contact electrostatic traps. In *Proceedings of the ASME International Congress and Exposition, Symposium on Micromechanical Systems*, pages 893–900, San Francisco, CA, 1995.
- [CKK01] Y.S. Choi, D.K. Kim, and Y.S. Kwon. New technology for dna chips on a microarray - random fluidic self-assembly method using hydrophobic interaction. *Molecular Crystals And Liquid Crystals*, 370:363–366, 2001.
- [CLHP96] M.B. Cohn, Y.C. Liang, R.T. Howe, and A.P. Pisano. Wafer-to-wafer transfer of microstructures for vacuum packaging. In *Proceedings of Solid-state Sensor and Actuator Workshop*, Hilton Head Island, SC, 1996.
- [Coh97] M.B. Cohn. *Assembly Techniques for Microelectromechanical Systems*. PhD thesis, University of California: Berkeley, 1997.
- [CP97] M.D.B. Charlton and G.J. Parker. Fabrication of high aspect ratio silicon microstructures by anodic etching. *Journal of Micromechanics and Microengineering*, 7:155–158, 1997.

- [dG95] P. G. de Gennes. Wetting: Statics and dynamics. *Reviews of Modern Physics*, 57(3):827–863, 1995.
- [ER01] N.F. Edmondson and A. H. Redford. Flexible parts feeding for flexible assembly. *International Journal of Production Research*, 39(11):2279–2294, 2001.
- [EVK01] K. P. Ellis, F. J. Vittes, and J. E. Kobza. Optimizing the performance of a surface mount placement machine. *IEEE Trans. Electron. Packag. Manufact.*, 24:160–170, 2001.
- [FB05a] J. Fang and K.F. Böhringer. High yield batch packaging of micro devices with uniquely orienting self-assembly. In *Proceedings of IEEE International Conference on Micro Electro Mechanical Systems*, Miami Beach, FL, 2005.
- [FB05b] J. Fang and K.F. Böhringer. Uniquely orienting dry micro assembly by two-stage shape recognition. In *Proceedings of The 13th International Conference on Solid-State Sensors and Actuators*, Seoul, Korea, 2005.
- [FB06a] J. Fang and K. F. Böhringer. Parallel micro component-to-substrate assembly with controlled poses and high surface coverage. *IOP Journal of Micromechanics and Microengineering*, 16(4):721–730, 2006.
- [FB06b] J. Fang and K. F. Böhringer. Wafer-level packaging based on uniquely orienting self-assembly (the duo-spasp processes). *ASME/IEEE Journal of Microelectromechanical Systems*, 15(3):531–540, 2006.
- [FBA<sup>+</sup>95] F.K. Forster, R.L. Bardell, M.A. Afromowitz, N.R. Sharma, and A. Blanchard. Design, fabrication and testing of fixed-valve micropumps. In *Proceedings of the ASME Fluids Engineering Division, ASME International Mechanical Engineering Congress and Exposition*, volume 234, pages 39–44, San Francisco, CA, 1995.
- [Fea95a] R.S. Fearing. A planar milli-robot on an air bearing. In *Proceedings of International Symposium of Robotics Research*, Heitsching, Germany, 1995.
- [Fea95b] R.S. Fearing. Survey of sticking effects for micro parts. In *Proceedings of IEEE International Conference of Robotics and Intelligent Systems*, Pittsburgh, PA, 1995.

- [ffi] <http://www.flipchips.com>.
- [FWB04] J. Fang, K. Wang, and K.F. Böhringer. Self-assembly of micro pumps with high uniformity in performance. In *Proceedings of Solid State Sensor, Actuator, and Microsystems Workshop*, Hilton Head Island, SC, 2004.
- [FWB06] J. Fang, K. Wang, and K. F. Böhringer. Self-assembly of pzt actuators for micro pumps with high process repeatability. *ASME/IEEE Journal of Microelectromechanical Systems*, 15(4), 2006.
- [Gar00] P. Garrou. Contributions from tc-18 wafer scale packaging - foreword. *IEEE Transactions On Advanced Packaging*, 23(2):197–197, 2000.
- [GJOB02] J. Geske, V. Jayaraman, Y.L. Okuno, and J.E. Bowers. Vertical and lateral heterogeneous integration using direct wafer bonding. *Compound Semiconductors 2001 Institute Of Physics Conference Series*, 170:289–293, 2002.
- [GLK<sup>+</sup>02] A. Greiner, J. Lienemann, J.G. Korvink, X. Xiong, Y. Hanein, and K.F. Böhringer. Capillary forces in micro-fluidic self-assembly. In *Proceedings of 5th International Conference on Modeling and Simulation of Microsystems*, pages 198–201, 2002.
- [Goo69] L.S. Goodman. Geometric optimization of controlled collapse interconnections. *IBM J. Res. Dev.*, 13:251–265, 1969.
- [GS86] B. Grünbaum and G. C. Shephard. *Tilings and Patterns*. New York: Freeman, 1986.
- [GTB<sup>+</sup>00] D.H. Gracias, J. Tien, T.L. Breen, C. Hsu, and G.M. Whitesides. Forming electrical networks in three dimensions by self-assembly. *Science*, 289:1170–1172, 2000.
- [HAE<sup>+</sup>01] G. Hotchkiss, G. Amador, D. Edwards, P. Hundt, L. Stark, R. Stierman, and G. Heinen. Wafer level packaging of a tape flip-chip chip scale packages. *Microelectronics Reliability*, 41(5):705–713, 2001.
- [HBL99] K.F. Harsh, V.M. Bright, and Y.C. Lee. Solder self-assembly for three-dimensional microelectromechanical systems. *Sensors and Actuators A: Physical*, 77(3):237–244, 1999.

- [HDWL01] Y. Huang, X. Duan, Q. Wei, and C.M. Lieber. Directed assembly of one-dimensional nanostructures into functional networks. *Science*, 291:630–633, 2001.
- [HGA<sup>+</sup>03] T.T. Huang, T. Geng, D. Akin, W.J. Chang, J. Sturgis, R. Bashir, A.K. Bhunia, J.P. Robinson, and M.R. Ladisch. Micro-assembly of functionalized particulate monolayer on c18-derivatized sio2 surfaces. *Biotechnology and Bioengineering*, 83(4):416–427, 2003.
- [HHF<sup>+</sup>02] S. Hayamizu, K. Higashino, Y. Fujii, Y. Sando, and K. Yamamoto. New bi-directional valveless silicon micropump controlled by driving waveform. In *Proceedings of IEEE Conference on Micro Electromechanical Systems*, pages 113–116, 2002.
- [HIL98] K.F. Harsh, R.S. Irwin, and Y.C. Lee. Solder self-assembly for mems. In *Proceedings of 4th International Instrumentation Symposium*, pages 256–261, Reno, NV, 1998.
- [Hit88] H. Hitakawa. Advanced parts orientation system has wide application. *Assembly Automation*, 8, 1988.
- [HKZ<sup>+</sup>00] K. F. Harsh, P. E. Kladitis, Y. H. Zhang, M. L. Dunn, V. M. Bright, and Y. C. Lee. Tolerance and precision study for solder self-assembled mems. *Proc. SPIE*, 4075:173–184, 2000.
- [HMB97] M. Heschel, M. Muellenborn, and S. Bouwstra. Fabrication and characterization of truly 3-d diffuser/nozzle microstructures in silicon. *IEEE Journal of Microelectromechanical Systems*, 6(1):41–47, 1997.
- [HS98] A.S. Holmes and S.M. Saidam. Sacrificial layer process with laser-driven release for batch assembly operations. *IEEE Journal of Microelectromechanical Systems*, 7(4):416–422, 1998.
- [HSM94] K. Hosokawa, I. Shimoyama, and H. Miura. Dynamics of self-assembling systems - analogy with chemical kinetics. *Artificial Life*, 1:413–427, 1994.
- [HZBL99] K.F. Harsh, W. Zhang, V.M. Bright, and Y.C. Lee. Flip-chip assembly for si-based rf mems. In *Proceedings of IEEE International Conference of Micro Electromechanical Systems*, pages 273–278, 1999.
- [IS05] E. Iwase and I. Shimoyama. Multi-step sequential batch self-assembly of three-dimensional micro-structures using magnetic field. In *Proceedings*



- of *IEEE International Conference on Micro Electromechanical Systems*, Miami, FL, 2005.
- [JH04] S. Jensen and O. Hansen. Characterization of the microlading effect in deep reactive ion etching of silicon. In *Proceedings of SPIE International Symposium on Micromachining and Microfabrication*, volume 5342, pages 111–118, San Jose, CA, 2004.
- [Jia02] S. Jiang. Molecular simulation studies of self-assembled monolayers of alkanethiols on au(111). *Molecular Physics*, 100(14):2261–2275, 2002.
- [JMH02] L.S. Jang, D.R. Meldrum, and M.R. Holl. An active mixer for microscale dna purification and sequencing reaction clean-up. In *Proceedings of 6th International Conference on Miniaturized Chemical and Biochemical Analysis Systems*, pages 239–241, Nara, Japan, 2002.
- [JTS<sup>+</sup>02] H.O. Jacobs, A.R. Tao, A. Schwartz, D.H. Gracias, and G.M. Whitesides. Fabrication of cylindrical display by patterned assembly. *Science*, 296:323–325, 2002.
- [KB00] P.E. Kladitis and V.M. Bright. Prototype microrobots for micro-positioning and micro-unmanned vehicles. *Sens. Actuators*, A80:132–137, 2000.
- [KBdR03] A. Kuoni, M. Boillat, and N.F. de Rooij. A modular high density multi-channel dispenser for micro-array printing. In *Proceedings of International Conference of Solid-State Sensors, Actuators and Microsystems*, pages 372–375, 2003.
- [KBNG97] I. Kashkoush, E. Brause, R. Novak, and R. Grant. In situ chemical concentration control for wafer wet cleaning. In *Proceedings of Materials Research Society Symposium*, volume 477, pages 311–316, 1997.
- [KC00] J.Y. Kim and H.S. Cho. A neural net-based assembly algorithm for flexible parts assembly. *Journal of Intelligent and Robotic Systems*, 29(2):133–160, 2000.
- [KCBG99] I. Kashkoush, G. Chen, P. Boelen, and M. Geomini. Hf concentration control in ic manufacturing. In *the 6th International Symposium on Cleaning Technology in Semiconductor Device Manufacturing*, Honolulu, Hawaii, 1999.

- [KF04] S.A. Kulinich and M. Farzaneh. Alkylsilane self-assembled monolayers: Modeling their wetting characteristics. *Applied Surface Science*, 230:232–240, 2004.
- [Kim00] M. Kimura. Wafer-scale packaging will become a low-cost alternative by 2003. *Solid State Technology*, 43(7):67–68, 2000.
- [KL01] V. Kaajakari and A. Lal. Electrostatic batch assembly of surface mems using ultrasonic triboelectricity. In *Proceedings of IEEE International Conference on Micro Electromechanical Systems*, pages 10–13, 2001.
- [Kla] E. Klavins. Directed self-assembly using graph grammars. In *Proceedings of Foundations of Nano Science Conference*, Snowbird, UT.
- [KLS<sup>+</sup>99] H. Kurino, K.W. Lee, K. Sakuma, T. Nakamura, and M. Koyanagi. A new wafer scale chip-on-chip (w-coc) packaging technology using adhesive injection method. *Japanese Journal Of Applied Physics Part 1-Regular Papers Short Notes and Review Papers*, 38(4B):2406–2410, 1999.
- [Kov98] G. Kovacs. *Micromachined Transducers Sourcebook*. The McGraw-Hill Companies, New York, 1998.
- [KPL<sup>+</sup>02] K. Kim, S. Park, J.B. Lee, H. Manohara, Y. Desta, M. Murphy, and C.H. Ahn. Rapid replication of polymeric and metallic high aspect ratio microstructures using pdms and liga technology. *Microsystem Tech.*, 9:5–10, 2002.
- [KSK<sup>+</sup>97] S.D. Kim, C.S. Shin, N.J. Kwak, K.B. Lee, O.J. Kwon, and C.T. Kim. Effects of the underlayer surface state on the interconnecting aluminum film properties. In *Proceedings of the Materials Research Society Spring'97 Meeting*, San Francisco, CA, 1997.
- [LB03] S.W. Lee and R. Bashir. Dielectrophoresis and electrohydrodynamics-mediated fluidic assembly of silicon resistors. *Applied Physics Letters*, 83(18):3833–3835, 2003.
- [LGK<sup>+</sup>03] J. Lienemann, A. Greiner, J.G. Korvink, X. Xiong, Y. Hanein, and K.F. Böhringer. Modelling, simulation and experimentation of a promising new packaging technology - parallel fluidic self-assembly of micro devices. *Sensors Update*, 13(1):3–43, 2003.

- [LHL02] W. C. Lai, P. Hui, and J. Li. Non-contact batch micro-assembly by centrifugal force. In *Proceedings of International Conference of Micro Electromechanical Systems*, pages 184–187, Las Vegas, NV, 2002.
- [LN01] Y. Luo and B.J. Nelson. Fusing force and vision feedback for manipulating deformable objects. *Journal of Robotic Systems*, 18(3):103–117, 2001.
- [LWA<sup>+</sup>91] P.E. Laibinis, G.M. Whitesides, D.L. Allara, Y.T. Tao, A.N. Parikh, and R.G. Nuzzo. Comparison of the structures and wetting properties of self-assembled monolayer of n-alkanethiols on the coinage metal surfaces, cu, ag, au. *J. Am. Chem. Soc.*, 113:7152–7167, 1991.
- [LWB] S. Liang, K. Wang, and K.F. Böhringer. Self-assembly of mems components in air assisted by diaphragm agitation. In *Proceedings of IEEE Conference on Micro Electromechanical Systems*, Miami, FL.
- [LXB] S. Liang, X. Xiong, and K.F. Böhringer. Towards optimal designs for self-alignment in surface-tension driven micro-assembly. In *Proceedings of IEEE Conference on Micro Electromechanical Systems*, Maastricht, Holland.
- [Mad97] M.J. Madou. *Fundamentals of Microfabrication (2nd Edition)*. CRC Press LLC, Florida, 1997.
- [MDR<sup>+</sup>95] K.W. Marcus, V. Dhuler, D. Roberson, A. Cowen, M. Berry, and S. Nangalia. Smart mems: Flip chip integration of mems and electronics. In *Proceedings of SPIE Smart Materials Conference*, 1995.
- [MF03] C.J. Morris and F.K. Forster. Low-order modeling of resonance for fixed-valve micropumps based on first principles. *IEEE Journal of Microelectromechanical Systems*, 12(3):325–334, 2003.
- [mic] [http://www.aist.go.jp/MEL/soshiki/kyoku/bisho/ashida/study\\_e.html](http://www.aist.go.jp/MEL/soshiki/kyoku/bisho/ashida/study_e.html).
- [Mil69] L.F. Miller. Controlled collapse reflow chip joining. *IBM Journal of Research and Development*, 13:239–250, 1969.
- [MKZL94] T.S. McLaren, S.Y. Kang, W. Zhang, and Y.C. Lee. Thermosonic bonding for flip-chip assembly. *Adv. Microelectron.*, 21(4):14–16, 1994.

- [MZK<sup>+</sup>02] N. Miki, X. Zhang, R. Khanna, A. A. Ay, D. Ward, and S.M. Spearing. A study of multi-stack silicon-direct wafer bonding for mems manufacturing. In *Proceedings of IEEE Conference on Micro Electromechanical Systems*, pages 407–410, 2002.
- [OSS99] A. Olsson, G. Stemme, and E. Stemme. A numerical design study of the valveless diffuser pump using a lumpedmass model. *Journal of Micromechanics and Microengineering*, 9:34–44, 1999.
- [PCH04] C.T. Pan, C.H. Chien, and C.C. Hsieh. Technique of microball lens formation for efficient optical coupling. *Applied Optics*, 43:5939–5946, 2004.
- [PKPL04] D.S. Park, K. Kim, B. Pillans, and J.B. Lee. Polydimethylsiloxane-based pattern transfer process for the post-ic integration of mems onto cmos chips. *Journal of Micromechanics and Microengineering*, 14(3):335–340, 2004.
- [PRF02] J. Perkins, J. Rumpler, and C.G. Fonstad. Magnetically assisted self-assembly - a new heterogeneous integration technique. *MIT Microsystems Technology Laboratories Annual Report*, 2002.
- [Qia03] H. Qiao. Two- and three-dimensional part orientation by sensor-less grasping and pushing actions: Use of the concept of 'attractive region in environment'. *International Journal of Production Research*, 41(14):3159–3184, 2003.
- [RKW<sup>+</sup>01] M. Richter, J. Kruckow, J. Weidhaas, M. Wackerle, A. Drost, U. Schaber, M. Schwan, and K. Kühn. Batch fabrication of silicon micropumps. In *Proceedings of The 11th International Conference on Solid-State Sensors and Actuators*, Munich, German, 2001.
- [RLB02] E. Riedo, F. Ly, and H. Brune. Kinetics of capillary condensation in nanoscopic sliding friction. *Physical Review Letters*, 88(18):185505–(1–4), 2002.
- [RVN00] S.J. Ralis, B. Vikramaditya, and B.J. Nelson. Micropositioning of a weakly calibrated microassembly system using coarse-to-fine visual servoing strategies. *IEEE Transactions on Electronics Packaging Manufacturing*, 23(2):123–131, 2000.

- [SBCJ03] M.G. Steward, C.R. Barry, S.A. Campbell, and H.O. Jacobs. Nanoxerography: The use of electrostatic forces to pattern nanoparticles. In *Proceedings of the 2003 NSF Design, Service and Manufacturing Grantees and Research Conference*, 2003.
- [SBK95] P.J. Swanson, P.R. Burrige, and D.E. Koditschek. Global asymptotic stability of a passive juggling strategy: a possible parts feeding method. *Mathematical Problems in Engineering*, 3:193–224, 1995.
- [SCC02] E.J. Snyder, J. Chideme, and G.S.W. Craig. Fluidic self-assembly of semiconductor devices: A promising new method of mass-producing flexible circuitry. *Japanese Journal Of Applied Physics Part 1-Regular Papers Short Notes and Review Papers*, 41(6B):4366–4369, 2002.
- [SDB<sup>+</sup>99] J.W. Suh, R.B. Darling, K.F. Böhringer, B.R. Donald, H. Baltes, and G.T.A. Kovacs. Cmos integrated ciliary actuator array as a general-purpose micromanipulation tool for small objects. *Journal of Microelectromechanical Systems*, 8(4):483–496, 1999.
- [SEPL02] J. Seo, E. Ertekin, M.S. Pio, and L.P. Lee. Self-assembly templates by selective plasma surface modification of micropatterned photoresist. In *Proceedings of IEEE Conference on Micro Electromechanical Systems*, pages 192–195, 2002.
- [SF98] C.T. Su and H.P. Fu. A simulated annealing heuristic for robotics assembly using the dynamic pick-and-place model. *Prod. Planning and Control*, 9(8):795–802, 1998.
- [SHC<sup>+</sup>99] A. Singh, D.A. Horsley, M.B. Cohn, A.P. Pisano, and R.T. Howe. Batch transfer of microstructures using flip-chip solder bonding. *J. Microelectromechanical Systems*, 8(1):27–33, 1999.
- [SHH98] U. Srinivasan, M.R. Houston, and R.T. Howe. Alkyltrichlorosilane-based self-assembled monolayer films for stiction reduction in silicon micromachines. *Journal of Microelectromechanical Systems*, 7(2):252–260, 1998.
- [SHR<sup>+</sup>02] U. Srinivasan, M.H. Helmbrecht, C. Rembe, R.S. Muller, and R.T. Howe. Fluidic self-assembly of micromirrors onto microactuators using capillary forces. *Journal on Selected Topics in Quantum Electronics*, 8(1):4–11, 2002.

- [SHR03] K.L. Scott, R.T. Howe, and C.J. Radke. Model for micropart planarization in capillary-based microassembly. In *Proceedings of International Conference of Solid-State Sensors, Actuators and Microsystems*, pages 1319–1322, 2003.
- [SLH01] U. Srinivasan, D. Liepmann, and R.T. Howe. Microstructure to substrate self-assembly using capillary forces. *J. Microelectromechanical Systems*, 10(1):17–24, 2001.
- [SLW04] R.K. Smith, P.A. Lewis, and P.S. Weiss. Patterning self-assembled monolayers. *Progress in Surface Science*, 75(1-2):1–68, 2004.
- [SMAN03] D.R. Sparks, S. Massoud-Ansari, and N. Najafi. Chip-level vacuum packaging of micromachines using nanogetters. *IEEE Transactions on Advanced Packaging*, 26(3):277–282, 2003.
- [SP05] S. A. Stauth and B. A. Parviz. Self-assembled silicon networks on plastic. In *Proceedings of the 13th International Conference on Solid-State Sensors and Actuators*, Seoul, Korea, 2005.
- [SS99] S. Sorensen and R. Stringham. Feature vision guided flexible feeding made easy. *Industrial Robot*, 26(2):99–104, 1999.
- [SSFS00] J. Shinohara, M. Suda, K. Furuta, and T. Sakuhara. A high pressure-resistance micropump using active and normally-closed valves. 2000.
- [SUSE93] H. Sellers, A. Ulman, Y. Shnidman, and J.E. Eilers. Structure and binding of alkanethiolates on gold and silver surfaces: Implications for self-assembled monolayers. *J. Am. Chem. Soc.*, 115:9389–9401, 1993.
- [SY93] R.R.A. Syms and E.M. Yeatman. Self-assembly of fully three-dimensional microstructures using rotation by surface tension forces. *Electronics Letters*, 29:662–664, 1993.
- [SY98] J.S. Smith and J. Yeh. Method and apparatus for fabricating self-assembling microstructures. *U. S. Patent*, (5,824,186), 1998.
- [SYBW03] R.R.A. Syms, E.M. Yeatman, V.M. Bright, and G.M. Whitesides. Surface tension-powered self-assembly of microstructures - the state-of-the-art. *IEEE Journal of Microelectromechanical Systems*, 12(4):387–417, 2003.

- [SYHV99] J.S. Smith, J. Yeh, M.A. Hadley, and A.K. Verma. Apparatus for fabricating self-assembling microstructures. *U. S. Patent*, (5,904,545), 1999.
- [Sym99] R.R.A. Syms. Surface tension powered self-assembly of 3-d micro-optomechanical structures. *Journal of Microelectromechanical Systems*, 8(4):448–455, 1999.
- [SZE94] S.M. SZE. *Semiconductor Sensors*. John Wiley and Sons, Inc, New York, 1994.
- [TF01] J.A. Thompson and R.S. Fearing. Automating microassembly with orthotweezers and force sensing. In *Proc. IROS2001*, pages 1327–1334, Maui, HI, 2001.
- [TTHS95] J.K. Tu, J.J. Talghader, M.A. Hadley, and J.S. Smith. Fluidic self-assembly of ingaas vertical-cavity surface-emitting lasers onto silicon. *Electronics Letters*, 31(17):1448–1449, 1995.
- [TTW97] J. Tien, A. Terfort, and G.M. Whitesides. Microfabrication through electrostatic self-assembly. *Langmuir*, 13:5349–5355, 1997.
- [Ulm96] A. Ulman. Formation and structure of self-assembled monolayers. *Chem. Rev.*, 96:1533–1554, 1996.
- [VBCT04] J.M. Vorstenbosch, F. Bourgeois, S.K. Chollet, and M. Tichem. First results on vibration feeding of small parts in the presence of adhesive forces. *Assembly Automation*, 24(2):177–183, 2004.
- [WAE+00] W. Wijngaart, H. Andersson, P. Enoksson, K. Noren, and G. Stemme. The first self-priming and bi-directional valve-less diffuser micropump for both liquid and gas. In *Proceedings of IEEE International Conference of Micro Electromechanical Systems*, 2000.
- [Wan63] H. Wang. In *Proc. Symp. Math. Theory of Automata*, New York, 1963.
- [WF01] B.E. Williams and F.K. Forster. Micropump design of optimum pressure/flow characteristics. In *Proceedings of ASME International Mechanical Engineering Congress and Exposition*, 2001.
- [WG02] G.M. Whitesides and B. Grzybowski. Self-assembly at all scales. *Science*, 295:2418–2421, 2002.

- [WS00] A. Wüsch and M. Scussat. An innovative micro optical elements assembly robot characterized by high accuracy and flexibility. *Paper 41, ECTC2000, Las Vegas, USA*, 2000.
- [WXN<sup>+</sup>03] J. Wei, H. Xie, M. L. Nai, C. K. Wong, and L. C. Lee. Low temperature wafer anodic bonding. *J. of Micromech. and Microeng.*, 13:217–222, 2003.
- [XHF<sup>+</sup>03] X. Xiong, Y. Hanein, J. Fang, Y. Wang, W. Wang, D.T. Schwartz, and K.F. Böhringer. Controlled multi-batch self-assembly of micro devices. *IEEE Journal of Microelectromechanical Systems*, 12(2):117–127, 2003.
- [XWB04] X. Xiong, K. Wang, and K.F. Böhringer. From micro-patterns to nanostructures by controllable colloidal aggregation at air-water interface. In *Proceedings of IEEE Conference on Micro Electromechanical Systems*, Maastricht, Holland, 2004.
- [YBJ<sup>+</sup>97] R. Younkin, K.K. Berggren, K.S. Johnson, M. Prentiss, D.C. Ralph, and G.M. Whitesides. Nanostructure fabrication in silicon using cesium to pattern a self-assembled monolayer. *Appl. phys. Lett.*, 71(9):1261–1263, 1997.
- [YCSW04] K. Yang, I. Chen, B. Shew, and C. Wang. Investigation of the flow characteristics within a micronozzle / diffuser. *Journal of Micromechanics and Microengineering*, 14:26–31, 2004.
- [YGMM00] Z. Yang, H. Goto, M. Matsumoto, and R. Maeda. Ultrasonic micromixer for microfluidic systems. In *Proceedings of IEEE Micro Electromechanical Systems*, pages 80–85, 2000.
- [YGN01] G. Yang, J.A. Gaines, and B.J. Nelson. A flexible experimental workcell for efficient and reliable wafer-level 3d microassembly. In *Proceedings of ICRA2001*, pages 133–138, Seoul, South Korea, 2001.
- [YLF05] H. Yang, C. Lin, and W. Fang. Wafer level self-assembly of microstructures using the global magnetic lifting and localized induction welding. In *Proceedings of the 13th International Conference on Solid-State Sensors and Actuators*, Seoul, Korea, 2005.
- [YS94] H.J. Yeh and J.S. Smith. Fluidic self-assembly for the integration of gas light-emitting diodes on si substrates. *IEEE Photonics Technol. Lett.*, 6(6):706–708, 1994.



- [ZBJ04] W. Zheng, P. Buhlmann, and H.O. Jacobs. Sequential shape-and-solder-directed self-assembly of functional microsystems. In *Proc. Natl. Acad. Sci. U.S.A.* 101, 12814, 2004.
- [ZC03] Y. Zhao and T. Cui. Fabrication of high-aspect-ratio polymer-based electrostatic comb drives using the hot embossing technique. *J. Micromech. Microeng.*, 13:430–435, 2003.

## Appendix A

**PHOTOLITHOGRAPHY RECIPES**

*Note:* All the following recipes are for transparency masks used in our experiments. Transparency masks adsorb more UV light energy than glass masks.

**A.1 Positive Photoresist: AZ1512**

1. **Wafer cleaning:** soak in a NanoStrip solution for 5min, and then rinse in flowing DI water for 3min, and spin dry at 1200rpm for 5min.
2. **Singe** the wafer on a 90°C hotplate for 1min.
3. **Set a spin-coating recipe:** spread photoresist across the wafer at a speed of 500rpm for 5sec, and then thin the film at a speed of 3000rpm for 30sec.
4. **Spin-coat** adhesion primer P20.
5. **Spin-coat** AZ1512.
6. **Pre-bake** AZ1512 on a 90°C hotplate for 3min.
7. **Expose** AZ1521 through a mask to 10mW/cm<sup>2</sup> UV light for 8sec.
8. **Develop** in developer AZ351:H2O=1:4 or AZ300MIF for 25sec.
9. **Rinse** in flowing DI water for 1min.
10. **Spin dry** at 1200rpm for 5min.

11. **Hardbake** on a 90°C hotplate for 5min. (This step provides higher quality etching masks, and it should be skipped for lift-off patterning processes.)

Patterned AZ1512,  $\sim 1.2\mu\text{m}$  in thickness, can be used for (1) masks for BOE etching of silicon oxide; (2) masks for wet chemical etching of thin metal films such as Cr, Al, Cu, Au and TiW; (3) masks for reactive ion etching of silicon oxide and silicon nitride thin film; (4) sacrificial layers for thin film metal lift-off patterning processes.

### **A.2 Positive Photoresist: AZ4620**

1. **Wafer cleaning:** soak in a NanoStrip solution for 5min, and then rinse in flowing DI water for 3min, and spin dry at 1200rpm for 5min.
2. **Singe** the wafer on a 110°C hotplate for 1min.
3. **Set a spin-coating recipe:** spread photoresist across the wafer at a speed of 500rpm for 8sec, and then thin the film at a speed of 1500rpm for 40sec.
4. **Spin-coat** adhesion primer P20.
5. **Spin-coat** AZ4620.
6. **Pre-bake** AZ4620 on a 70°C hotplate for 5min, and then 100°C for 5min.
7. **Expose** AZ4620 through a mask to  $10\text{mW}/\text{cm}^2$  UV light for 30sec (expose for 15sec, then rest for 20sec to dissipate heat introduced by UV light, and expose for another 15sec).
8. **Develop** in developer AZ400K:H<sub>2</sub>O=1:2 for 2min.
9. **Rinse** in flowing DI water for 1min.

10. **Spin dry** at 1200rpm for 5min.
11. **Hardbake** on a 110°C hotplate for 5min.

Patterned AZ4620,  $\sim 10\mu\text{m}$  thicker than AZ1512, is usually used as masks for deep reactive ion etching of silicon.

### ***A.3 Negative Photoresist: single layer SU8-2025***

1. **Wafer cleaning:** soak in a NanoStrip solution for 5min, and then rinse in flowing DI water for 3min, and spin dry at 1200rpm for 5min.
2. **Singe** the wafer on a 200°C hotplate for 5min.
3. **Set a spin-coating recipe:** spread photoresist across the wafer at a speed of 500rpm for 8sec, and then thin the film at a speed of 2000rpm for 30sec.
4. **Spin-coat** SU8-2025.
5. **Pre-bake** SU8-2025 on a 65°C hotplate for 5min, and then 95°C for 20min.
6. **Cool down** for 2min.
7. **Expose** SU8-2025 through a mask to  $17\text{mW}/\text{cm}^2$  UV light for 30sec (expose for 15sec, then rest for 20sec to dissipate heat introduced by UV light, and expose for another 15sec).
8. **Post exposure bake** on a 65°C hotplate for 2min, and then 95°C for 6min.
9. **Relaxation** for 5min.
10. **Develop** in SU8 developer for 5min.

11. **Rinse** in IPA for 1min.
12. **Blow dry** with N<sub>2</sub>.
13. **Hardbake** on a 180°C hotplate for 30min.

Patterned SU8-2025 has a thickness of  $\sim 42\mu\text{m}$ .

#### ***A.4 Negative Photoresist: double layer SU8-2025***

1. **Wafer cleaning**: soak in a NanoStrip solution for 5min, and then rinse in flowing DI water for 3min, and spin dry at 1200rpm for 5min.
2. **Singe** the wafer on a 200°C hotplate for 5min.
3. **Set a spin-coating recipe**: spread photoresist across the wafer at a speed of 500rpm for 8sec, and then thin the film at a speed of 2000rpm for 30sec.
4. **Spin-coat** SU8-2025.
5. **Pre-bake** SU8-2025 on a 65°C hotplate for 5min, and then 95°C for 20min.
6. **Cool down** for 2min.
7. **Expose** SU8-2025 through a mask to 17mW/cm<sup>2</sup> UV light for 30sec (expose for 15sec, then rest for 20sec to dissipate heat introduced by UV light, and expose for another 15sec).
8. **Post exposure bake** on a 65°C hotplate for 2min, and then 95°C for 6min.
9. **Relaxation** for 5min.
10. **Spin-coat** 2<sup>nd</sup> layer SU8-2025 with a thinning speed of 1500rpm for 30sec.

11. **Pre-bake** on a 65°C hotplate for 5min, and then 95°C for 20min.
12. **Cool down** for 2min.
13. **Expose** through a mask to 17mW/cm<sup>2</sup> UV light for 60sec (with a 20sec break after each 15sec exposure to dissipate heat).
14. **Post exposure bake** on a 65°C hotplate for 5min, and then 95°C for 10min.
15. **Relaxation** for 5min.
16. **Develop** in SU8 developer for 10min.
17. **Rinse** in IPA for 2min.
18. **Blow dry** with N<sub>2</sub>.
19. **Hardbake** on a 180°C hotplate for 30min.

The lower and upper layers of SU8-2025 are respectively 42μm and 70μm in thickness.

## Appendix B

### DEEP REACTIVE ION ETCHING

Deep reactive ion etching processes were carried out on an Oxford Instruments DRIE Etcher (Model ICP 380) with a standard Bosch recipe:

The experimental parameters for the Bosch process were recorded as follows:

- Initial cool down the wafer to the table temperature 15°C for 5min.
- An **etching** step: time = 7sec, SF<sub>6</sub> flow rate = 100sccm, DC bias = 144V.
- A **deposition** step: time = 5sec, C<sub>4</sub>F<sub>8</sub> flow rate = 100sccm, DC bias = 74V.
- Chamber pressure = 20mTorr, RF forward power = 25W, ICP forward power = 1500W, helium pressure = 7Torr.

## VITA

Jiandong Fang was born in Anhui Province, People's Republic of China. In 1999 he obtained a Bachelor of Science degree from the department of modern physics at the University of Science and Technology of China (USTC). Then he attended the University of Washington, where he earned a Master degree in Physics in 2001, and a Doctor of Philosophy degree in Electrical Engineering in 2006.